ROLE OF METALLURGY IN THE THERMAL CONDUCTIVITY OF SUPERCONDUCTING NIOBIUM

By

Saravan Kumar Chandrasekaran

A DISSERTATION

Submitted to
Michigan State University
in partial fulfillment of the requirements
for the degree of

Mechanical Engineering – Doctor of Philosophy

2013

ABSTRACT

ROLE OF METALLURGY IN THE THERMAL CONDUCTIVITY OF SUPERCONDUCTING NIOBIUM

By

Saravan Kumar Chandrasekaran

Superconducting radio frequency (SRF) cavities for particle accelerators are fabricated using high purity niobium to allow for continuous high power operation. A hot-spot generated at a surface defect during accelerator operation can quench superconductivity and limit its performance. Increased heat conduction to the liquid helium bath dissipates hot spots, maintaining performance. Properly treated niobium may exhibit a local maximum (*i.e.*, phonon peak) in thermal conductivity at $T \approx 1.8$ K, the accelerator operating temperature. Conductivity with a phonon peak may be more than ten times that without the peak. Fabrication from ingot to cavity involves substantial processing, which in turn defines the metallurgical state of the niobium. Understanding the role of metallurgy and processing on conduction in the phonon regime can lead to improved accelerator performance.

This study reveals the role of metallurgy (*e.g.*, grain size and orientation, imperfection density, metal purity) and processing (*e.g.*, deformation, heat treatment) on the magnitude of the phonon peak. This study examines the most comprehensive set of conditions in a group of related uniaxial tensile specimens of mono- and bicrystal niobium with purity of $100 \lesssim \text{RRR} \lesssim 200$. Measurements of the thermal conductivity of the niobium were made with a coldest bath temperature of 1.6 K. A novel parameter estimation technique used data from a range of temperatures to determine parameters in a theoretically based model of the thermal conductivity of superconducting metals, without resorting to intermediate approximations.

The grain orientations and imperfection densities of the specimens were examined using electron backscatter diffraction and high energy X-ray diffraction, respectively. The role of deformation was examined by uniaxially straining several specimens to 2–38%, typical of SRF cavity manufacturing. The kinetics of recovering the phonon peak post-deformation was revealed by heat treating specimens from 140 ℃ for 48 h to 1200 ℃ for 2 h in a high-vacuum furnace. Two specimens were saturated with hydrogen to examine its effect on thermal conductivity.

The as-received specimens displayed no phonon peak due to thermal strain-induced dislocations from ingot production. The recovery of a phonon peak depended sigmoidally on the heat treatment temperature, with a plateau after 1000 ℃. The dislocation density of the specimens decreased with increasing heat treatment temperature, but the vacancy concentration increased dramatically. Phonon conductivity appears to be dependent on the vacancy concentration. In addition, smaller RRR yielded a smaller phonon peak.

Results revealed that the density of dislocations introduced during deformation depends on both grain orientation and strain level. The recovery of the phonon peak by post-deformation heat treatment at 1000 ℃ for 2 h was complete for specimens with $\leq$ 74% reduction in the phonon peak due to strain-induced dislocations. Although hydrogen infused during typical cavity processing steps left the phonon peak unchanged, specimens saturated with hydrogen displayed a 25% reduction. The concentration of hydrogen was deduced to be affected by vacancy concentration of the specimens.

These results should assist those designing and manufacturing SRF cavities by guiding them to the processes that may provide the greatest possible thermal conductivity for niobium cavities operating at $T = 1.8$ K.

In memory of my beloved grandfather, Mr. T.A. Muthuswamy.

ACKNOWLEDGMENTS

The majority of this work was supported by the U.S. Department of Energy, Office of High Energy Physics, through Grant No. DE-S0004222. This research was partially supported by Fermi National Accelerator Laboratory and National Superconducting Cyclotron Laboratory (NSCL). Use of the Advanced Photon Source was supported by the U.S. Department of Energy, Office of Science, Office of Basic Energy Sciences, under Contract No. DE-AC02-06CH11357. The large grain niobium discs used in this research were generously provided by Dr. Ganapati Myneni from the Thomas Jefferson National Accelerator Facility, in exchange for RRR estimates of the discs in their as-received condition.

I wish to express my deepest gratitude to my dissertation adviser, Dr. Neil Wright, for his excellent guidance, patience, and encouragement. His ability and willingness to tackle heat transfer problems, both theoretically and experimentally, using his broad knowledge has guided me through this work. His ability to think from the perspective of the audience is astounding, and I have benefitted from this on several occasions. I am thankful to him for demonstrating how to be diplomatic and to look at the larger picture to take balanced decisions.

I am grateful to Dr. Thomas Bieler for introducing me to the concepts of metallurgy, and for patiently supporting me while I delved into the gigantic set of X-ray data. I have greatly benefitted from his open-door policy during this work. His commitment to science and knowledge is an inspiration, especially for young scientists.

I am thankful to Chris Compton for his technical and logistical support during the entire period of this research. I truly appreciate his efforts to keep my hopes up during the long delays in scheduling experiments, especially during the last two years of this work.

I would also like to thank Dr. James Beck for his thoughtful comments during this work, and for guiding me through the intricacies of parameter estimation. His desire to share knowledge and his willingness to assist in identifying solutions to problems of all magnitudes is inspiring.

I wish to thank Drs. Farhang Pourboghrat and Craig Somerton for their comments and suggestions on my work, and for being members on my doctoral guidance committee.

I am grateful to Drs. Terry Grimm and Walter Hartung for introducing me to the world of accelerator physics. Walter's patience while clearing my doubts in this field is truly appreciated.

I could not have completed the cryogenic experiments without the expert assistance of Steve Bricker, Dave Norton, and Allyn McCartney. Steve's and Dave's patience during the pump down of liquid helium, especially while maintaining steady pressures for constant temperature calibration data points, is truly appreciated. I am thankful to Allyn for often going out of the way to ensure that the cryogenic group was able to support my helium requirements. I also appreciate Dave's advice and assistance with data acquisition. I am also grateful to John Bierwagen for his assistance on several occasions, and for always being willing to help.

I am grateful to Lindsay Dubbs, Kyle Elliott, and Ian Malloch for performing chemical treatments on my specimens, often at very short notice, while I was safely outside the acid room. I wish to thank undergraduate students, Aaron Winter, Andrew Rauch, and Joseph Asciutto, for their assistance in preparing sensors for the experiments.

I am indebted to my fellow graduate student, Di Kang, for performing the majority of the OIM reported in this work, and for voluntarily training me to use the OIM microscope and the Laue X-ray diffraction apparatus. I am grateful to Bite Zhou for demonstrating and teaching me to acquire high energy X-ray diffraction data at the APS at ANL. I wish to thank fellow graduate students from Mechanical Engineering and NSCL, especially Jeremiah Holzbauer, Payam Darbandi, Aboozar Mapar, and Derek Baars, for several useful conversations.

I wish to thank the administrative staff of Mechanical Engineering and NSCL, especially Aida Montalvo, Craig Gunn, and Amanda Alter, for their excellent support and assistance.

The love, support, and encouragement from my parents, L.M. Chandrasekaran and Devi Chandrasekaran, and sister, Gayathri Chandrasekaran, have been the foundation of my standing today. The advice and support from my in-laws, Drs. K. Balu and P.S. Meenakshi, on the personal and professional aspects of graduate life have come in handy several times. I cannot express enough my appreciation of my best friend and wife, Deebika Balu. Despite the physical distance between us, her willingness and desire to stand by me and encourage me during easy and tough times were instrumental in me making it to the other side. Thank you!

TABLE OF CONTENTS

LIST OF TABLES

LIST OF FIGURES

Chapter 1

Introduction

Studying the effect of the metallurgical state on the thermal conductivity of superconducting niobium offers the opportunity to examine the influence of vacancies, dislocations, and grain boundaries on the phonon contribution to conductivity. The motivation for this study is the design and manufacture of improved superconducting radio frequency particle accelerator cavities. First, an overview of superconductivity, as applied to accelerator cavities is given. Then, heat transfer in accelerator cavities is considered.

1.1 Background

Particle accelerators are used in high-energy physics research, biomedical treatments, and homeland security applications to accelerate beams of charged atomic or sub-atomic particles. High energy physics applications often require particle beams to be accelerated to nearly the speed of light, c. These accelerators are comprised of several components, including accelerating cavities, magnets, and solenoids. Accelerator cavities impart energy to the particles being accelerated, while the magnets and solenoids steer the particle beam in the desired direction and keep the beam focused.

To impart the energy, current is applied to the interior of the accelerating cavity. Radio frequency (RF) alternating current provides energy to each particle in the beam from each cavity. Synchronizing the current provides repeated acceleration at each cavity. RF cavities have traditionally been manufactured from metals, such as copper and niobium. Normal conducting, room temperature cavities have been made of copper due to its ease in formability and due to its high thermal conductivity (400 $\mathrm{Wm^{-1}K^{-1}}$). However, room temperature cavities have high electrical (RF) losses due to the electrical resistivity of normal conducting copper, and their accelerating gradients are limited by the capacities of RF power supplies. They are also limited to pulsed operation as the electrical resistance causes large temperature excursions.

High-energy physics research and other applications require continuous operation making superconducting metals the materials of choice for RF cavities. Niobium is widely used to fabricate superconducting radio frequency (SRF) cavities, as it has the highest superconducting critical temperature (T_c) for any metal ($T_\mathrm{c} = 9.25$ K). Superconducting metals have zero DC electrical resistance and a very small RF electrical resistance. Though non-zero, the RF electrical resistance in superconducting Nb is much smaller than that in normal conducting copper. Despite the need for constant cryogenic refrigeration of the SRF cavities, the total power requirements for the operation of SRF cavities is about 200 times smaller than that required for normal conducting copper cavities [1]. The niobium cavities are submersed in a liquid helium bath and operate at $1.8\ \mathrm{K} \lesssim T \lesssim 4.5\ \mathrm{K}$.

A schema of an elliptical single-cell cavity is shown in Figure 1.1. The particle beam travels through the beam pipe and energy is imparted across the iris by the RF electric field. The frequency of the electric field is synchronized with the velocity of the particles

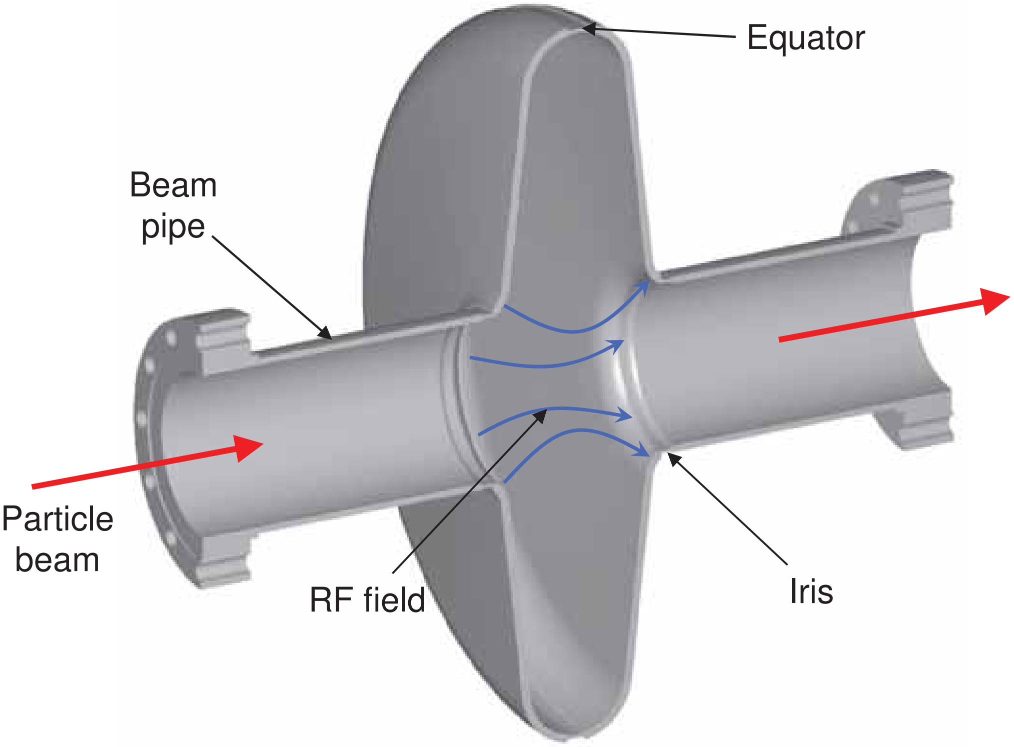

Figure 1.1: A schema of a single-cell elliptical SRF cavity. Charged particles are accelerated in a vacuum by an RF field confined to the inner volume. The cavity is submerged in liquid helium. For interpretation of the references to color in this and all other figures, the reader is referred to the electronic version of this dissertation.

being accelerated, so as to attract the particle toward the iris during the first half of the RF cycle and repel the particle away from the iris during the second half cycle of the alternating electric field. For example, in an electron accelerator, the positive half cycle of the RF electric field would attract the electron toward the iris, and the negative half cycle would repel the electron away from the iris. The particle beam and the RF electric field are confined to the inner volume of the cavity, which is maintained under vacuum.

The RF electric field applied on the interior of the cavity induces a magnetic field in the azimuthal direction. The magnetic field penetrates the inner surface of the cavity up to the London penetration depth, which is about 40 nm for Nb. The interaction of the RF magnetic field with Nb results in Joule heating. The presence of local surface defects on the inner surface of these cavities creates hot spots that reduce cavity performance, and ultimately lead to the destruction of superconductivity, also known as quench. Heat conduction from the heat source to the liquid helium bath surrounding the cavity prevents or delays the onset of a quench. Impurities and crystal imperfection added during metal forming may reduce the thermal conductivity and thus, the cavity performance.

1.2 RF cavity basic definitions

In RF cavities, the average accelerating electric field (E_{acc}) experienced by the particle being accelerated is used as a measure of performance for the cavity. The average accelerating electric field is related to the applied accelerating voltage (V_{acc}) as

$$E_{\mathrm{acc}} = \frac{V_{\mathrm{acc}}}{d}, \tag{1.1}$$

where d is the effective accelerating distance within the cavity. In the case of elliptical cavities such as that illustrated in Figure 1.1, d is the iris-to-iris distance.

The efficiency of a cavity is measured using the quality factor Q, which is defined as the ratio of the energy stored in the cavity to the energy dissipated in a cycle. It may be written as

$$Q = \frac{\omega U}{P_{\text{diss}}}, \tag{1.2}$$

where ω is the RF angular frequency, U is the total electromagnetic energy stored in the cavity per RF cycle, and P_{diss} is the energy dissipated by the cavity per RF cycle. The stored energy U in equation (1.4) is defined as

$$U = \frac{1}{2}\mu_0 \int_V |H|^2 \mathrm{d}V, \tag{1.3}$$

where μ_0 is the magnetic permeability of Nb, H is the amplitude of the magnetic field, and V is the volume of the cavity. The total dissipated power per RF cycle is written as

$$P_{\text{diss}} = \frac{1}{2}R_s \int_S |H|^2 \mathrm{d}S, \tag{1.4}$$

where R_s is the surface resistance of the cavity, and S is the surface of the cavity. Hence, Q can be written as

$$Q = \frac{\frac{1}{2}\omega\mu_0 \int_V |H|^2 \mathrm{d}V}{\frac{1}{2}\int_S |H|^2 \mathrm{d}S} \cdot \frac{1}{R_s} = \frac{G}{R_s}, \tag{1.5}$$

where G is termed the geometry factor, and is influenced by the shape of the cavity and the electromagnetic field distribution within the cavity.

1.2.1 Superconducting RF cavities

SRF cavities are desirable because these are high Q devices as compared with room temperature devices, and a necessity for high-voltage continuous (CW) applications.

The two-fluid model explains the zero DC electrical resistance of superconductors, for $T < T_\mathrm{c}$, as a result of the formation of Cooper pairs (fluid 1) in a bath of normal conducting electrons (fluid 2). The Cooper pairs are bound by energy $2\Delta(0)$, where $\Delta(0)$ is the superconductor energy gap at $T = 0$ K. The electrons in Cooper pairs, despite their similar charge, interact with phonons and remain paired until the energy of the phonon is greater than $2\Delta(0)$. The number of electrons condensed into Cooper pairs is a function of T. All electrons are Cooper pairs at $T = 0$ K, and for $T > 0$ K the Boltzmann function $\exp(-\Delta(T)/k_\mathrm{B}T)$ defines the number of electrons that are condensed into Cooper pairs.

The Cooper pairs in DC superconductors flow without any resistance through the lattice, and hence the electrical resistance is zero. In RF applications, however, the magnetic field penetrates the surface of the superconductor. The depth of this penetration is known as the London penetration depth, and is defined as

$$\lambda_\mathrm{L} = \sqrt{\frac{m}{n_s e^2 \mu_0}}, \tag{1.6}$$

where m is the mass of an electron, n_s the number of superconducting electrons, e the charge of an electron, and μ_0 the magnetic permeability. The temperature dependent expression for λ_L, as obtained from the two-fluid model, is

$$\lambda_\mathrm{L}(T) = \lambda_\mathrm{L}(0)\frac{1}{\sqrt{1 - \left(\frac{T}{T_\mathrm{c}}\right)^4}}. \tag{1.7}$$

The periodic reversal of the magnetic field in the penetration depth, induces an electrical current that interacts with the normal electrons, and leads to electrical resistance and dissipation. For $T < T_\mathrm{c}/2$, this electrical resistance was quantified by the BCS theory to be

$$R_\mathrm{BCS}(T) = A\frac{\omega^2}{T}\exp\left(-\frac{\Delta(0)}{k_\mathrm{B}T}\right), \tag{1.8}$$

where A is a constant dependent on several material properties (*e.g.*, the London penetration depth, mean free path length of electrons, Fermi velocity, coherence length), ω the frequency in GHz, $2\Delta(T)$ the superconductor energy gap, and k_B the Boltzmann constant. Due to the dependance of A on material properties, especially the mean free path length of the electrons, it is influenced by the impurity content of Nb. A measure of the impurity content is the residual resistivity ratio (RRR), defined as

$$\mathrm{RRR} = \frac{\rho_{295}}{\rho_{4.2}}, \tag{1.9}$$

where ρ_{295} is the room temperature electrical resistivity, and $\rho_{4.2}$ the normal conducting electrical resistivity at 4.2 K. Hence, A cannot be easily estimated using standard formulae, and computer programs written independently by Turneaure [2] and Halbritter [3] can be used to estimate A.

Below a certain temperature, in addition to R_BCS, a residual resistance $R_\circ$ has been observed experimentally [1]. This resistance is a constant and is independent of temperature. With careful preparation of the RF surface of the cavity, $R_\circ$ as low as 1 nΩ had been observed.

These resistances act in series, and hence the total surface resistance R_s may be written as

$$R_s = R_{\text{BCS}}(T) + R_\circ = A\frac{\omega^2}{T}\exp\left(-\frac{\Delta(0)}{k_{\text{B}}T}\right) + R_\circ. \tag{1.10}$$

1.3 Niobium SRF cavity limits

1.3.1 Magnetic field

When a DC magnetic field is applied on a superconductor, the superconductor expels the magnetic field completely. This phenomenon is known as the Meissner effect. When the applied DC magnetic field is increased above a critical value H_c, the superconductor becomes normal conducting and allows magnetic field lines to penetrate the conductor. The critical magnetic field H_c depends on the temperature, and is approximated as

$$H_\text{c}(T) \approx H_\text{c}(0)\left[1-\left(\frac{T}{T_\text{c}}\right)^2\right], \tag{1.11}$$

where $H_\text{c}(0)$ is the critical magnetic field at $T = 0$ K. Niobium being a Type-II superconductor, has two critical magnetic fields. When the applied DC magnetic field H is greater than the first critical magnetic field $H_{\text{c}1}$, normal conducting magnetic flux vortices penetrate the superconductor. Despite these vortices being normally conducting, the material around these vortices is still superconducting and can support the flow of Cooper pairs. Above a second critical magnetic field $H_{\text{c}2}$, however, the normal conducting magnetic flux vortices completely occupy the superconductor, transforming it into a normal conductor. The phase with partial occupancy of magnetic flux vortices, *i.e.*, for $H_{\text{c}1} \leq H \leq H_{\text{c}2}$, is referred to as the “mixed state”. For Nb at $T = 0$ K, $H_\text{c} = 2000$ Oe, $H_{\text{c}1} = 1700$ Oe, and

$H_{c2} = 2400$ Oe [1].

When an RF magnetic field is applied on Type-II superconductors like Nb, the critical magnetic field is further enhanced to a value known as the "superheated" critical magnetic field H_{sh}. Due to the RF period (*e.g.*, $t = 10^{-9}$ s for 1 GHz cavity) being several orders of magnitude smaller than the time $t \approx 10^{-6}$ s estimated by Flippen [4] for the penetration of the magnetic flux vortices, the critical magnetic field required for phase transformation to normal conducting is $H_{sh} > H_c$.

1.3.2 Thermal breakdown

The thermal limit for SRF cavities is when the temperature T exceeds T_c. Often times, the increased temperatures decrease H_c, thereby decreasing performance of the cavity. There are several factors that can lead to $T \geq T_c$, including defects on the RF surface. There are four dominant causes for thermal breakdown, which can act either individually or in unison. The four are: defects on the RF surface of the cavity, global thermal instability (GTI), multipacting, and field emission.

1.3.2.1 RF surface defects

The interaction of the RF magnetic field with the defect on the RF surface leads to Joule heating and power dissipation. The timely dissipation of this excess heat from the RF surface, through the Nb bulk, to the liquid helium surrounding the exterior of the cavity ensures that T at the defect remains cooler than T_c. Depending on the size, and hence the resistance, of the defect and the RF field being applied, the power loss could increase substantially to the state where $T \geq T_c$ at the edge of the defect. This leads to the surface surrounding the defect to become normal conducting, and thereby increasing the RF power dissipation. For effective containment of T, the thermal conductivity k of Nb and either the heat transfer coefficient h (for $T > 2.17$ K) or the Kapitza conductance h_{K} (for $T < 2.17$ K) across the Nb-liquid helium interface play a vital role.

The defect-limited maximum of H for a hemispherical defect on the RF surface was estimated by Padamsee [1] to be

$$H_{\mathrm{d,\ max}} = \sqrt{\frac{4k}{a_{\mathrm{d}} R_{\mathrm{d}}} (T_{\mathrm{c}} - T_b)}, \tag{1.12}$$

where a_{d} is the radius of the defect, R_{d} the surface resistance due to the defect, and T_b the temperature of the liquid helium bath. Note that $H_{\mathrm{d,\ max}} \propto \sqrt{k}$, hence greater k in the Nb bulk would increase the maximum defect-limited magnetic field.

1.3.2.2 Global thermal instability

The surface resistance of a SRF cavity is a function of the squared of the frequency of the cavity and the temperature T at the cavity surface. In defect-free RF cavities, at high frequency operations, the increase in R_{s} due to the frequency causes an increase in P_{diss} leading to an increase in T_s. In such situations, if the heat generated cannot be dissipated to the liquid helium, a thermal runaway can occur until superconductivity is lost leading to rapid dissipation of the stored energy within the cavity. This phenomenon is known as the global thermal instability (GTI) [5], and occurs simultaneously in the high magnetic field regions of the cavity, *i.e.*, near the equator of the cavity.

1.3.2.3 Multipacting

Multipacting is a resonant electron phenomenon where an electron strikes the surface of the cavity, causing secondary electrons to be released from the surface of the cavity. These secondary electrons are influenced by the RF electric field, and can accelerate and strike the surface of the cavity near its point of origination, releasing more such secondary electrons and dumping energy into the surface of the cavity causing a local temperature rise. As multipacting is a resonant phenomenon, it occurs at a specific frequency for a microwave cavity.

1.3.2.4 Field emission

Field emission is a non-resonant phenomenon, where electrons from the surface of the cavity are extracted by the RF electric field. These electrons, influenced by the cavity's electric field, are accelerated and dumped on the surface of the cavity at a location other than its point of extraction. At the location of dump, the energy gained by the electrons from the electric field are lost as heat.

1.4 Heat transfer in SRF cavities

For increased performance of SRF cavities, the RF surface temperature T_s needs to be as cool as possible. The heat generated on the RF surface by the various sources listed in Section 1.3.2 can cause the temperature of Nb to rise and increase the surface resistance R_s. Due to the interrelation between T_s and R_s, a thermal runaway can occur, leading to quench. To prevent or delay the onset of such an event, the heat being generated at the RF surface of the cavity needs to be dissipated away from the RF surface, through the Nb

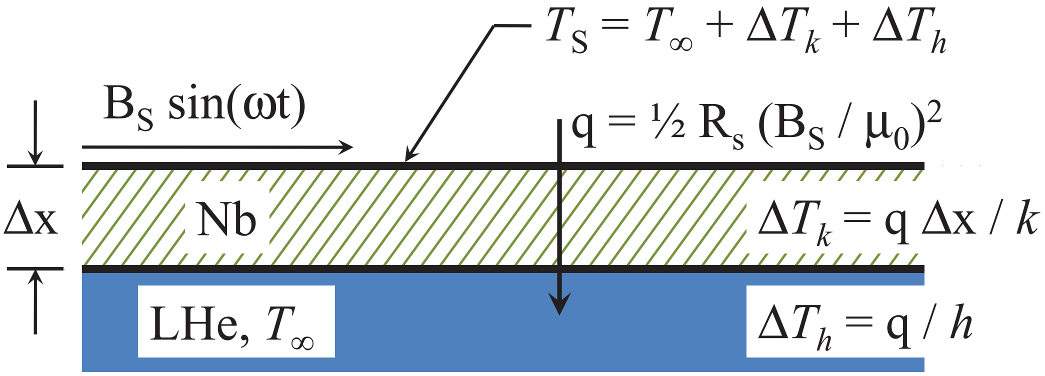

Figure 1.2: One dimensional heat transfer from the inner to the outer wall of a Nb SRF cavity. Subscripts s, k, h and ∞ refer to the inner surface, due to conduction, due to convection, and of liquid helium (LHe), respectively.

bulk and into the liquid helium surrounding the cavity. Hence, the thermal conductivity k of bulk Nb and the Kapitza conductance h_{K} across Nb-helium interface play a vital role in the performance and thermal stability of SRF cavities. As is conventional in heat transfer, the power dissipated at the RF surface P_{diss} will be denoted as the heat flux q. Local surface defects increase R_s, and in turn increase q. In the case of defects on the RF surface, k of Nb needs to be sufficient to diffuse q away from the defect before T_s gets hotter than T_{c}.

For heat transfer purposes, the heat dissipation through the Nb wall can be considered as a one dimensional heat transfer problem [6]. A schematic of the one dimensional heat transfer problem with heat flow from the RF surface to the liquid helium bath surrounding the cavity is illustrated in Figure 1.2.

1.5 SRF cavity fabrication and processing

There are several types of SRF cavity designs, each specific to a particular operating frequency range. For near the speed of light applications, high frequency cavities are used.

These cavities typically are elliptical, as illustrated in Figure 1.1.

Conventionally, elliptical cavities are fabricated either using polycrystal niobium from rolled sheets or large grain niobium discs cut from ingots. Regardless of the initial material, the fabrication of elliptical SRF cavities includes deep drawing of niobium discs into half cells, electron beam welding of two half cells to form a cavity, and mechanical cavity shape tuning to attain desired frequency. These steps are often interspersed with one or more buffer chemical polishing (BCP) or electro-polishing (EP) steps to remove damage layer and contaminants from the RF surface of the cavity. After fabrication into a cavity, it undergoes several processes prior to actual application. In addition to BCP or EP, the processing of these cavities include one or more heat treatments in high to ultra-high vacuum at temperatures hotter than 600 ℃ to primarily degas hydrogen. Additionally, an *in situ* heating at around 120 ℃ – 140 ℃ for 24–48 h is performed, which increases high field cavity performance in cavities fabricated from polycrystal Nb [7, 8] and large grain or single crystal Nb [9]. The processing of cavities is empirically optimized to increase cavity performance, by obtaining smooth RF surfaces for reduced RF losses, and increase bulk properties for improved heat transfer from the inside RF surface of the cavity to the liquid helium bath in contact with the outer surface of the cavity [1]. Flow charts summarizing the significant steps in fabrication and processing of elliptical cavities are illustrated in Figures 1.3 and 1.4, respectively. Cavities fabricated using alternate techniques, such as hydroforming [10, 11] or spinning [12, 13], have fabrication paths that are dissimilar to that shown in Figure 1.3, but have similar processing steps as listed in Figure 1.4.

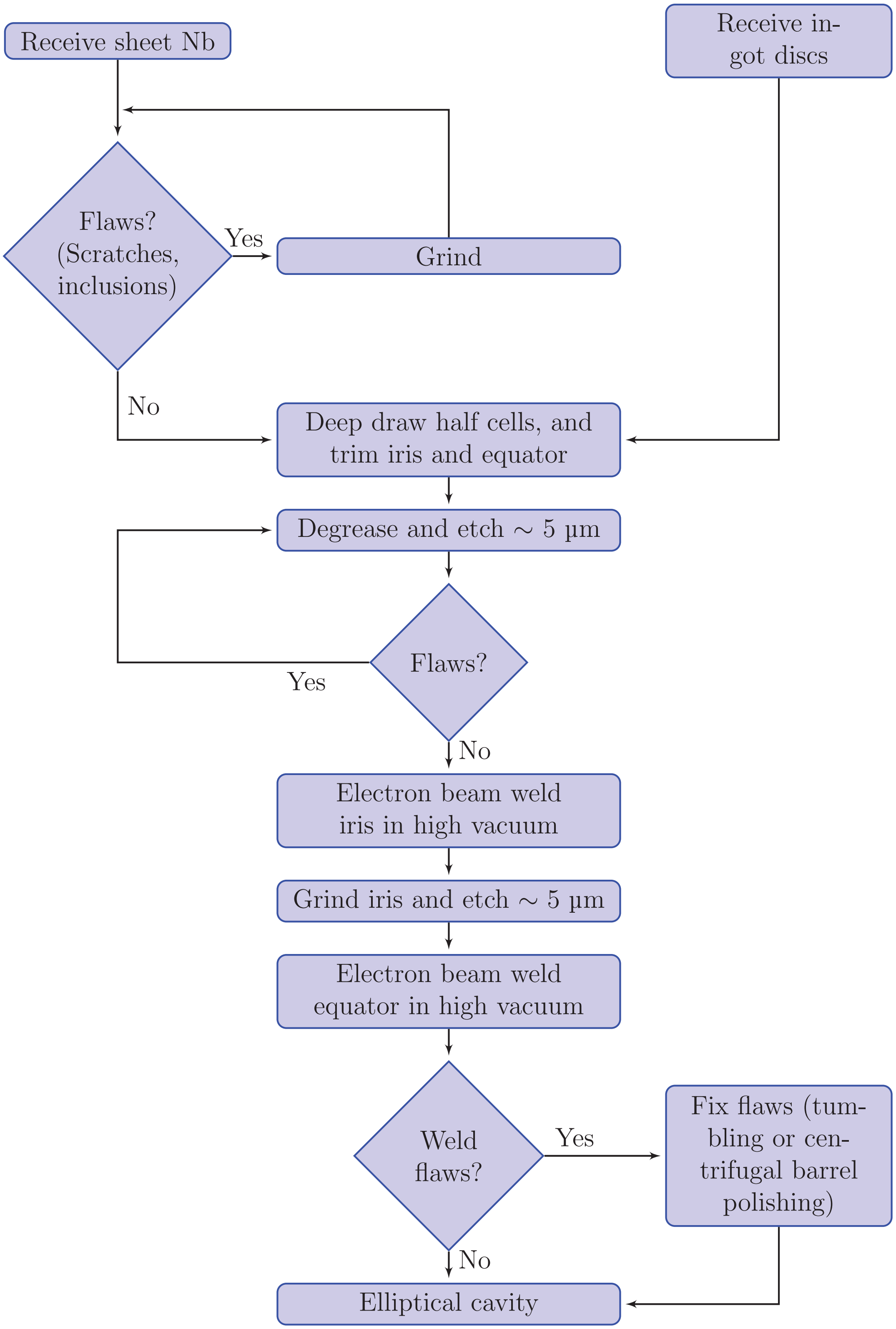

Figure 1.3: The steps involved in the fabrication of an elliptical cavity from either sheet niobium or ingot niobium discs [1, 14, 15]. There is significant processing done after obtaining the elliptical shape, and is illustrated in Figure 1.4.

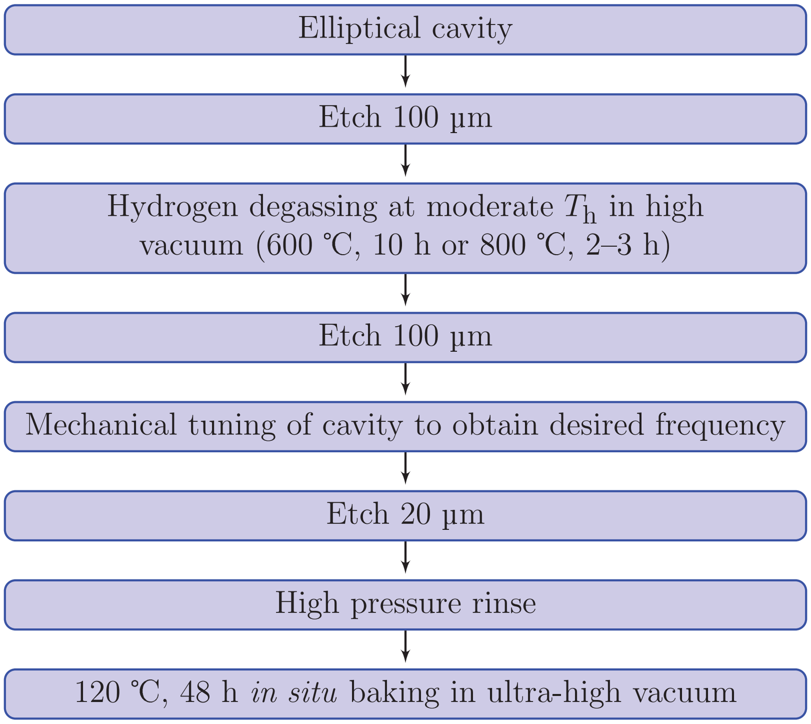

Figure 1.4: Processing of cavities after obtaining elliptical shape [1, 14, 15]. The steps involved in obtaining the initial elliptical cavity by deep drawing are presented in Figure 1.3. Fabrication steps for seamless cavities obtained by hydroforming or spinning are different from those presented in Figure 1.3, but the processing steps are similar.

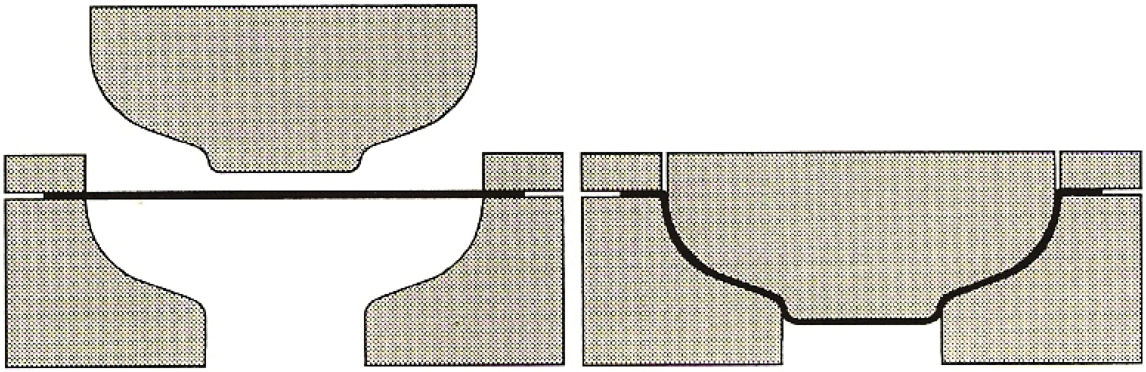

Figure 1.5: Deep drawing a niobium disk into a half cell. (Copyright Wiley-VCH Verlag GmbH & Co. KGaA. Reproduced with permission from [1].)

1.5.1 Deep drawing and electron beam welding

After inspection of the niobium sheets using eddy current scanning or squid scanning, discs are cut from the sheets to be deep drawn. Two-part aluminium dies are used to form the Nb into the desired shape, as illustrated in Figure 1.5. To prevent Nb from sticking to the die, conventional motor oil is used as lubrication. Subsequently, the formed Nb is trimmed at the equator and iris regions to final half cell shape. The half cells are then ultrasonic cleaned with a detergent to remove contaminants left over from the deep drawing and trimming processes, and about 20 µm of material is etched from the cavity prior to welding.

The half cells are electron beam welded in high vacuum. The welds at the iris are performed first, followed by equator welds to form full cavities. The iris welds are inside welds, while the equator welds are done from the outside of the cavity. The welds and the inner surface of the cavity are then inspected for any imperfections. Grinding, tumbling or centrifugal barrel polishing are often used to get rid of the imperfections [15].

1.5.2 Etching and cleaning

The cavity is etched either using BCP or EP to remove the surface damage layer (∼ 100 µm) formed during deep drawing. The BCP is a mixture of 49% diluted hydrofluoric acid, 69% diluted nitric acid, and 85% diluted phosphoric acid, in ratios of 1:1:1, 1:1:2 or 1:1:4. To reduce the absorption of hydrogen by Nb during BCP, the acid mixture is maintained at 10 ℃ [16]. Alternately, instead of BCP, EP is used to etch the cavity. During EP, the cavity is electrically charged and immersed in a 1:9 mixture of hydrofluoric and sulfuric acids. The electrical charging preferentially etches surface peaks, leading to a smooth surface.

The final step in the processing of cavities prior to assembling it into the accelerator (or test apparatus), is a high pressure rinse using ultra pure water [15]. Water jets are sprayed onto the inner surfaces of the cavity at a pressure of 100 bar, to remove any contaminants present on the surface.

1.5.3 Cavity heat treatments

1.5.3.1 Moderate to high temperature heat treatments

The performance of SRF cavities was often reduced when a cavity was slow cooled to 4.2 K. It was linked to the precipitation of hydrogen into hydrides, at temperatures of 77–150 K [16, 17]. An empirical solution was to heat treat the cavity, prior to cool down, at $T_\mathrm{h} \geq 600$ ℃ in high vacuum [17] to sufficiently degas hydrogen from the material and prevent hydride formation. Additionally, the rate of cool down from 298 K to 4.2 K was increased, to reduce the time available for the precipitation of hydrides [16]. Figure 1.6 illustrates the improvement of cavity performance after an 800 ℃ and a 1400 ℃ heat treatment [18].

Hotter temperature heat treatments ($T_\mathrm{h} \geq 1200$ ℃) in high vacuum in the presence of

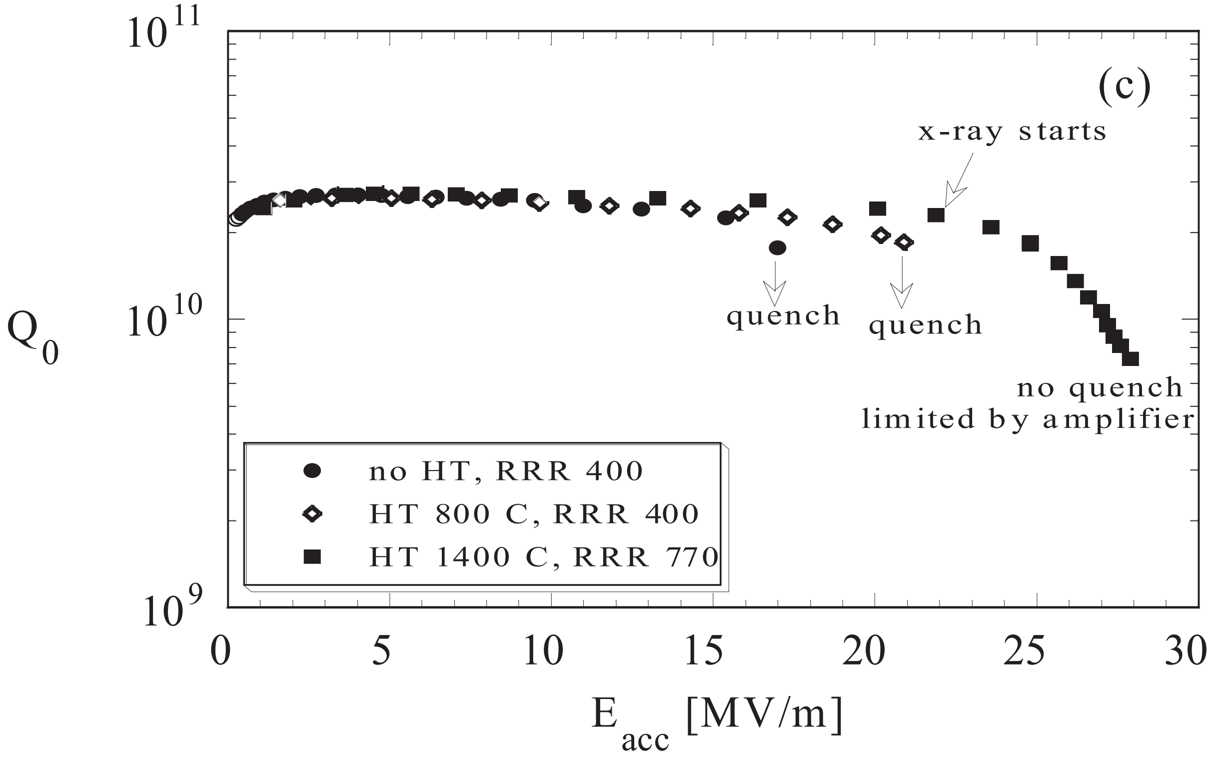

Figure 1.6: Performance of a niobium cavity before and after an 800 ℃ and a 1400 ℃ heat treatment [18]. After heat treatment, the cavity produces higher accelerating gradients before quenching, although Q_0 is unchanged. Quenching is due to loss of superconductivity initiated at a local hot spot. (Reproduced from [18] under the Creative Commons Attribution License 3.0. Copyright 2000 by The American Physical Society.)

a getter material, like titanium or yttrium, were also used to enhance the performance of cavities [19, 20]. In addition to degassing hydrogen, these heat treatments anneal the Nb to reduce the strain and dislocations in the material. In the absence of a getter material, the thermal conductivity and RRR of Nb reduces due to diffusion of surface impurities into the bulk [21]. At $T_\mathrm{h} \geq 1200$ ℃, with a getter, the RRR increases by a factor of 2–3.

1.5.3.2 Low temperature heat treatments

An *in situ*, relatively low temperature heat treatment at $100 \geq T_\mathrm{h} \geq 170$ ℃ for $t > 24$ h was found to increase cavity performance at high accelerating fields [7, 8, 22]. A comparison

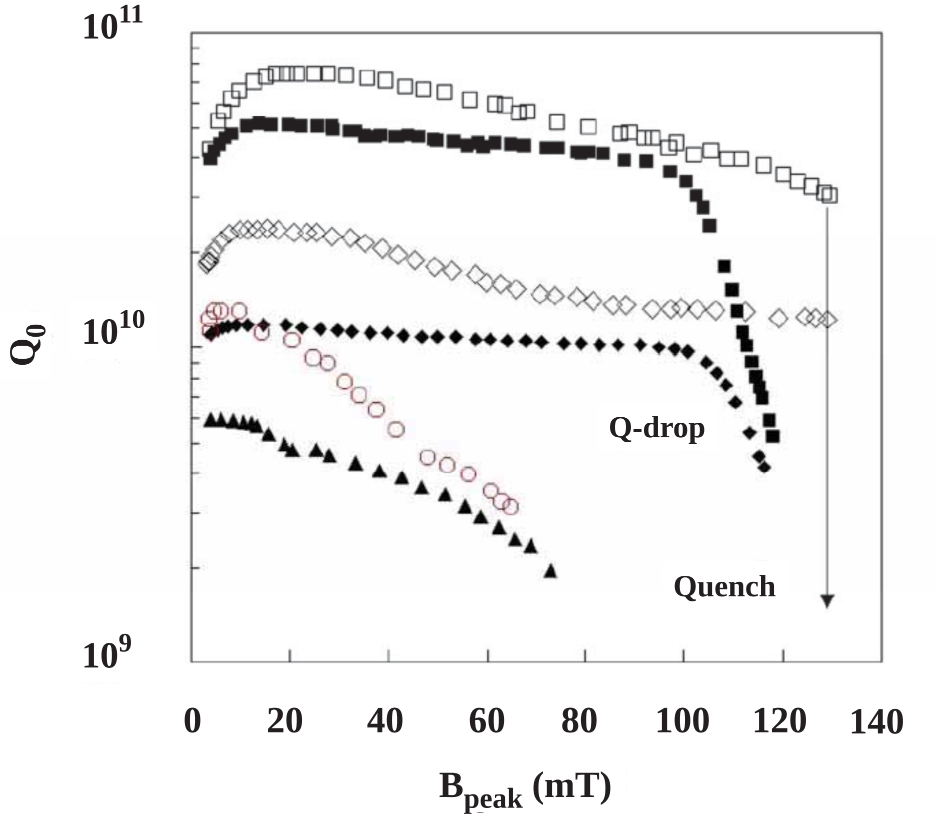

Figure 1.7: Quality factor as a function of magnetic flux before (solid symbols) and after 120 ℃ 48 h baking (open symbols) at three different temperatures: 1.37 K (squares), 2 K (diamonds), and 2.2 K (circles, triangles). (Reprinted with permission from [23]. Copyright 2004, American Institute of Physics.)

of the effect of the in situ low temperature bake for different operating temperatures is illustrated in Figure 1.7 [23].

1.6 Cavity processing and thermal conductivity

The thermal conductivity k of Nb and the Kapitza conductance h_K across the Nb-liquid helium interface are vital properties influencing the quench field of a cavity. The induced RF magnetic field generates heat on the interior surface of the cavity, and sometimes is locally enhanced due to surface imperfections and defects. To keep the Nb superconducting, this heat must be dissipated to the liquid helium that is in contact with the exterior surface of the cavity.

The plastic deformation involved during deep drawing Nb into half cells generates dislocations in the material. Excessive dislocations are sources for scattering phonons. Phonons are thermally activated lattice vibrations, and are a component of thermal conductivity. The diminishing effect of deformation induced dislocations on the thermal conductivity of Nb was first observed by Rowell [24], and was confirmed by several researchers [25–28]. The effect of room temperature deformation on the thermal conductivity of single crystal Nb, for 4% and 8% strain, is redrawn from [26] in Figure 1.8. The local peak in the thermal conductivity at around 1.8 K is due to the contribution of phonons, and is referred to as the phonon peak. Figure 1.8 shows that the phonon conductivity can vary by more than an order of magnitude at 1.8 K, due to deformation by virtue of dislocations.

In deep drawn Nb cavities as well as hydroformed and spun cavities, prior to any heat treatment, it can be assumed that there is no phonon peak. Although the effect of deformation on the phonon peak can be reversed [25] by annealing Nb close to its melting temperature (2468 ℃), there is an undesired loss in the mechanical properties even for heat treatments at $1200 \leq T_{\mathrm{h}} \leq 1400$ ℃ [29]. Additionally, the cost of heat treatments increases exponentially with temperature, due to the exponential increase in the power requirements for the furnaces [30].

The commonly used high temperature ($T_{\mathrm{h}} \geq 1200$ ℃) heat treatments, with getter material, during cavity processing increases the thermal conductivity of undeformed polycrystal Nb. With a getter, the RRR increases and leads to greater thermal conductivity in the electron dominated regime ($T \geq 3$ K), as illustrated in Figure 1.9 [20]. The corresponding

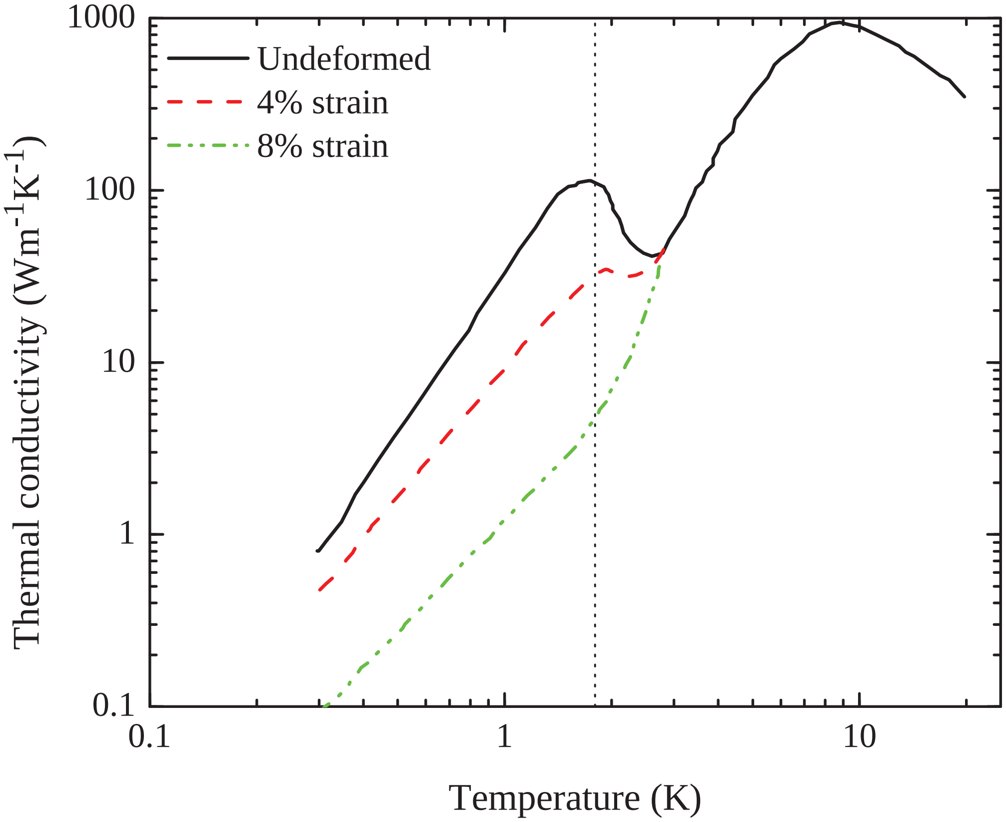

Figure 1.8: Effect of room temperature deformation on the thermal conductivity of superconducting single crystal niobium. The undeformed specimen has the highest conductivity at 1.8 K, followed by the 4% and 8% strained specimens, respectively. The vertical dashed line is drawn at $T = 1.8$ K. (Copyright Taylor & Francis. Redrawn with permission from [26])

increase in the phonon dominated regime ($T \leq 3$ K) in the polycrystal Nb specimens is due to the increase in grain size during annealing. In polycrystal Nb, it has been observed that the phonon peak is limited mainly by grain size (grain boundary scattering), while it is mainly limited by specimen boundary scattering in monocrystal and large grain Nb.

In addition to the temperature of measurement, the factors influencing the thermal conductivity of polycrystal and large grain superconducting Nb can thus be grouped as metallurgical and processing factors, as illustrated in Figure 1.10. The metallurgical factors are grain size, crystal orientation, and purity (RRR), while deformation and heat treatments are the processing factors that affect the thermal conductivity.

Although researchers have looked at the effect of one or more factors on the thermal conductivity of superconducting Nb, there still is a need for better correlation of the thermal conductivity with the processing history. Additionally, despite there being separate studies on the role of deformation induced dislocations on the phonon peak of large grain Nb and the role of heat treatments on the phonon and electron conductivity of polycrystal Nb, there is very little knowledge about the role of heat treatments on the thermal conductivity of deformed Nb. One study [28] examined the effect of moderate temperature ($T_{\mathrm{h}} = 750$ ℃) and high temperature ($T_{\mathrm{h}} \approx 1300$ ℃) heat treatments on the thermal conductivity of 3% strained polycrystal Nb, and noted that high temperature heat treatments were required to recover the phonon peak after deformation, despite the small strains. No such deformation-heat treatment studies exist for greater strains or large grain Nb.

In this study, the recovery of the phonon peak in undeformed mono- and bicrystal Nb are correlated with the temperature of heat treatment, and the effects of various levels of deformation and subsequent heat treatments are examined. Additionally, the influence of RRR, grain orientation, and interstitial hydrogen on phonon conductivity is studied.

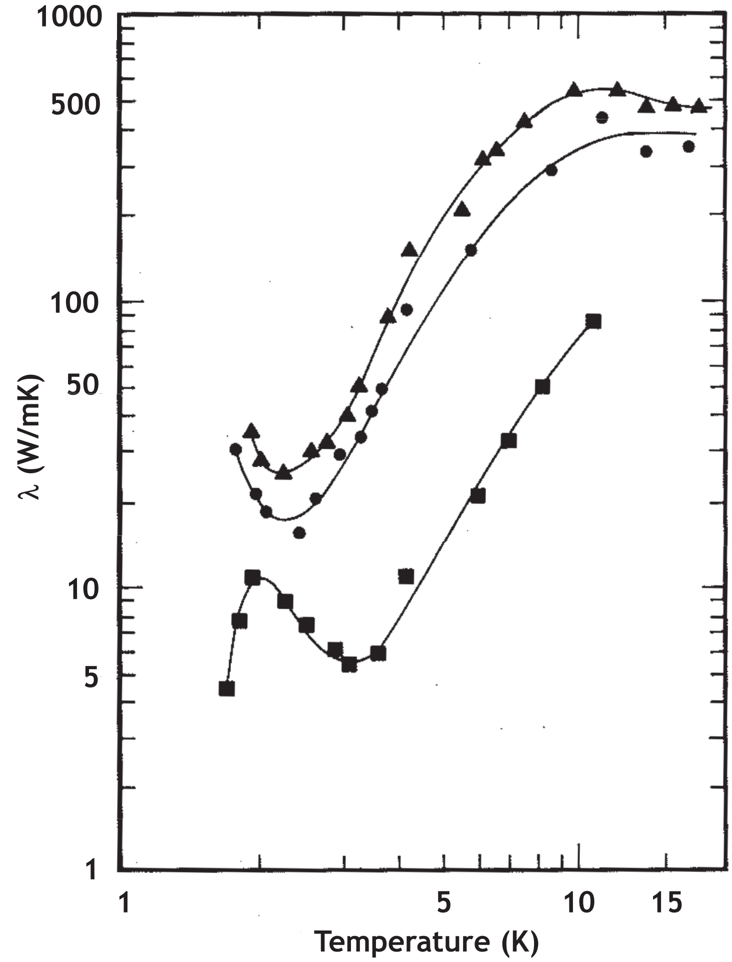

Figure 1.9: Thermal conductivity of a niobium sample after various heat treatments with and without Ti getter. 2000 ℃ for 2 h (squares), 1250 ℃ for 6 h with Ti gettering (cirles), 1300 ℃ for 10 h with Ti gettering (triangles). (Reprinted from [20], Copyright 1988, with permission from Elsevier.)

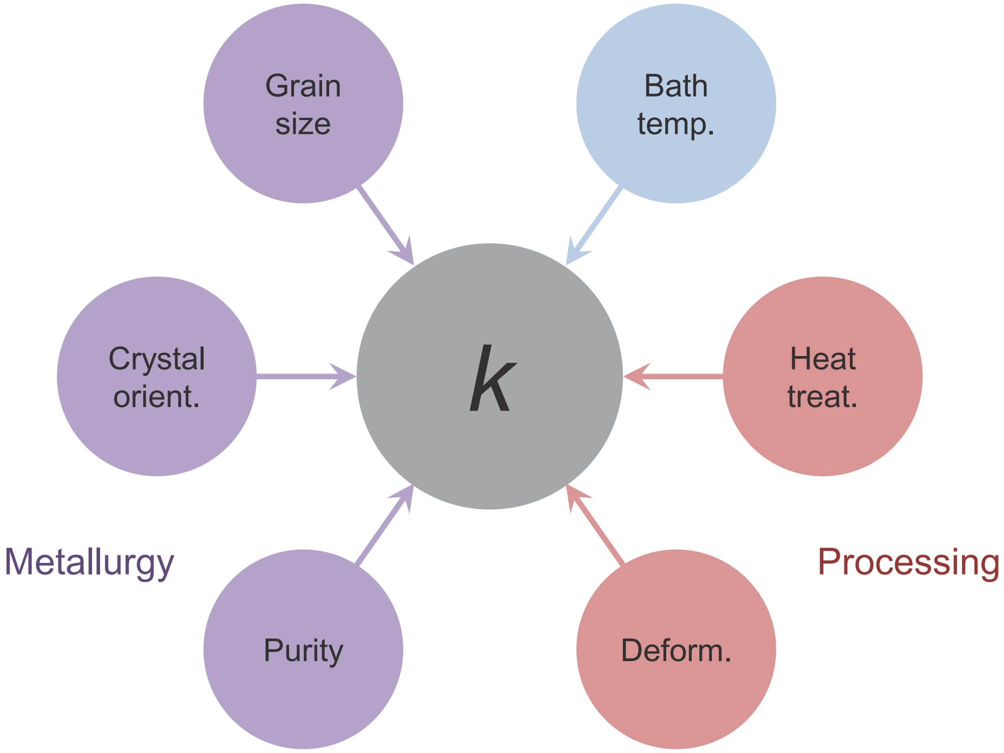

Figure 1.10: The two major groups of factors, *i.e.*, metallurgy and processing, that influence the thermal conductivity of polycrystal and large grain superconducting Nb.

Chapter 2

Thermal conductivity

2.1 Theory of Thermal conductivity

The thermal conductivity of metals is comprised of two components. The first is due to the flow of electrons in the metal (k_{e}), and the second is due to elastic thermal vibrations of the lattice, also known as phonon conduction (k_{g}). These two components are additive, and hence the total thermal conductivity (k) of any metal can be written as

$$k = k_{\mathrm{e}} + k_{\mathrm{g}}. \tag{2.1}$$

2.1.1 Electron thermal conductivity

The conductivity due to the flow of electrons in normal conducting metals (k_{en}) has two forms of resistances to its flow. The first is from the interaction of electrons with interstitial and substitutional impurities in the metal (W_{ei}), and the second is from the momentum exchange of the electrons with the lattice (W_{eg}). These resistances act in series, and can be added to get the total resistance to the conduction of electrons as

$$W_{\mathrm{en}} = W_{\mathrm{ei}} + W_{\mathrm{eg}}, \tag{2.2}$$

or,

$$\frac{1}{k_{\mathrm{en}}} = \frac{1}{k_{\mathrm{ei}}} + \frac{1}{k_{\mathrm{eg}}}. \tag{2.3}$$

The resistance due to scattering of normal electrons by impurities is inversely proportional to the temperature, due to its value being a constant [31] for a given impurity concentration. The Wiedeman-Franz law relates the impurity limited electronic thermal conductivity k_{ei} and the electrical conductivity σ of the metal to the temperature as

$$\frac{k_{\mathrm{ei}}}{\sigma} = L\,T, \tag{2.4}$$

where the constant of proportionality L is the Lorentz constant, and the electrical resistivity of the metal $\rho = \sigma^{-1}$.

The scattering of normal electrons by the lattice vibrations k_{eg} was theoretically defined in [31, 32], and was simplified in [33, 34] as

$$\frac{1}{k_{\mathrm{eg}}} = \frac{95.3\, N_a^{2/3}}{k_{295}} \left(\frac{T}{\Theta}\right)^2 = a\,T^2, \tag{2.5}$$

where N_a is the number of conduction electrons per atom, k_{295} is the thermal conductivity at room temperature (295 K), and Θ is the Debye temperature.

With the relations for k_{ei} and k_{eg} in equations (2.4) and (2.5), respectively, the expression for the total conductivity due to electrons in normal conducting metals (equation (2.3)) can be rewritten as

$$\frac{1}{k_{\mathrm{en}}} = \frac{\rho_{295}}{L\ \mathrm{RRR}\ \ T} + a\,T^2. \tag{2.6}$$

When superconducting, metals have the advantage of having zero electrical resistance when the temperature is below the superconducting critical temperature (T_{c}). However, when $T < T_{\mathrm{c}}$, electrons within the metal begin condensing into Cooper pairs [35] and do not aid in heat conduction [36]. The number of electrons forming Cooper pairs increases with decreasing temperature, with all electrons having paired up at $T = 0$ K [35]. Bardeen, Rickayzen and Tewordt [36] proposed a model for the thermal conductivity of superconductors based on the BCS theory of superconductivity [35]. To account for the effect of the condensation of electrons to form Cooper pairs on the electronic thermal conductivity of superconducting metals, they derived an expression for the ratio of the electronic thermal conductivity in the superconducting state (k_{es}) and the electronic thermal conductivity in the normal state (k_{en}) as

$$\frac{k_{\mathrm{es}}}{k_{\mathrm{en}}} = \frac{2F_1(-y) + 2y\,\ln(1 + e^{-y} + y^2/(1 + e^{y}))}{2F_1(0)}, \tag{2.7}$$

with

$$y = \frac{\Delta(T)}{k_{\mathrm{B}}T},$$

where $2\Delta(T)$ is the superconductor energy gap, and k_{B} is the Boltzmann constant. The Fermi-Dirac functions of the form $F_n(x)$ in equation (2.7) were evaluated by Rhodes [37], and were defined as

$$F_n(x) = \int_0^\infty \frac{z^n}{1 + e^{z-x}} \mathrm{d}z.$$

Koechlin and Bonin [34], for simplicity, redefined $k_{\mathrm{es}}/k_{\mathrm{en}} = R(y)$.

Hence, for superconducting metals at $T < T_\mathrm{c}$ the total thermal conductivity due to the flow of normal conducting electrons can be written as

$$k_\mathrm{es} = R(y) \left\{ \frac{\rho_{295}}{L \ \mathrm{RRR} \ T} + a\,T^2 \right\}^{-1} . \tag{2.8}$$

2.1.2 Thermal conductivity due to phonons

In normal conducting metals, the conductivity due to phonon motion k_gn is usually a negligible fraction of the electron based thermal conductivity due to the scattering of phonons by normal electrons. However, in the superconducting regime, the pairing of electrons to form Cooper pairs leads to a reduction in the electron contribution as expressed in equation (2.7) [36], and hence a reduction in the number of phonons that are being scattered. Experimentally it has been observed in superconducting metals that the phonon based conductivity k_gs becomes larger than k_es for $T \lesssim 0.3 \cdot T_\mathrm{c}$. It has also been noted that at $T = 0.2 \cdot T_\mathrm{c}$ the thermal conductivity in the superconducting metal can be greater than or equal to the thermal conductivity had the metal been normal conducting. This is depicted in [38] for the superconducting metals tantalum (Ta) and niobium (Nb). For convenience, the illustration from [38] is shown in Figure 2.1.

Similar to the electronic thermal conductivity, the phonon conduction in superconducting metals can also be expressed in terms of the different resistances or scattering mechanisms. Hulm [33] lists four scattering sources for phonons:

- normal conducting electrons,
- crystal boundaries, and specimen boundaries in the case of monocrystals,
- impurities and crystal imperfections, and

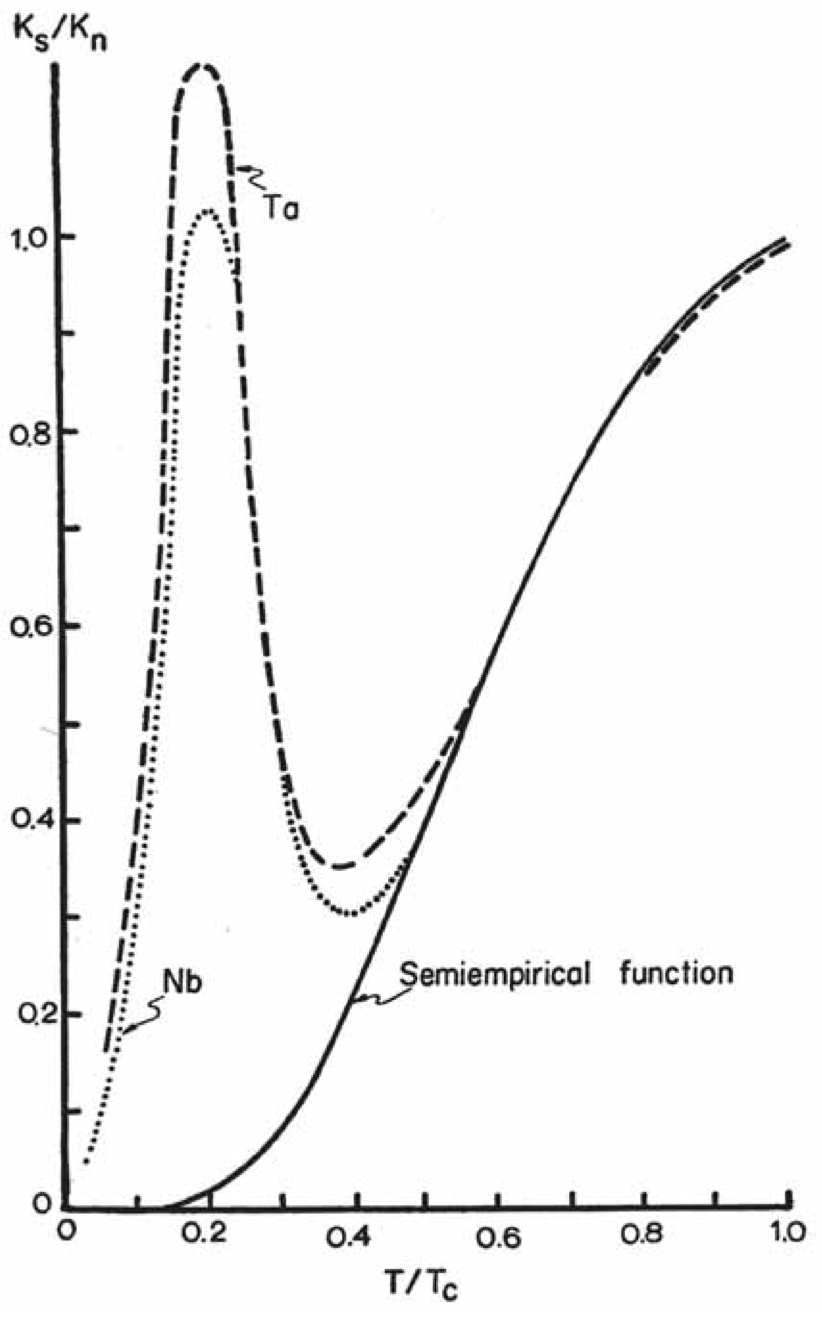

Figure 2.1: Ratio of the thermal conductivity of superconducting and normal conducting tantalum (Ta) and niobium (Nb). Note that k_s at $T = 0.2 \cdot T_\mathrm{c}$ is primarily by phonons. (Reprinted from [38], Copyright 1961, with permission from Elsevier.)

- Umklapp phonon-phonon scattering.

However, it is also pointed out that Umklapp scattering is negligible at low temperatures [33], which would be the case for superconducting metals below T_c. Hence, the phonon based thermal conductivity in superconducting metals can be expressed as

$$\frac{1}{k_\mathrm{gs}} = \frac{1}{k_\mathrm{ge}} + \frac{1}{k_\mathrm{gb}} + \frac{1}{k_\mathrm{gi}}, \tag{2.9}$$

where the subscripts s, e, b, and i indicate superconducting, electron limited, boundary limited, and imperfection limited phonon conduction, respectively.

Bardeen *et al.* [36] derived an expression for the phonon conductivity limited by electron scattering in superconducting metals k_ges. This was simplified in [34] as

$$k_\mathrm{ges} = \exp(-y)\,\frac{27\,I_3(\infty)\,k_{295}}{(2\,\mathrm{RRR}\,N_a\,\Theta)^2}\,T^2 = \exp(-y)DT^2, \tag{2.10}$$

where $\exp(-y)$ accounts for the reduction in normal conducting electrons for $T < T_\mathrm{c}$, and $I_3(\infty)$ is the third order Grüneisen integral.

The phonon conductivity limited by crystal boundary scattering was shown to have a cubic dependence on the temperature by Casimir [39], and was expressed as

$$k_\mathrm{gb}^\mathrm{c} = 2.31 \times 10^3\,RPA^{2/3}\,T^3, \tag{2.11}$$

where R is the radius for a circular cylindrical specimen, $A = C_v/T^3$ with C_v being the specific heat per unit volume, and

$$P = \frac{2\left(v_l/v_t\right)^2 + 1}{\left[2\left(v_l/v_t\right)^3 + 1\right]^{2/3}},$$

where v_l and v_t are the longitudinal and transverse velocities of sound in the material, respectively. For a specimen with square cross section d^2, R in the above equation would be replaced [39] by $R = 0.56 * d$. For specimens with a rectangular cross section, like the ones presented here, R would be replaced by $R = 0.56\sqrt{A_{\text{cs}}}$, where A_{cs} is the cross sectional area of the specimen.

Koechlin and Bonin [34] generalized the Casimir [39] expression to be valid for any form of phonon scattering other than that due to normal electrons expressed in equation (2.10). The relation given in [34] is

$$k_{\text{gb'}} = \left[\frac{1}{k_{\text{gb}}} + \frac{1}{k_{\text{gi}}}\right]^{-1} = \frac{3.6 \times 10^9}{a_\circ \Theta}\, lT^3 = BlT^3, \tag{2.12}$$

where $a_\circ$ is the lattice parameter in Å, and l is the phonon mean free length. It should be noted that the mean free length here is limited not only by Casimir boundary scattering, but also by other non-electron based phonon scattering sources.

Hence, the phonon dominant thermal conductivity of metals for $T > T_{\text{c}}$ can be written as

$$k_{\text{gs}} = \left\{\frac{1}{\exp(-y)DT^2} + \frac{1}{BlT^3}\right\}^{-1}. \tag{2.13}$$

2.1.3 Thermal conductivity of superconducting metals

The total thermal conductivity of superconducting metals for $T < T_\mathrm{c}$ can be written in the form of equation (2.1), by substituting the electron and phonon terms on the right hand side with equations (2.8) and (2.13), respectively, as

$$k_\mathrm{s} = k_\mathrm{es} + k_\mathrm{gs} = R(y)\left\{\frac{\rho_{295}}{L\ \mathrm{RRR}\ \ T} + a\,T^2\right\}^{-1} + \left\{\frac{1}{\exp(-y)DT^2} + \frac{1}{BlT^3}\right\}^{-1}. \tag{2.14}$$

It has been experimentally observed and theoretically explained that there are a few significant temperatures at which some phenomenological events occur:

1. at $T_1 \approx 0.3 * T_\mathrm{c}$, k_es and k_gs are similar in magnitude, *i.e.*, $k_\mathrm{es}/k_\mathrm{gs}{\approx}1$,
2. at $T_2 \approx 0.2 * T_\mathrm{c}$, a maximum in k_gs is noticed in "defect-free" metals, and
3. at $T_3 \approx 0.01 * T_\mathrm{c}$, Casimir boundary scattering is the dominant scatterer for k_gs.

Given the different scattering mechanisms, the following can be deduced for the conductivity in the superconducting regime: (1) For $T_1 \lesssim T < T_\mathrm{c}$, k is dominated by normal conducting electrons and the contribution from phonons is suppressed due to its scattering by the normal electrons. In this temperature range, the magnitude of k_es is limited by impurity scattering. (2) For $T_2 \lesssim T \lesssim T_1$, electrons and phonons contribute to k, and k_gs is still limited by the normal electrons. Since the number of normal electrons decreases with decreasing T, k_gs becomes the dominant mode for k in this temperature region. (3) For $T_3 \lesssim T \lesssim T_2$, the thermal conduction is almost only by phonons. The mean free lengths of the phonons are limited primarily by lattice defects, and hence are affected by the different types of dislocations and their concentration. (4) For $T \lesssim T_3$, k_gs is limited primarily by boundary scattering as calculated by Casimir [39], and has a T^3 dependence.

2.2 Thermal conductivity of superconducting niobium

The thermal conductivity of superconducting niobium has been studied with great interest due to its superconducting critical temperature ($T_\mathrm{c} = 9.25$ K) being the highest for any pure metal. This high T_c translates to the appearance of the lattice conductivity at a relatively high temperature ($T \approx 0.3 \cdot T_\mathrm{c} = 2.775$ K). The reduced electron contribution for temperatures below $T \approx 0.2 \cdot T_\mathrm{c} = 1.85$ K in niobium, enabled researchers to examine lattice defects by studying their effect on phonon conduction [24–26, 40–43]. Such studies often decouple the electron and phonon components of the thermal conductivity using theoretical relations presented in the previous sections. To study the effects lattice defects on the phonon conduction, however, the thermal conductivity needs to be dominated by defect-limited phonon conduction with minimal scattering by electrons. Hence such studies focus on the response of k_gs for undeformed and deformed specimens in the temperature regions of $T_3 \lesssim T \lesssim T_2$, *i.e.*, $0.1 \lesssim T \lesssim 1.85$ K.

Straining niobium specimens, and thereby introducing dislocations, has been shown to gradually change the temperature dependence of the phonon thermal conductivity from T^3 to T^2 depending on the level of deformation [24, 26]. The additional resistance generated due to the introduction of dislocations (either from uniaxial strain or bending) has been used to develop theoretical models for the phonon scattering mechanisms involved [25, 26, 40–47], so as to better understand the mechanics of dislocations and defects. In order to have negligible effects by the electrons, these studies focused on the conductivity of dielectrics and the conductivity of superconductors for $T < 0.1 * T_\mathrm{c}$, *i.e.*, $T \lesssim 1$ K for Nb. These studies, despite their depth into scattering mechanisms, have not provided a method to estimate the thermal conductivity of superconducting Nb after different processing steps and do not examine the recovery of the phonon peak after deformation using heat treatments. The operation of SRF cavities at temperatures hotter than the $T \lesssim 1$ K range, combined with the need for improved thermal design, necessitated the study to relate processing history with the thermal conductivity of Nb.

Chapter 3

Experimental Methods

An experimental system to measure the steady temperature profile and heat flux on as many as two specimens has been commissioned by Aizaz [48]. This system consists of an evacuated tube, one end of which is attached to a stainless steel Dewar lid, while the other end has two specimen housings. This tube-lid assembly is collectively known as the insert, and is lowered into a cryogenic Dewar that is then filled with liquid helium (He). The specimens are mounted on to conflat flanges and placed in evacuated chambers that are surrounded by liquid He, at the lower end of the evacuated tube. An illustration of the experimental insert [48] is shown in Figure 3.1. Illustrated are the various air-to-vacuum feed-throughs on the Dewar lid that are used for instruments such as the He level sensor, He bath pressure sensor, He bath temperature sensor, and cabling for temperature sensors and heaters on the Nb specimens. Also shown at the bottom of the vacuum-tube are the specimen housing for the thermal conductivity specimens. Two identical arms have been added to the system to measure up to four specimens at a time, doubling throughput. Figure 3.2 illustrates a two-dimensional CAD rendering of the experimental insert after being lowered into the Dewar [48], and highlights the structure of the cryogenic Dewar.

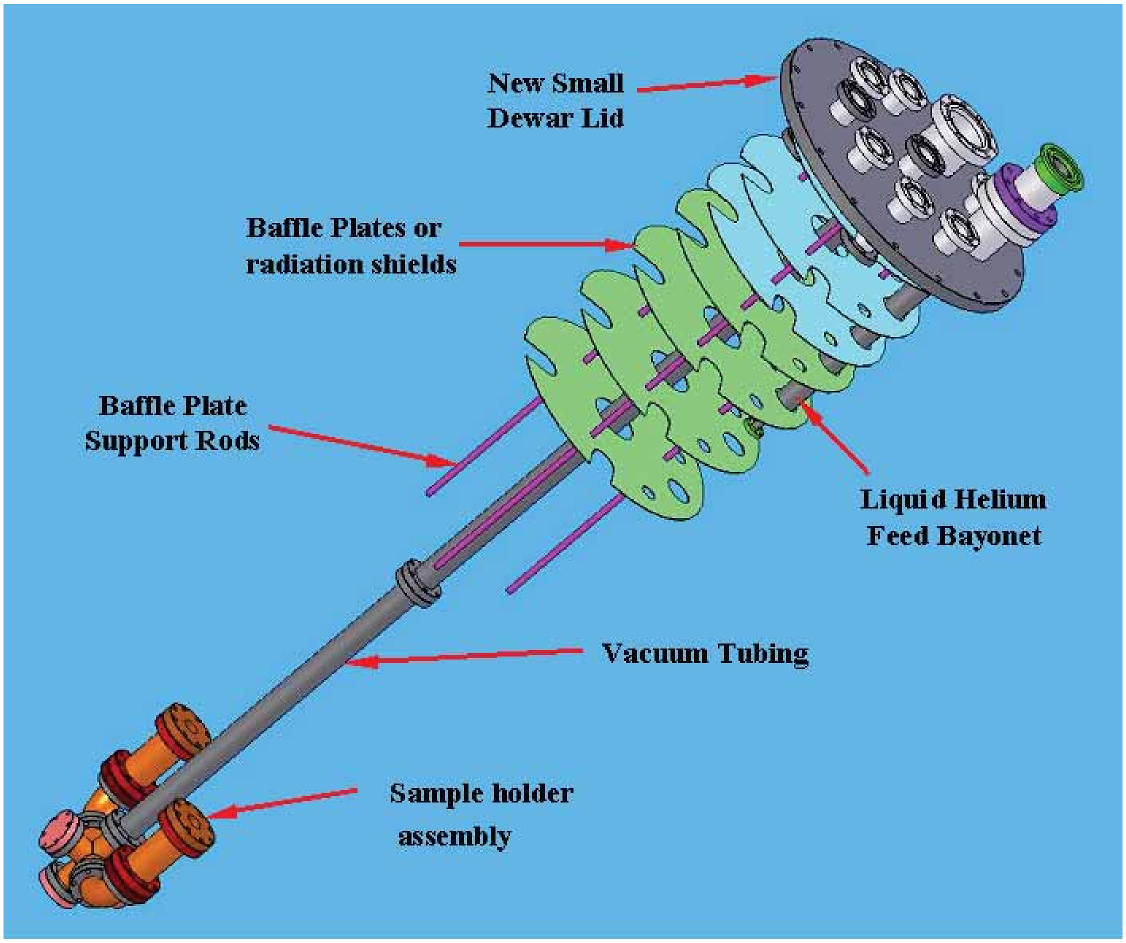

Figure 3.1: An illustration of the experimental insert [48]. Shown are the various components of the insert, including the air-to-vacuum feed-throughs on the Dewar lid, the thermal radiation shielding, and the specimen housing. For the current measurements, two identical specimen holders have been added.

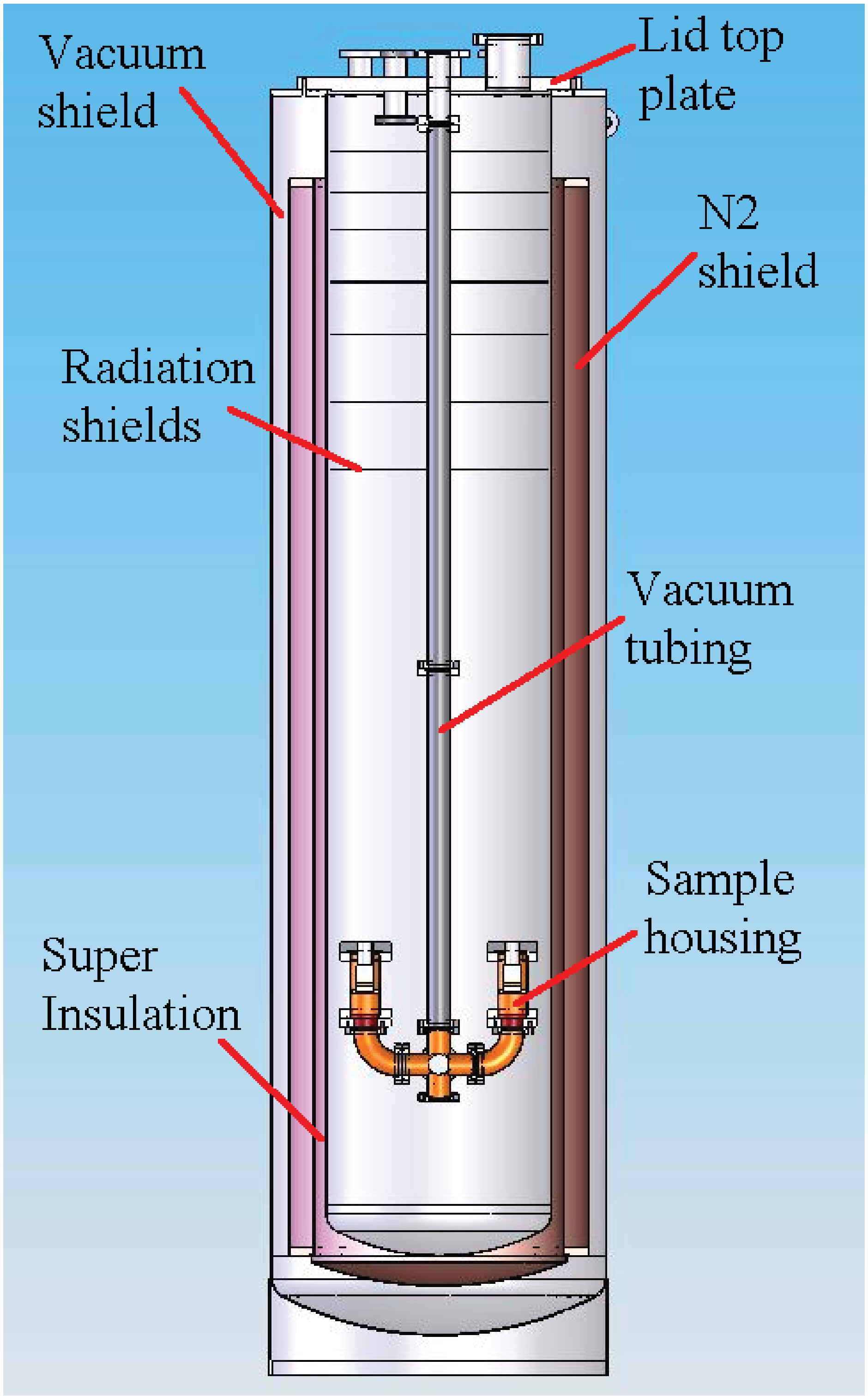

Figure 3.2: An illustration of the experimental insert, when lowered into a cryogenic Dewar [48].

3.1 Temperature measurement

Up to four Allen-Bradley 100 Ω, 1/8 W carbon resistors are used to measure the temperature gradient along the length of each specimen. Carbon resistors are favored for low temperature measurements due to their exponentially increasing resistance with decreasing temperature, along with them being relatively inexpensive.

The carbon resistors are attached to the Nb specimens using STYCAST® 2850 FT, an electrically insulating epoxy with low coefficient of thermal expansion, mixed with Catalyst 24 LV in a 100:8 ratio. This epoxy mixture has a 30 minute work life and a 16 h curing time at room temperature. A custom made fixture is used to hold the resistors in place during curing.

The resistances of the carbon and germanium resistors are measured as described by Aizaz [48]. Three LakeShore® Model 218 temperature monitors are used to measure the resistances. Each temperature monitor has eight channels, each capable of the four-lead measurement method using a 10 µA excitation current. The temperature monitors are connected to a data acquisition computer via RS-232 serial interfaces. A custom LabVIEW® program reads and records data from the temperature monitors, along with data from the He level and He bath pressure sensors. The data is recorded at 2 Hz.

The LakeShore® Model 218 temperature monitors are limited to measuring resistances up to 7,500 Ω. At temperatures colder than 1.9 K, the resistance of the carbon resistors is greater than 7,500 Ω. A 10 kΩ resistor is attached in parallel to each carbon resistor to reduce the overall resistance of the measurement circuit by limiting the current going to the carbon resistor.

The carbon resistors are calibrated for 1.6 K $\leq T \leq$ 4.6 K using a factory calibrated germanium resistor, which can be traced back to international standards. At atmospheric pressure, liquid He has a saturation temperature of 4.2 K, and sub-atmospheric pumping is required to decrease the pressure, and hence cool the liquid to 1.6 K. The pumping is done with several intermediate constant pressure periods to accommodate steady T data points for the calibration.

To reduce uncertainties due to random noise, the recorded resistances for the carbon resistors are averaged over 30 s (60 data points). This is done during data extraction for both the calibration and the thermal conductivity measurements.

3.2 Specimen heaters

A 0.3 mm thin foil heater manufactured by Minco® is used to heat one end of the specimen. It is pasted on a copper fixture to provide homogeneous heat flux to both sides of the specimen. A BK Precision® 1786B 0–32 V, 0–3 A programmable DC power supply was used to power the heaters attached to the specimens. Two Hewlett-Packard 34401a high performance bench-top multimeters were used to measure the power to the heaters, one as a voltmeter and the other as an ammeter. The multimeters had a voltage and current resolution of 1 mV and 1 µA, respectively.

3.3 Niobium specimens

Thirteen mono- and bicrystal Nb specimens were cut using wire electrical discharge machining (EDM) from several ingot slices. The ingot slices were sourced from several ingots, and thus had different RRR and tantalum contents. The specimens were shaped as tensile specimens (ASTM E8) to facilitate uniaxial deformation. A bicrystal Nb specimen positioned in

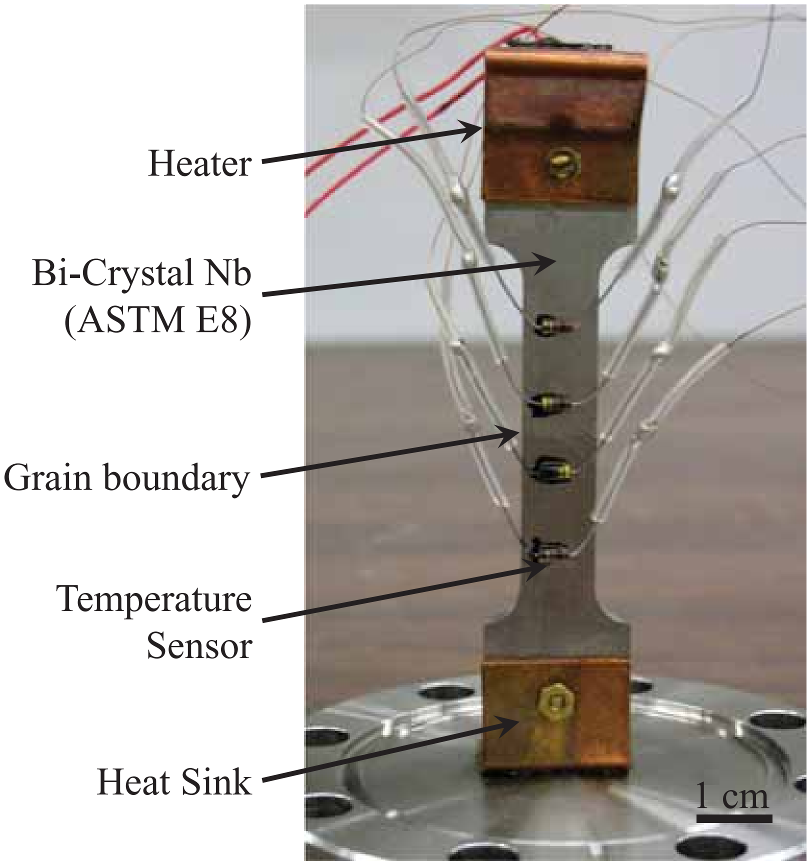

Figure 3.3: A bi-crystal Nb specimen in the holder. A steady temperature gradient is obtained on the Nb specimen using a heater on one end (top) while cooling the other side (bottom). The temperature gradient is measured using four carbon resistors positioned along the length of the specimen.

the specimen holder is illustrated in Figure 3.3. A finite electrical power is applied to the thin foil heater on one end of the specimen while the other end is attached to a cold sink (conflat flange exposed to liquid He), to obtain a temperature gradient along the length of the specimen.

Table 3.1: Processing histories of the nine bicrystal and four monocrystal specimens. The hydrogen experiment consisted of infusing hydrogen into the specimens at 300 ℃ for 1 h, at a pressure of 0.5 atm in a 75 % nitrogen, 25 % hydrogen atmosphere. These specimens were subsequently heat treated at 800 ℃ for 2 h to degas the hydrogen. The deformation experiment involved straining the specimens to different nominal engineering strains, and the specimens were later heat treated at 1000 ℃ for 2 h to examine the recovery of the phonon peak.

		Heat Treatment (HT)					
		First HT		Second HT			
Spec.	Mono- (M) or bicrystal (B)	T_{h} (℃)	t (h)	T_{h} (℃)	t (h)	Hydrogen saturated	Deformation experiment
1	B	600	6				
2	B	600	6	1100	4		✓
3	B	750	2	1100	4		✓
4	B	750	2	1100	4		
5	B	800	2			✓	
6	B	800	2				
7	B	140	48	1100	4		✓
8	B	140	48	1100	4	✓	
9	M	600	2				
10	M	800	2				
11	M	1000	2				
12	M	1200	2				
13	B						✓

3.4 Specimen processing

3.4.1 Heat treatments

After baseline measurements, several specimens were heat-treated in a high temperature, high vacuum furnace [30]. The history of heat treatments for all the specimens are tabulated in Table 3.1. Specimens 1–8 were used to investigate the response of the phonon peak to heating protocols frequently used in the SRF community, which ranged from 140 ℃ for 48 h to 800 ℃ for 2 h. Specimens 2, 3, 4, 7 and 8 were heated a second time at 1100 ℃ for 4 h, to investigate the effects of prior heat treatments and RRR on the response of the phonon peak. Specimens 9–12 were prepared to investigate the role of heat treatment temperature on the thermal conductivity, and were cut from the same grain of an ingot and the crystal orientation along the heat flow direction were chosen to be the same. These specimens were heated to different temperatures from 600–1200 ℃, all for the same peak temperature duration of 2 h.

The 750 ℃ heat treatment was carried out at the Thomas Jefferson National Accelerator Facility, in the presence of Ti getter at a heating ramp rate of 5 ℃/min. The 140 ℃, 600 ℃, 800 ℃, 1000 ℃, 1100 ℃ and 1200 ℃ heat treatments were performed in a custom built high-temperature, high-vacuum furnace at Michigan State University [30]. No getter was used for the 140 ℃ – 800 ℃ heat treatments of specimens 1, 2, and 5–8. For all other heat treatments, however, Ti getter was used. The temperature ramp rate for all of the specimens heat treated at Michigan State University was 10 ℃/min. The cooling rate was uncontrolled, and typically took about 17 h to cool from 1000 ℃ to 50 ℃. A measured temperature profile for a 1000 ℃ for 2 h heat treatment performed in this furnace is illustrated in Figure 3.4.

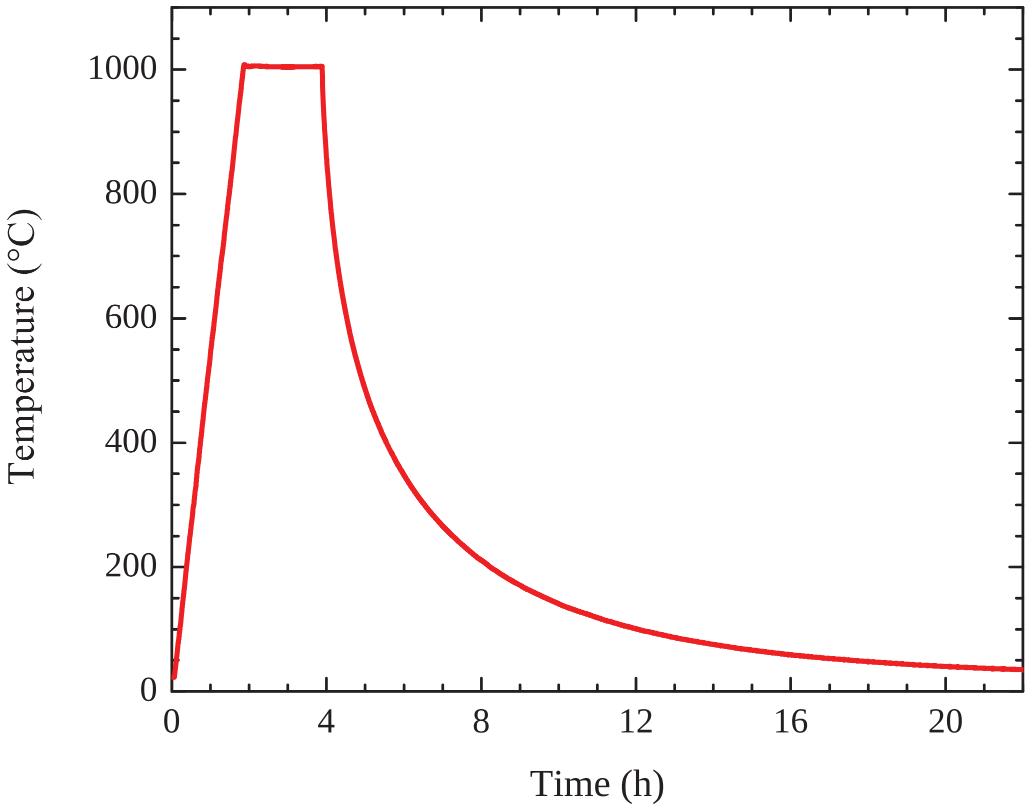

Figure 3.4: A measured temperature profile in the hot zone of the furnace at Michigan State University during a 1000 ℃ for 2 h heating. The ramp rate was 10 ℃/min, while the cooling rate was uncontrolled.

3.4.2 Deformation

Subsequent to the second heat treatment, specimens 2, 3, and 7 were strained to 20%, 10%, and 2% nominal engineering strains, respectively. Specimen 13, in its as-received condition, was strained to 2% nominal engineering strain as well. The uniaxial straining was performed in an Instron® 4302 tensile testing machine. The recovery of the phonon peak in the deformed specimens was examined by subjecting them to a 1000 ℃ for 2 h heating.

The amount of strain for each of the four specimens was chosen based on an analysis of Schmid factors and Burger's vector directions. The Schmid factor m is the result of obtaining the resolved shear stress τ for a crystal with cross-sectional area A being deformed by a force F applied in the tensile direction. The resolved shear stress is defined as

$$\tau = \frac{F}{A}\cos(\phi)\cos(\lambda) = \frac{F}{A}m, \tag{3.1}$$

where ϕ is the angle between the direction of F and slip plane normal, and λ is the angle between F and the slip direction. Although there are several slip planes in a crystal, the one with the largest Schmid factor will yield first and be dominant. Thus, grains with larger Schmid factors will deform more readily.

The Burger's vector, in simple words, represents the direction of dislocation motion in a crystal. The angle between the Burger's vector and the tensile direction of the specimen is used as an alternate measure of dislocation direction. The number of slip systems being activated during deformation can be inferred from the number of unique Burger's vector directions present for the slip planes with the largest Schmid factors.

3.4.3 Hydrogen infusion

The interaction of hydrogen with the phonon peak was examined by saturating hydrogen in specimens 5 and 8, with a subsequent degassing heat treatment at 800 ℃ for 2 h. The hydrogen was introduced into the specimens in a brazing furnace at 300 ℃ with a 75% hydrogen, 25% nitrogen gas mixture at 0.5 atm.

3.4.4 BCP etching

The specimens were etched in a 1:1:2 BCP bath at 15 ℃ to remove 15 µm, 20 µm, and 25 µm of niobium from the surface in their as-received condition, after each processing step, and after each k measurement, respectively.

3.5 Specimen metallurgy characterization

3.5.1 High energy X-ray diffraction

The imperfection densities of specimens 6–9, subsequent to the 2 h heat treatments, were qualitatively analyzed using high energy X-ray diffraction.

High energy X-ray diffraction (HEXRD) can be used for volumetric characterization of defects by using transmission X-ray diffraction [49]. Planes in the specimens that satisfy Bragg's law would diffract the X-ray beam to produce a peak on the detector. Bragg's law for X-ray diffraction states that for constructive interference to occur in the diffracted X-rays, the difference in the path lengths of the diffracted beam ($2d \sin \Theta$), where d is the inter-planar spacing and Θ is the incident angle, must equal an integer (n) multiple of the X-rays' wavelength (λ). This is illustrated in Figure 3.5. Bragg's law can thus be written

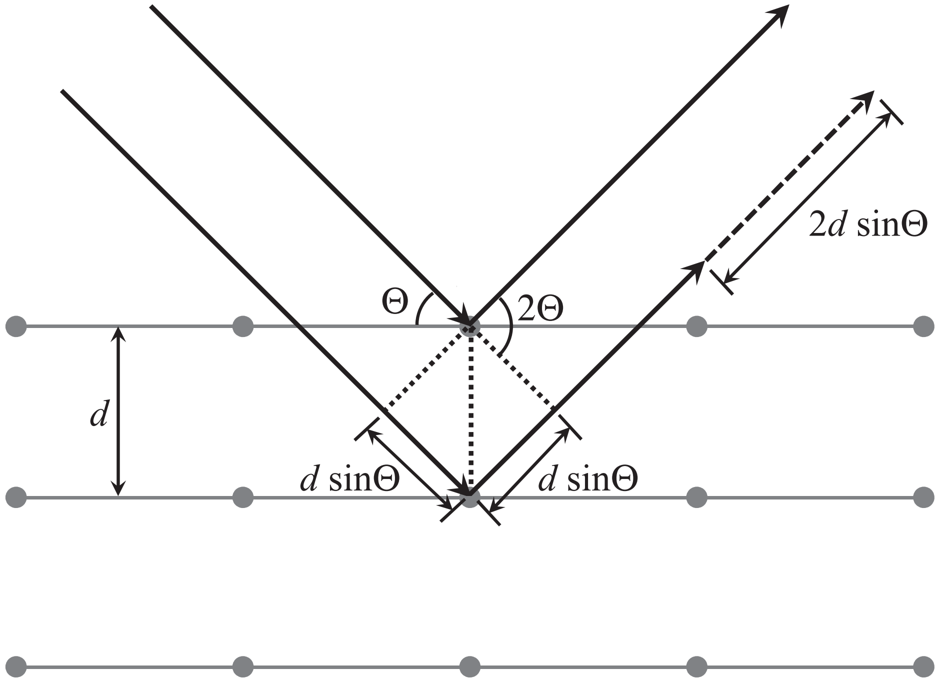

Figure 3.5: Illustration for Bragg's law for X-ray diffraction. The diffracted X-rays will produce a peak when there is constructive interference in them. For this to occur, the difference in path lengths of the diffracted beams ($2d \sin \Theta$) should equal an integer (n) multiple of the X-rays' wavelength (λ). Here, d is the inter-planar spacing and Θ is the angle of incidence of X-rays.

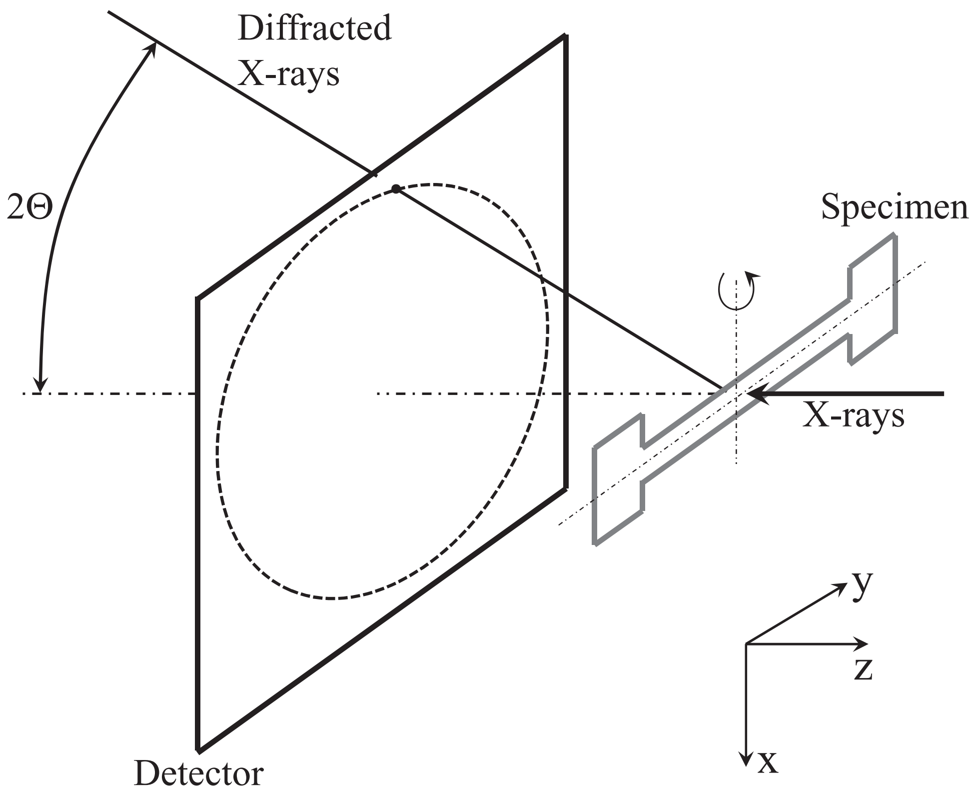

Figure 3.6: An illustration of the specimen-detector set-up at the Advanced Photon Source at Argonne National Laboratory. The diffracted X-rays were collected using an area detector having a resolution of 5 pixels/mm with 2048×2048 pixels, placed about 1 m from the specimen. Peaks observed on the detector would have satisfied Bragg's law.

as

$$n\lambda = 2d \sin \Theta. \tag{3.2}$$

The imperfection density in specimens 6–9 were estimated by HEXRD using monochromatic X-rays on beamline 6-ID-D at the Advanced Photon Source (APS), a synchrotron source, at Argonne National Laboratory (ANL). The synchrotron high energy X-rays can penetrate several mm into the metal [49], thereby making them ideal for the approximately 3 mm thick Nb specimens. An area detector, placed approximately 1 m away from the specimen, was used to collect the diffracted X-rays. The specimen-detector apparatus is illustrated in Figure 3.6. The 2Θ in Figure 3.6 is equivalent to that in Figure 3.5. The location of the center of the beam on the detector and the distance between the specimen and the detector were calibrated using a NIST 640c Si powder sample. The X-rays had energy of about 100 keV (wavelength of approximately 0.12 Å). The area detector had a resolution of 5 pixels/mm, with 2048×2048 pixels. The detector saturated at intensities greater than 14000 units.

Each of the specimens was examined at 27 locations, with the specimen being rotated 45° (±22.5°) at each location. The diffracted X-ray peak data was recorded in 60 frames per 45° sweep, *i.e.*, 0.75° per frame, thereby generating 1620 frames per specimen. One diffracted X-ray peak from a single crystal Nb specimen, as visible on the the area detector, is illustrated as a two dimensional contour plot in Figure 3.7. The same peak is illustrated in a three dimensional contour plot in Figure 3.8. Two Gaussian curves are fit to the diffracted peak in the X- and Y-directions, respectively. The location of the peak maximum and the calculated full width at half maximum (FWHM) for the detected peaks are used to analyze the defect concentration in the specimens. Peaks with intensities greater than 14000 units and intensities less than 3000 units were excluded from the analysis.

The HEXRD of the specimens were performed in collaboration with metallurgists at Michigan State University.

3.5.2 Electron backscatter diffraction

The crystal orientations of all the specimens in their as-received condition and after some of the processing were determined using electron backscatter diffraction (EBSD) in a scanning electron microscope. Diffracted electrons that satisfy the Bragg's law form Kikuchi patterns

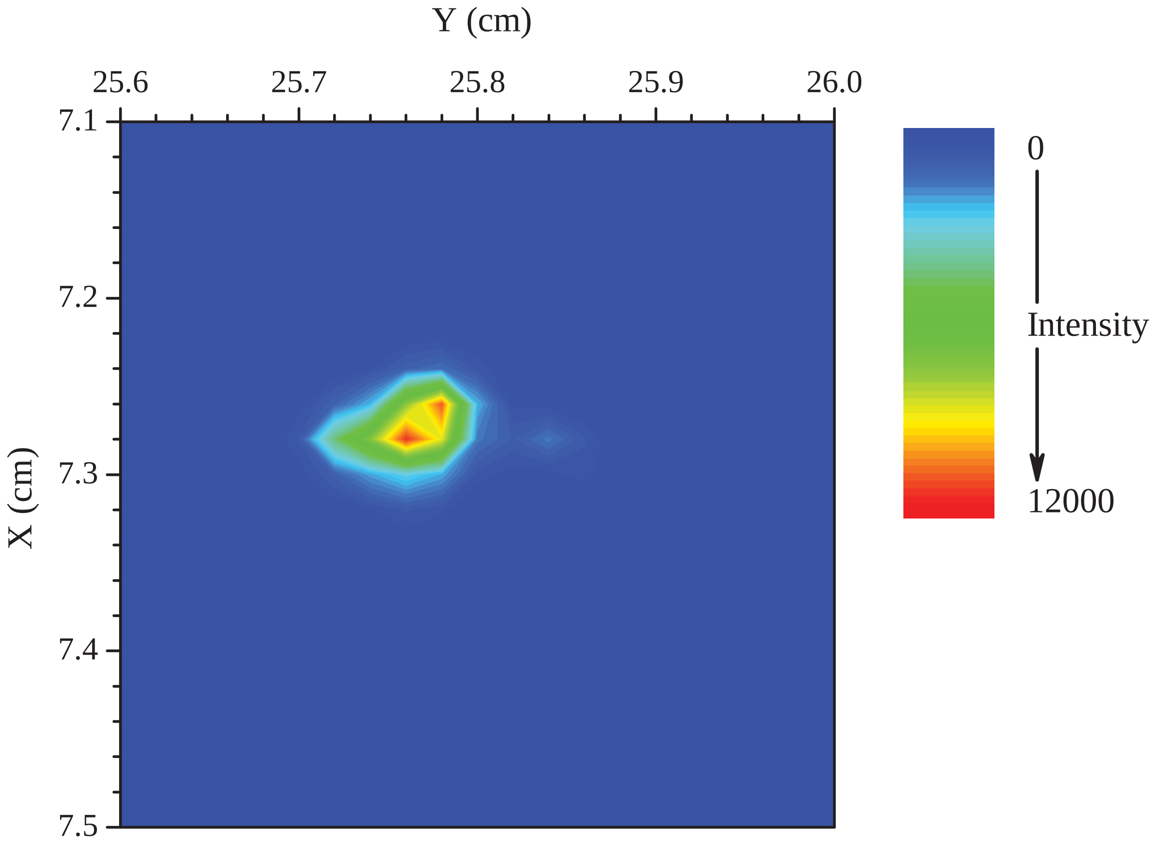

Figure 3.7: A diffracted X-ray peak from a single crystal Nb specimen measured on an area detector at the APS at ANL. A three dimensional contour plot for this peak is illustrated in Figure 3.8. The coordinate system is the same as that represented in Figure 3.6. The origin is at the top left corner of the detector.

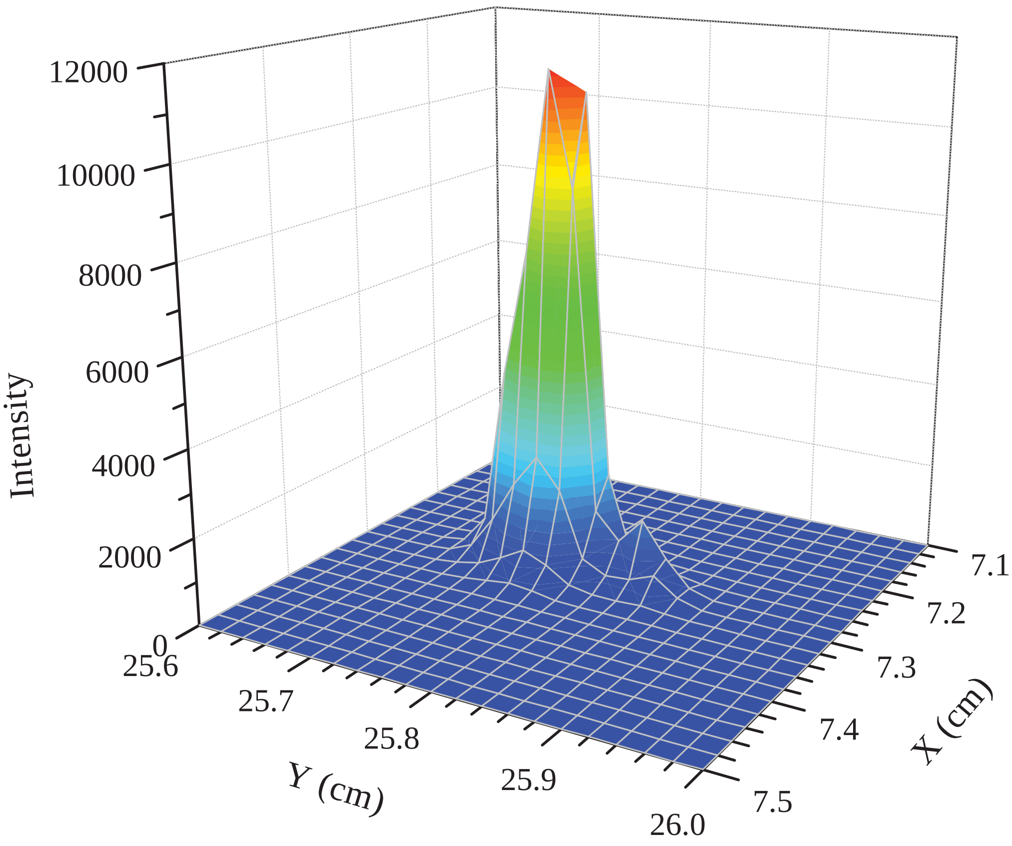

Figure 3.8: A diffracted X-ray peak from a single crystal Nb specimen measured on an area detector at the APS at ANL. A two dimensional contour plot for this peak, as would be visible on the detector, is illustrated in Figure 3.7. The coordinate system is the same as that represented in Figure 3.6.

on the detector. The process of obtaining Kikuchi patterns and automated indexing of the patterns to obtain crystal orientation is known as Orientation Imaging Microscopy$^{\mathrm{TM}}$ (OIM).

The crystal orientation obtained from OIM is represented using Bunge Euler angles, ϕ_1, Φ, and ϕ_2. The Euler angles describe the three angular rotations that are required to go from the sample reference coordinate system to the crystal coordinate system. For a sample coordinate system x, y, z, the Bunge method [50] describes the three rotations, using counter-clockwise rotation as positive, as

1. Rotate ϕ_1 about z-axis, producing new x- and y-axes (x$'$, y$'$).
2. Rotate Φ about x$'$-axis, to produce new y- and z-axes (y$''$, z$''$).
3. Rotate ϕ_2 about z$''$-axis, to arrive at the crystal coordinate system.

The OIM measurements of the specimens were performed in collaboration with metallurgists at Michigan State University.

3.5.3 Young's modulus

The Young's modulus E is an elastic constant, and is defined as the ratio of the stress σ to strain ϵ of a material during elastic deformation. According to Hooke's law, for a body under stress the strain is reversible provided the applied stress is less than the yield stress, *i.e.*, elastic deformation, and the strain is proportional to the applied stress. For a material subjected to uniaxial elastic deformation, Hooke's law can be written as

$$\epsilon = s\sigma, \tag{3.3}$$

where s is the elastic compliance constant, and is not isotropic. The Young's modulus for a crystal in the direction parallel to the unit vector l_i, $i = 1 \ldots 3$, was formulated and simplified for a cubic crystal by Nye [51] as

$$E = \left[s_{11} - 2 \left(s_{11} - s_{12} - \frac{1}{2} s_{44} \right) \left(l_1^2 l_2^2 + l_2^2 l_3^2 + l_3^2 l_1^2 \right) \right]^{-1}, \tag{3.4}$$

where s_{11}, s_{12}, and s_{44} were the non-zero components in the compliance constant matrix s_{ij}. Additional non-zero components in the s_{ij} matrix were equal to the three compliance components in equation (3.4). These equal, non-zero components are

$$\begin{aligned} s_{11} &= s_{ii},\ i = 2, 3, \\ s_{12} &= s_{ij},\ i = 1, 2,\ j = 3,\ \text{and} \\ s_{44} &= s_{ii},\ i = 5, 6. \end{aligned}$$

The values for s_{11}, s_{12}, and s_{44} for Nb between $4.2 \leq T \leq 300$ K are tabulated in [52, 53]. For Nb at 300 K [52, 53], $s_{11} = 0.6874 \times 10^{-11}$ Pa^{-1}, $s_{12} = -0.2481 \times 10^{-11}$ Pa^{-1}, and $s_{44} = 3.4130 \times 10^{-11}$ Pa^{-1}.

Hooke's law relates E with the speed of sound in the material ν as

$$\nu = \sqrt{\frac{E}{\rho}}, \tag{3.5}$$

where ρ is the density of the material. The Young's modulus is not isotropic for cubic materials [51] such as Nb due to the unit vector term in equation (3.4). The smallest value of E ($= 83.24$ GPa) is thus in the $\langle 111 \rangle$ direction, while the greatest E ($= 145.48$ GPa) is in the ⟨100⟩ crystallographic direction. Thus, ν is not isotropic and is dependent on the crystal orientation. The phonon conductivity in insulators can be estimated using the kinetic theory of gases as

$$k_{\mathrm{g}} = \frac{1}{3} C \nu l, \tag{3.6}$$

where C is the specific heat. The thermal conductivity of superconducting niobium for $T \lesssim 2$ K is dominated by phonons with minimal interaction with the electrons, similar to insulators. The phonon conductivity of superconducting Nb at 1.8 K can thus be related to E of the material, through equations (3.5) and (3.6), as

$$k_{\mathrm{g}} = \frac{1}{3} C l \sqrt{\frac{E}{\rho}}. \tag{3.7}$$

The thermal conductivity at the phonon peak for specimens that are heat treated at $T_{\mathrm{h}} \geq 1000$ ℃ are compared with E estimated using equation (3.4).

3.6 Estimating $k(T)$ from measurements

The temperature and heat flux data from the different Nb specimens are used to estimate the thermal conductivity of the specimens. For 1-dimensional heat conduction experiments, k is typically estimated using the Fourier's law of conduction as

$$q'' = -k \frac{\mathrm{d}T}{\mathrm{d}x}, \tag{3.8}$$

or,

$$k = q'' \frac{\mathrm{d}x}{\mathrm{d}T},$$

where $\mathrm{d}x$ is the distance between two sensors, and $\mathrm{d}T = T_2 - T_1$ with T_1 and T_2 being the measured temperature at sensors 1 and 2, respectively. The negative in equation (3.8) arises due to $T_2 > T_1$.

The temperature gradients from a Nb specimen during a 1.6 K thermal test is illustrated in Figure 3.9. The small temperature gradients corresponding to the low heat fluxes are typical for these bath temperatures. These small temperature gradients lead to larger uncertainties in the estimation of k. Since this study focused on the phonon conductivity of superconducting Nb, which appears for $T \lesssim 3$ K, a novel conductivity estimation technique had to be developed to reduce the effects of the smaller temperature gradients on k. This was done by utilizing the theory based model for the thermal conductivity of superconducting metals, which is described in Chapter 2, and using parameter estimation techniques to obtain parameter groups within the model.

3.6.1 Thermal conductivity estimation

In the past, researchers estimated parameters in equation (2.14) by curve fitting the model to k data points estimated using Fourier's law. This method not only contains uncertainties from T and q'' measurements, but also has additional uncertainties from the calculation of k and from the curve fitting.

An alternate method to estimate parameter groups in equation (2.14) was developed as part of the current study in [54]. This method groups coefficients of T^n in the model as

$$\beta_1 = \frac{\rho_{295}}{L\ \mathrm{RRR}}, \qquad \beta_2 = a, \qquad \beta_3 = \frac{1}{D}, \qquad \beta_4 = \frac{1}{B\lambda}, \qquad \beta_5 = \frac{\Delta(T)}{k_B T_c}, \tag{3.9}$$

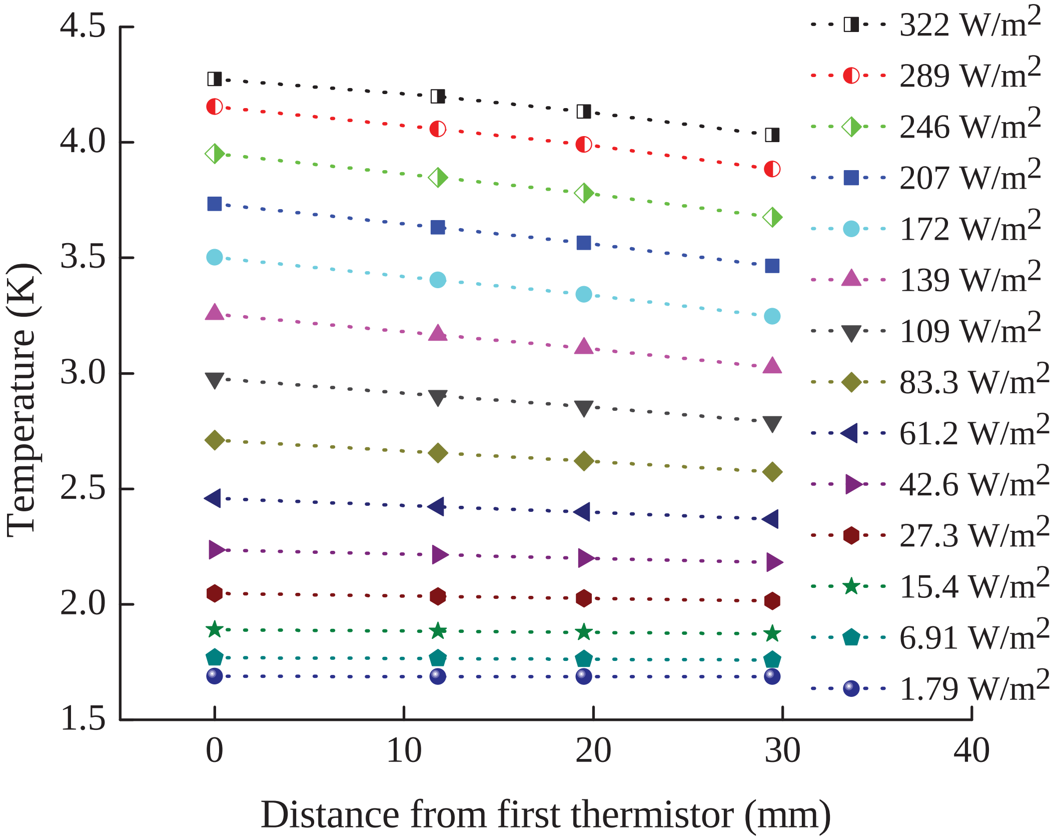

Figure 3.9: Measured temperature gradients along the length of a Nb specimen, for a bath temperature of $T_b = 1.6$ K. Also listed are the respective heat fluxes applied on the specimen to obtain the temperature gradients. Note the small gradients correspond to the low heat fluxes, thereby increasing uncertainty in the estimation of k for $1.6 \lesssim T \lesssim 2.5$ K, which is the temperature range of interest in this study.

to redefine equation (2.14) to be

$$k(T) = R(y)\left[\frac{\beta_1}{T} + \beta_2 T^2\right]^{-1} + \left[\frac{\beta_3}{\mathrm{e}^{-y}T^2} + \frac{\beta_4}{T^3}\right]^{-1}, \tag{3.10}$$

with

$$y = \beta_5 \frac{T_c}{T}.$$

As described in Chapter 2, each of the five β_i can be associated with a particular contribution to the thermal conductivity: β_1 is the contribution of purity of the metal, β_2 accounts for the scattering of electrons by the lattice and phonons, β_3 accounts for the scattering of phonons by normal conducting electrons, β_4 accounts for the scattering of phonons by lattice and specimen boundaries, and β_5 is the contribution of the condensation of electrons to k due to the formation of Cooper pairs.

3.6.2 Parameter estimation algorithm

A novel parameter estimation algorithm was developed to estimate β_is in equation (3.10) using temperature and heat flux measurements.

Applying boundary conditions of $T = T_1$ at $x = x_1$ and $T = T_2$ at $x = x_2$ for $T_1 > T_2$ on the integrated form of the conservation of energy (assuming Fourier's law), yields

$$T_1 - T_2 = q'' \int_{x'=x_1}^{x_2} \frac{1}{k\left(T\left(x\right)\right)}\,\mathrm{d}x'. \tag{3.11}$$

To estimate the five β_is, the $k(T(x))$ in equation (3.11) is substituted with the conductivity model defined in equation (3.10). Then, T_1 is assumed to be known and free of error, and equal to the measured temperature, while $\overline{T}_2$ is estimated as

$$\overline{T}_2 = T_1 - q'' \int_{x'=x_1}^{x_2} \frac{1}{k\left(T\left(x\right), \beta_i\right)} \, \mathrm{d}x' \ ; \ i = 1, 2, \ldots, 5. \tag{3.12}$$

The best estimates of β_i for the corresponding temperature and heat flux data are determined by minimizing a sum of the squares function using Gauss minimization with Box-Kanemasu interpolation to improve convergence.

3.6.2.1 Gauss minimization

The method of Gauss minimization as defined by Beck and Arnold [55], minimizes a sum of squares function (S) to yield a minima in the parameter vector (b). This method not only defines the step size for the correction of b, but also defines a direction for the correction. However, for the minimization to converge, the initial estimates for b must be in the vicinity of the minima. Beck and Arnold [55] also state that in the event that there are multiple local minima, then to estimate the overall minima of b a modification to the Gauss method of minimization must be implemented. While there are several modifications available to increase the stability of the Gauss minimization method, the one used in this study is the Box-Kanemasu interpolation method.

3.6.2.2 Scaled sensitivity analysis

Estimating correlated parameters may result in a nonconverging minimization. Scaled sensitivity coefficients (γ_i) indicate correlation between the different parameters, and are defined as

$$\gamma_i = \beta_i \frac{\partial T}{\partial \beta_i} \ ; \ i = 1, 2, \ldots, 5. \tag{3.13}$$

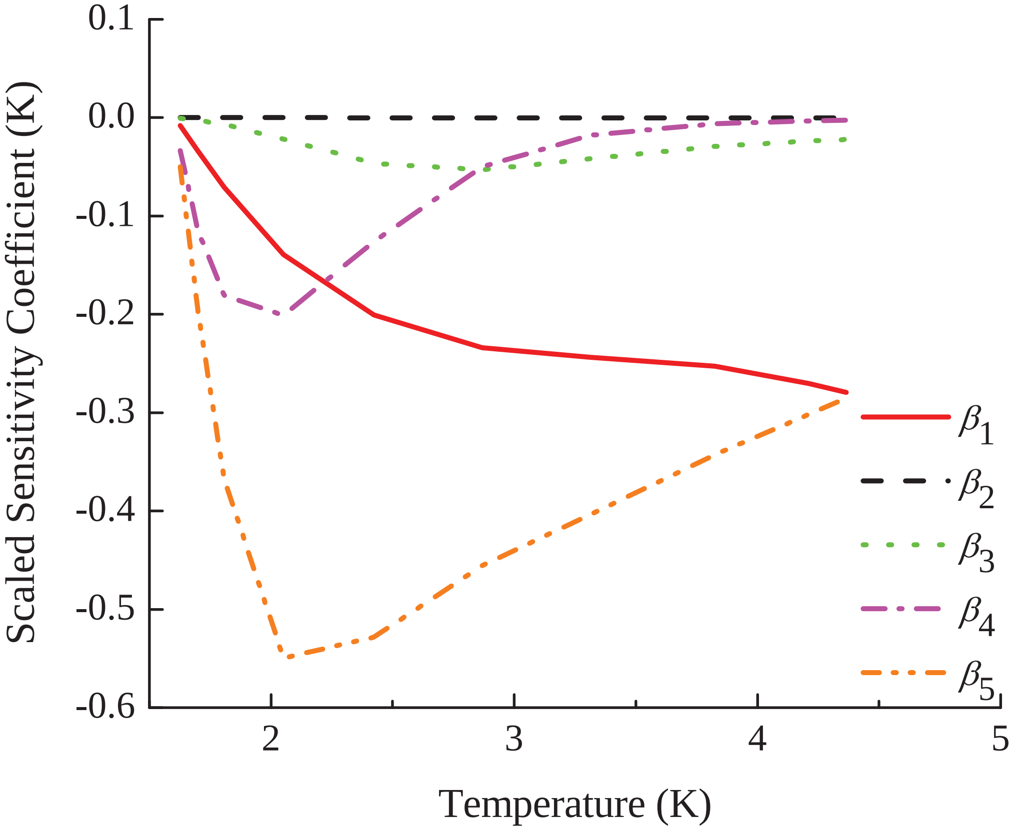

Figure 3.10: Scaled sensitivity coefficients for the five β_i defined in equation (3.9) [54].

Scaled sensitivity coefficients for the β_i are calculated for the temperature range of the measurements, $1.6\text{ K} \leq T \leq 4.6\text{ K}$ and plotted in Figure 3.10.

Curves for β_1, β_3, β_4 and β_5 in Figure 3.10 are unique and the magnitudes of the maximums are of the order of magnitude of the measured temperatures, hence these parameters can be estimated [55]. The magnitude of β_2 is too small to make reliable estimates within the measured temperatures. Thus, β_2 is not estimated, and its theoretical value [32] is used.

3.6.3 Uncertainty in k

The uncertainty in k is estimated using the Kline & McClintock method [56]. In this method the uncertainty σ for a result R, where $R = R(v_1, v_2, v_3)$ with v_1, v_2, and v_3 being independent variables, can be estimated as

$$\sigma = \sqrt{\left(\frac{\partial R}{\partial v_1}\sigma_{v_1}\right)^2 + \left(\frac{\partial R}{\partial v_2}\sigma_{v_2}\right)^2 + \left(\frac{\partial R}{\partial v_3}\sigma_{v_3}\right)^2}, \tag{3.14}$$

where σ_{v_1}, σ_{v_2}, and σ_{v_3} are the uncertainties in the independent variables v_1, v_2, and v_3, respectively.

The independent variables that implicitly influence $k(\beta_i)$ in equation (3.11) are T, x, q, and the cross-sectional area A of the specimen. The uncertainty in k can thus be written as

$$\sigma_k = \sqrt{\left(\frac{\partial k}{\partial T}\sigma_T\right)^2 + \left(\frac{\partial k}{\partial x}\sigma_x\right)^2 + \left(\frac{\partial k}{\partial q}\sigma_q\right)^2 + \left(\frac{\partial k}{\partial A}\sigma_A\right)^2}, \tag{3.15}$$

where σ_T, σ_x, σ_q, and σ_A are the uncertainties in the independent variables T, x, q, and A, respectively.

The partial derivatives of k, or the sensitivity coefficients, in equation (3.15) difficult to obtain analytically. The partial derivatives can alternately be estimated numerically by giving a small perturbation to one independent variable and observing the change in the dependent variable. For example,

$$\frac{\partial k}{\partial T} = \frac{k(T, x, q, A) - k(T + \Delta T, x, q, A)}{T - (T + \Delta T)}, \tag{3.16}$$

where ΔT is a small fraction of T, such as 0.1%.

The uncertainty in T is the combined uncertainties of the two temperature resistors that measure the temperature gradient, and is written as

$$\sigma_T = \sqrt{\sigma_{T_1}^2 + \sigma_{T_2}^2}, \tag{3.17}$$

where σ_{T_1} and σ_{T_2} are the uncertainties of the temperature measurements. The greatest contributor to uncertainty in the temperature measurements are from the interpolation polynomial used for the calibration [48].

The uncertainties in x and A arise due to length measurements taken on a digital vernier caliper with a resolution of 0.01 mm. The uncertainty in q is a function of the uncertainties in the measured current (I) and voltage (V), as

$$\sigma_q = \sqrt{\sigma_I^2 + \sigma_V^2}, \tag{3.18}$$

where σ_I and σ_V are the uncertainties of I and V respectively. The values for σ_I and σ_V are provided by the manufacturer of the multimeters used for measurements.

The uncertainty in k is estimated using data from representative specimens. The average in the uncertainty in k for the range of temperature measurement is 5%. The maximum in uncertainty is about 6%.

Chapter 4

Results: Phonon peak and heat-treatment temperature

The effect of heat treatment temperature on the magnitude of the phonon peak and dislocation content is examined in this chapter. Two sets of niobium specimens were used for this study. Set 1 comprised of eight bicrystal niobium specimens randomly cut from different ingot discs. These specimens generate data that account for variables like grain orientation, purity (RRR), and Ta content, in addition to heat treatment temperature. The specimens were heated to different temperatures and durations, ranging from 140 ℃ for 48 h to 1100 ℃ for 4 h, covering the range of heat treatments frequently used to heat treat SRF cavities. Set 2 comprised of four niobium specimens that were cut from one grain of an ingot disc and had heat transfer directions aligned along the same crystal orientation. These specimens were heated at various temperatures between 600 ℃ and 1200 ℃ for 2 h. Unlike the specimens in Set 1, the specimens in Set 2 reduce the variables in the experiment to be only the heat treatment temperature.

4.1 Set 1: Bicrystal specimens from different ingots

The specimens in Set 1 were used to explore the effects of several heat treatment parameters in combination with the variation in grain orientation, RRR and Ta contents on the magnitude of the phonon peak. After thermal measurements in their as-received conditions, specimens 1 and 2 were heated to 600 ℃ for 6 h, while specimens 3 and 4 were heated to 750 ℃ for 2 h, specimens 5 and 6 were heated to 800 ℃ for 2 h, and specimens 7 and 8 were heated to 140 ℃ for 48 h. After thermal conductivity measurements, specimens 2, 3, 4, 7, and 8 were subsequently heated a second time to 1100 ℃ for 4 h. The specimen heat treatment conditions, as well as their tantalum contents [57] and RRR estimated from k for each of the specimens, are tabulated in Table 4.1. All eight specimens presented here have a gauge length of 40 mm. Specimens 1, 5 and 6 have cross sections of 3.175×4 mm^2, while specimens 2, 3, 4, 7 and 8 have cross sections of 3.25×10 mm^2.

4.1.1 Thermal conductivities

The measured thermal conductivities of the eight bicystal specimens listed in Table 4.1, in their as-received condition and after heat treatments, are plotted as a function of T in Figures 4.1 – 4.8. The thermal conductivities of grains 1 and 2, and k across the grain boundary (GB) are illustrated in the figures by squares, circles, and triangles, respectively. The Euler angels ϕ_1, Φ, and ϕ_2 for the two grains after the hottest temperature heat treatment, as well as the inverse pole figure illustrating the orientation of the two grains, are shown below

Table 4.1: Heat treatment histories for the specimens in Set 1. Estimated RRR values, tantalum contents, and the use of Ti getter during the heat treatments of the specimens are also tabulated.

			Heat Treatment					
	Est.	**Ta content**	**First heating**			**Second heating**		
Specimen	**RRR**	**(ppm)**	$T_\mathbf{h}$ **(°C)**	t **(h)**	**Ti**	$T_\mathbf{h}$ **(°C)**	t **(h)**	**Ti**
1	191	1275	600	6	N			
2	131	668	600	6	N	1100	4	Y
3	190	756	750	2	Y	1100	4	Y
4	196	756	750	2	Y	1100	4	Y
5	104	1322	800	2	N			
6	143	523	800	2	N			
7	174	1375	140	48	N	1100	4	Y
8	200	704	140	48	N	1100	4	Y

the thermal conductivity plot in the figures. Figure 4.1 shows k as a function of T for both grains in specimen 1, in their as-received condition (open symbols) and after heat treatment at 600 °C for 6 h (half-filled symbols). The conductivity of specimen 2 in its as-received condition (open symbols), after the 600 °C for 6 h heat treatment (half-filled symbols), and after the 1100 °C for 4 h heat treatment (solid symbols) are illustrated in Figure 4.2. Figures 4.3 and 4.4 show k as a function of T for both grains of specimens 3 and 4, respectively, in their as-received condition (open symbols), after 750 °C for 2 h heat treatment (half-filled symbols), and after 1100 °C for 4 h heat treatment (solid symbols). Figures 4.5 and 4.6 show k as a function of T for both grains of specimens 5 and 6, respectively, in their as-received condition (open symbols), and after 800 °C for 2 h heat treatment (half-filled symbols). The conductivities of the two grains in specimens 7 and 8 in their as-received condition (open symbols), after the 140 °C for 48 h heat treatment (half-filled symbols), and after the 1100 °C for 4 h heat treatment (solid symbols) are illustrated in Figures 4.7 and 4.8, respectively.

These specimens are from different ingots, as suggested by their different values of RRR. For the 600 ℃ – 800 ℃ heat-treated specimens, there is very little change in the value of RRR after heat treatment, as might be expected at these relatively moderate heat treatment temperatures, even with the lack of a getter. After the 1100 ℃ heat treatment, however, there is a 10% decrease in k at 4.2 K.

A representative set of the measured thermal conductivities of specimens in Set 1 after the 1100 ℃ heat treatment are plotted as a function of temperature in Figure 4.9. Also listed in the legend of Figure 4.9 are the estimated RRR values for each of the specimens after the 1100 ℃ heat treatment.

The magnitude of increase in phonon conduction due to the first heating can be examined for the specimens by calculating the ratio k_{pp}/k_2, where k_{pp} is k at the phonon peak after heating and k_2 is k at 2 K in the specimens' as-received condition. To negate the contribution of electron conduction to the magnitude of the phonon peak, the ratio k_{pp}/k_3 is introduced for the specimens heat treated at 1100 ℃ for 4 h, where k_3 is k at 3 k after the heating. The ratios k_{pp}/k_2 and k_{pp}/k_3 for the specimens in Set 1 are listed in Table 4.2. Due to the absence of a phonon peak in k of specimens 7 and 8 after the 140 ℃ for 48 h heating, k_{pp}/k_2 are not calculated.

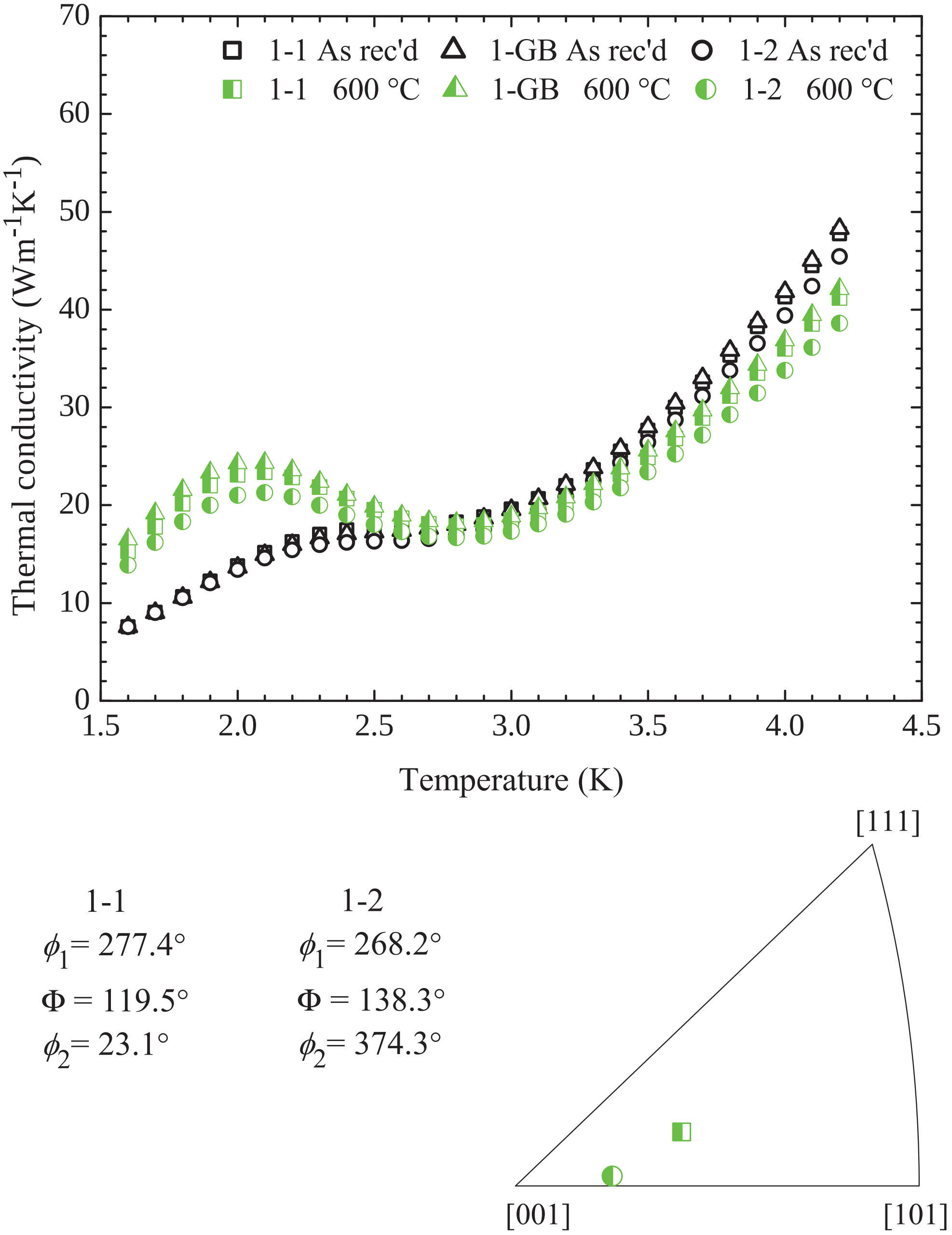

Figure 4.1: The thermal conductivities of grains 1 (squares) and 2 (circles), and across the grain boundary (triangles) of specimen 1 in their as-received condition (open symbols) and after 600 ℃ for 6 h heat treatment (half-filled symbols). The Euler angles ϕ_1, Φ, and ϕ_2 representing the crystal orientation along the heat flow direction for the two grains after the 600 ℃ heating, as well as the inverse pole figure illustrating the orientations, are shown below the thermal conductivity plot.

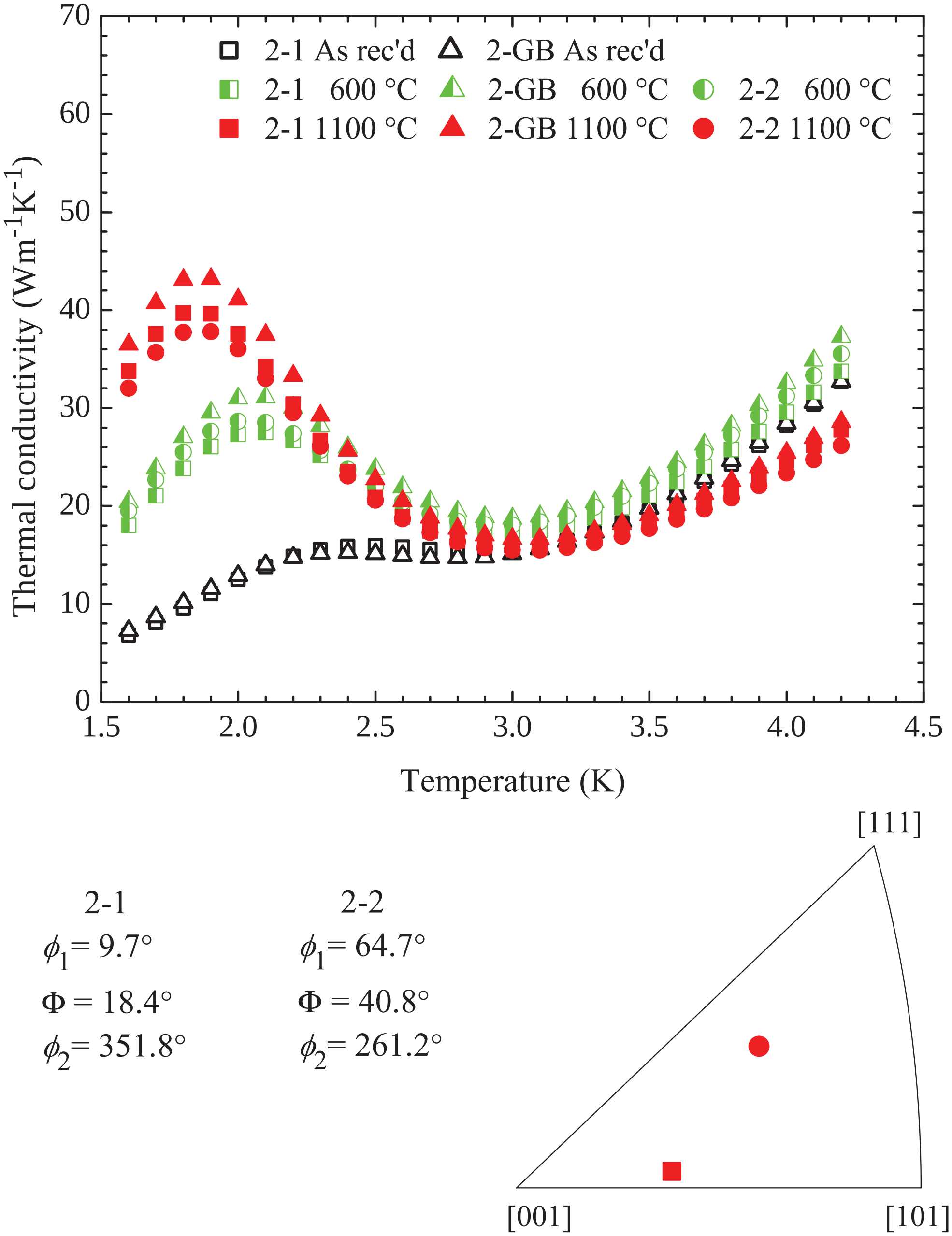

Figure 4.2: The thermal conductivities of the grains 1 (squares) and 2 (circles), and across the grain boundary (triangles) of specimen 2 in their as-received condition (open symbols), after 600 ℃ for 6 h heat treatment (half-filled symbols), and after 1100 ℃ for 4 h (solid symbols). The Euler angels ϕ_1, Φ, and ϕ_2 representing the crystal orientation along the heat flow direction for the two grains after the 1100 ℃ heating, as well as the inverse pole figure illustrating the orientations, are shown below the thermal conductivity plot.

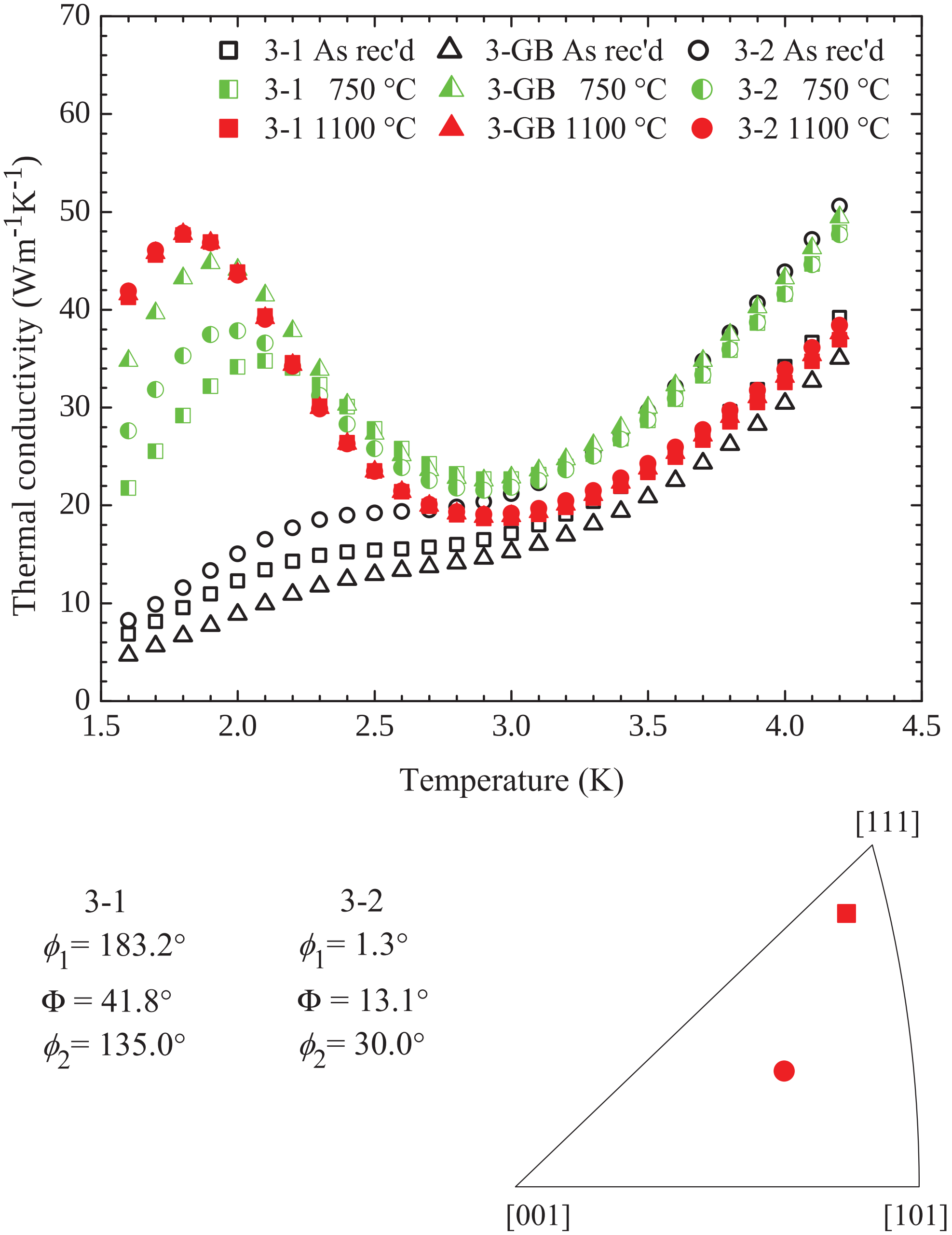

Figure 4.3: The thermal conductivities of the grains 1 (squares) and 2 (circles), and across the grain boundary (triangles) of specimen 3 in their as-received condition (open symbols), after 750 ℃ for 2 h heat treatment (half-filled symbols), and after 1100 ℃ for 4 h heat treatment (solid symbols). The Euler angels ϕ_1, Φ, and ϕ_2 representing the crystal orientation along the heat flow direction for the two grains after the 1100 ℃ heating, as well as the inverse pole figure illustrating the orientations, are shown below the thermal conductivity plot.

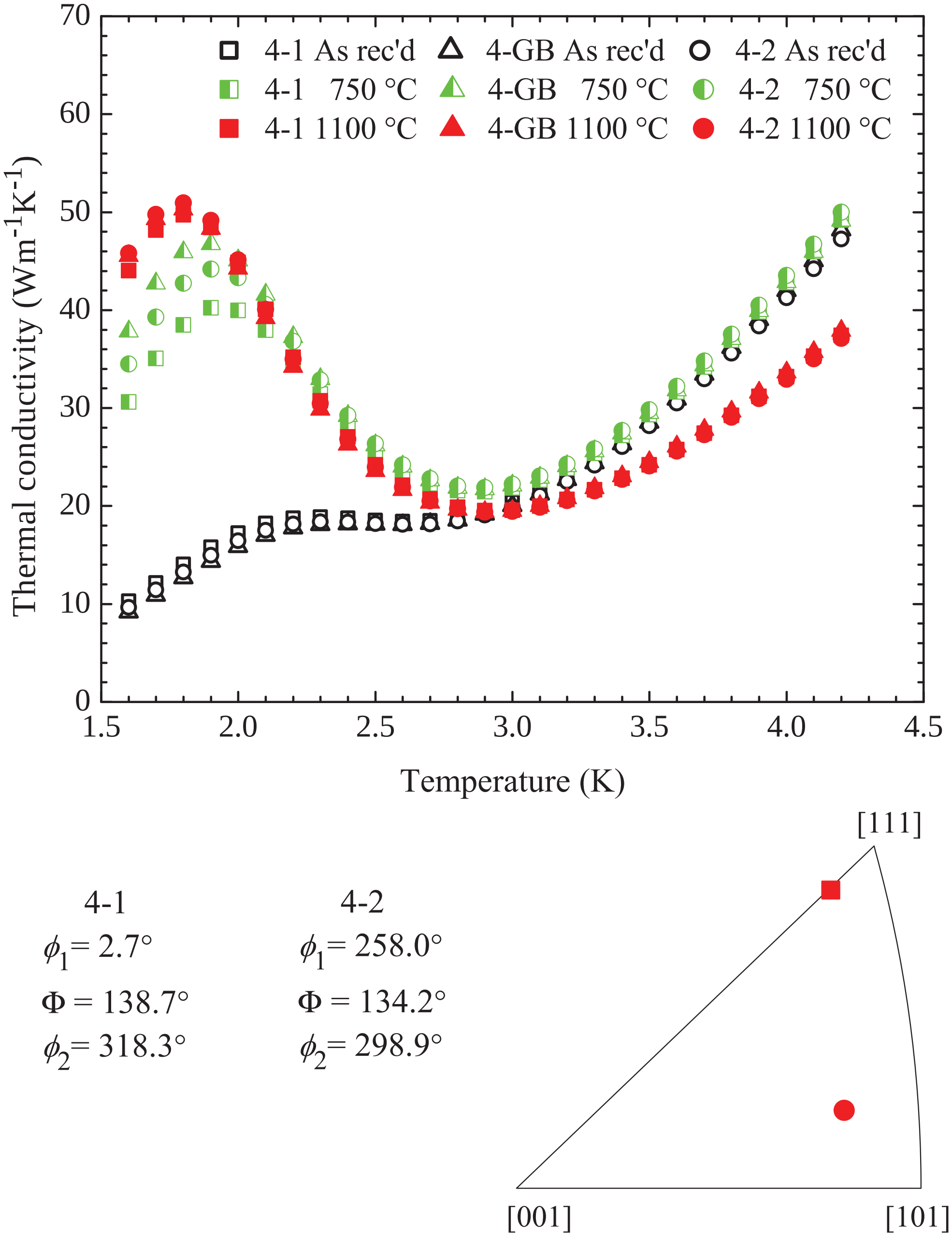

4-1
ϕ_1= 2.7°
Φ = 138.7°
ϕ_2= 318.3°

4-2
ϕ_1= 258.0°
Φ = 134.2°
ϕ_2= 298.9°

Figure 4.4: The thermal conductivities of the grains 1 (squares) and 2 (circles), and across the grain boundary (triangles) of specimen 4 in their as-received condition (open symbols), after 750 ℃ for 2 h heat treatment (half-filled symbols), and after 1100 ℃ for 4 h heat treatment (solid symbols). The Euler angels ϕ_1, Φ, and ϕ_2 representing the crystal orientation along the heat flow direction for the two grains after the 1100 ℃ heating, as well as the inverse pole figure illustrating the orientations, are shown below the thermal conductivity plot.

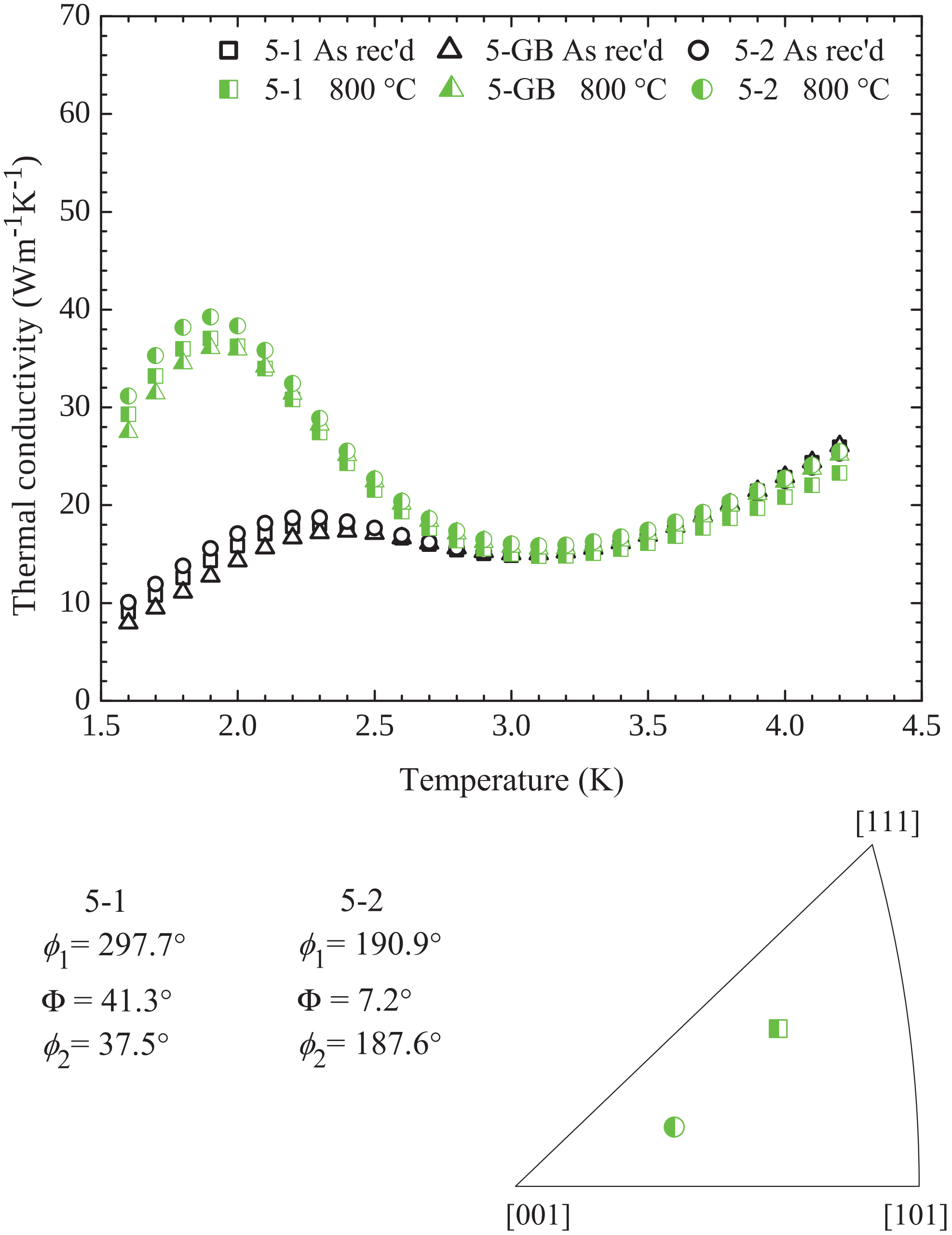

Figure 4.5: The thermal conductivities of the grains 1 (squares) and 2 (circles), and across the grain boundary (triangles) of specimen 5 in their as-received condition (open symbols) and after 800 ℃ for 2 h heat treatment (half-filled symbols). The Euler angels ϕ_1, Φ, and ϕ_2 representing the crystal orientation along the heat flow direction for the two grains after the 800 ℃ heating, as well as the inverse pole figure illustrating the orientations, are shown below the thermal conductivity plot.

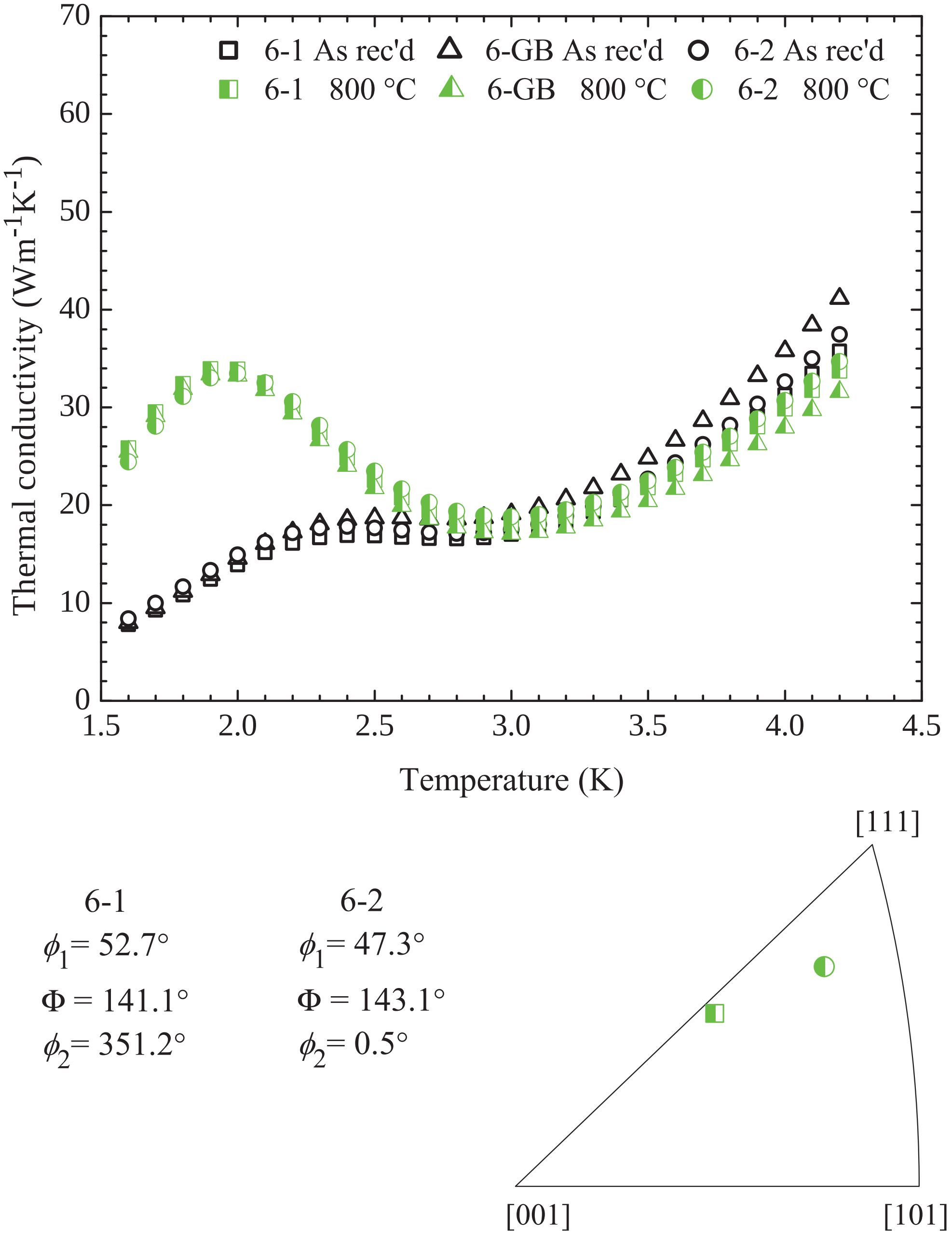

Figure 4.6: The thermal conductivities of the grains 1 (squares) and 2 (circles), and across the grain boundary (triangles) of specimen 6 in their as-received condition (open symbols) and after 800 ℃ for 2 h heat treatment (half-filled symbols). The Euler angels ϕ_1, Φ, and ϕ_2 representing the crystal orientation along the heat flow direction for the two grains after the 800 ℃ heating, as well as the inverse pole figure illustrating the orientations, are shown below the thermal conductivity plot.

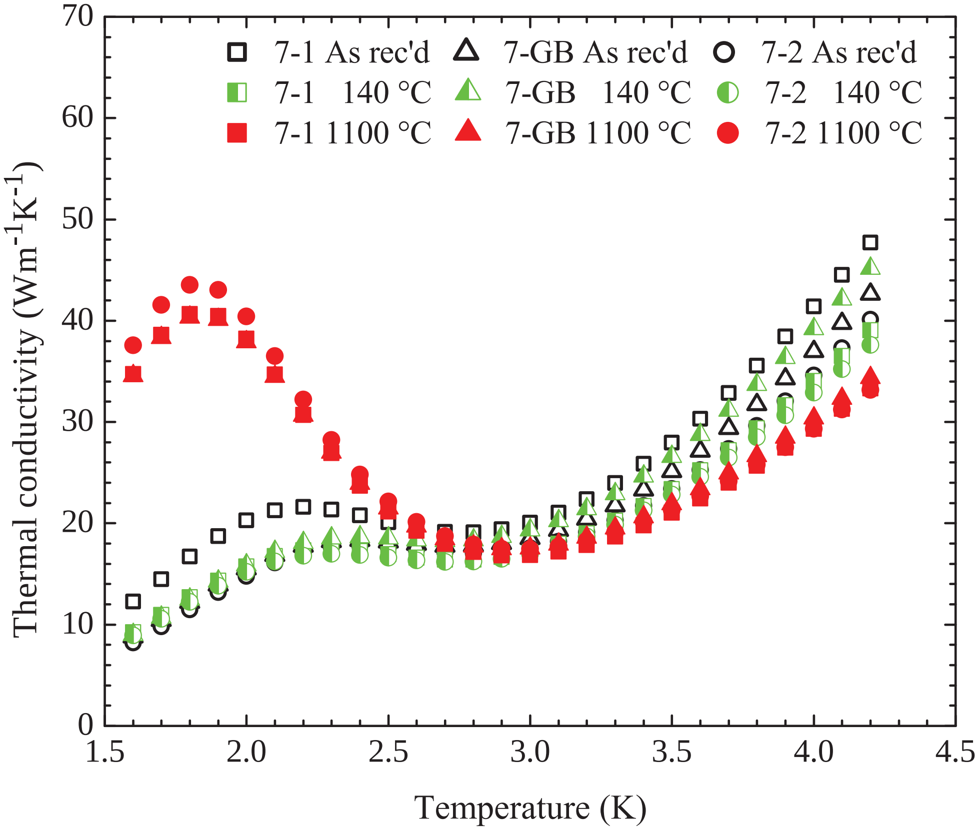

7-1	7-2
ϕ_1= 157.3°	ϕ_1= 226.2°
Φ = 40.3°	Φ = 47.0°
ϕ_2= 168.5°	ϕ_2= 172.8°

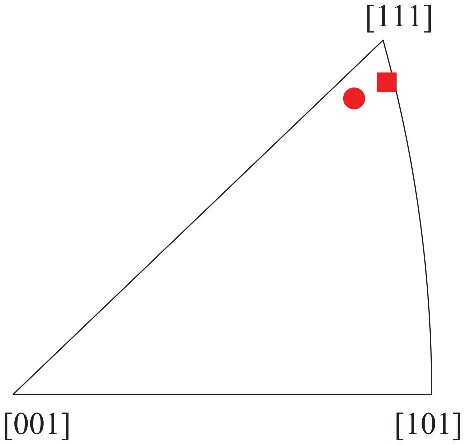

Figure 4.7: The thermal conductivities of the grains 1 (squares) and 2 (circles), and across the grain boundary (triangles) of specimen 7 in their as-received condition (open symbols) and after 140 ℃ for 48 h heat treatment (half-filled symbols), and after 1100 ℃ for 4 h heat treatment (solid symbols). The Euler angels ϕ_1, Φ, and ϕ_2 representing the crystal orientation along the heat flow direction for the two grains after the 1100 ℃ heating, as well as the inverse pole figure illustrating the orientations, are shown below the thermal conductivity plot.

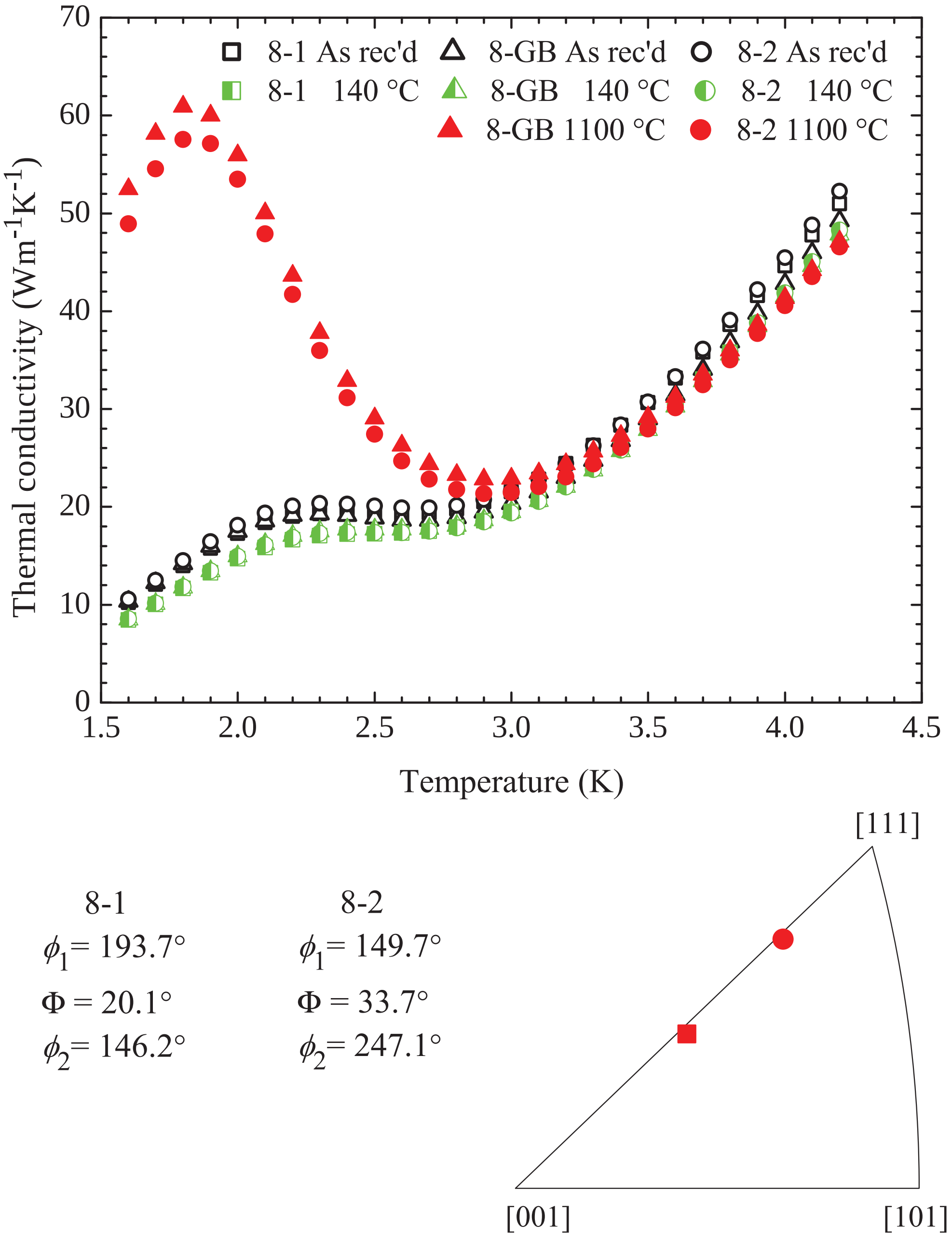

Figure 4.8: The thermal conductivities of the grains 1 (squares) and 2 (circles), and across the grain boundary (triangles) of specimen 8 in their as-received condition (open symbols), after 140 ℃ for 48 h heat treatment (half-filled symbols), and after 1100 ℃ for 4 h heat treatment (solid symbols). The Euler angels ϕ_1, Φ, and ϕ_2 representing the crystal orientation along the heat flow direction for the two grains after the 1100 ℃ heating, as well as the inverse pole figure illustrating the orientations, are shown below the thermal conductivity plot.

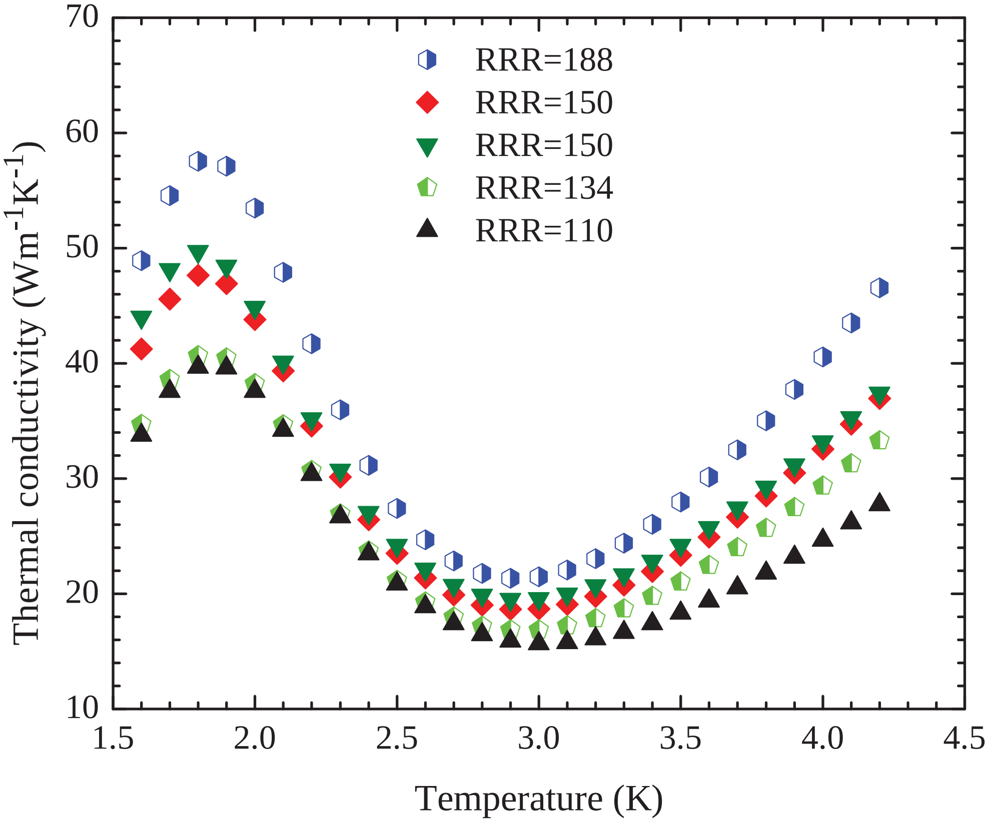

Figure 4.9: Representative thermal conductivities of the five niobium specimens in Set 1 that were heat-treated at 1100 ℃ for 4 h. The estimated RRR for each specimen after the 1100 ℃ heat treatment is listed in the legend. A dependence of maximum in k_{pp} on RRR is visible.

Table 4.2: Ratios of the phonon conductivity of the specimens in Set 1, after their two heat treatments. k_{pp} in the ratios refer to the thermal conductivity at the phonon peak after heat treatments, while k_2 refers to k at $T = 2$ K in their as-received condition, and k_3 refers to k at $T = 3$ K after the 1100 ℃ heat treatment. For specimens 7 and 8 after the 140 ℃ for 48 h heat treatment, there was no phonon peak, and hence the k_{pp}/k_2 ratios are not listed.

		First heating			**Second heating**		
Specimen	Grain	T_{h} (℃)	t_{h} (h)	k_{pp}/k_2	T_{h} (℃)	t_{h} (h)	k_{pp}/k_3
1	1	600	6	1.69			
	GB			1.78			
	2			1.58			
2	1	600	6	2.20	1100	4	2.53
	GB			2.42			2.59
	2			-			2.44
3	1	750	2	2.83	1100	4	2.55
	GB			4.99			2.52
	2			2.52			2.49
4	1	750	2	2.33	1100	4	2.54
	GB			2.95			2.58
	2			2.69			2.62
5	1	800	2	2.34			
	GB			2.53			
	2			2.30			
6	1	800	2	2.44			
	GB			2.29			
	2			2.24			
7	1	140	48	-	1100	4	2.41
	GB			-			2.30
	2			-			2.50
8	1	140	48	-	1100	4	-
	GB			-			2.66
	2			-			2.68

4.2 Set 2: Two hour heat treatment kinetics

The second set of niobium specimens were used to uncover the kinetics of two hour heat treatments. These four specimens had been cut from one grain of an ingot disc, and had the same crystal orientation along their heat flow (tensile) directions. Each specimen was subjected to a unique heat treatment temperature T_{h}, while the duration at constant T_{h} was 2 h for each specimen. Thermal measurements were performed on all of these specimens in their as-received conditions and after 2 h heat treatments. The dislocation contents of these specimens after the 2 h heat treatments were estimated using a theory-based model for dislocation density, and a qualitative analysis of the imperfection contents was performed using high energy X-ray diffraction and orientation imaging microscopy.

4.2.1 Thermal conductivities

The measured thermal conductivities of specimens 9–12 in their as-received condition (open symbols) and after the 600 ℃ – 1200 ℃ for 2 h heat treatments (half-filled symbols) are plotted as a function of temperature in Figures 4.10–4.13, respectively. The Euler angels ϕ_1, Φ, and ϕ_2 of the crystal after the hottest temperature heating, as well as the inverse pole figure illustrating the crystal orientation, are shown below the thermal conductivity plot. For comparing the thermal conductivities of the specimens in Set 2 illustrated in Figures 4.10–4.13, one k curve for each specimen in its as-received condition and after the 2 h heat treatments are plotted as a function of temperature in Figure 4.14. Although there is a significant increase in k in the phonon dominated regime, there is a 10% and 20% decrease in k at $T = 4.2$ K after the 1000 ℃ and 1200 ℃ heat treatments, respectively. This indicates introduction of some impurities into the specimen during the 1000 ℃ and 1200 ℃

heat treatments.

To reduce the influence of the RRR of heat-treated specimens on the perception of their phonon response, the ratio k_{pp}/k_3 is examined for specimens in Set 2. The ratio k_{pp}/k_3 for these specimens in their as-received condition (25 ℃) and after heat treatments (squares) is plotted in Figure 4.15. A sigmoidal curve was found to best fit the data from specimens in Set 2, and is illustrated as the solid line in Figure 4.15. Also plotted are the k_{pp}/k_3 for the niobium specimens of Set 1 heat-treated at 1100 ℃ for 4 h (triangles).

4.2.2 Dislocation content

A quantitative comparison of the dislocation contents of specimens 9 – 12 was performed using the magnitude of the phonon peak and the theoretical phonon peak limited by specimen boundary scattering as defined by Casimir [39]. A qualitative comparison of the concentration of imperfections in the lattice was done using local average misorientation (LAM) data from the orientation gradient maps for the surfaces of the specimens. Bulk measurements were made using peak spread and full width at half maximum (FWHM) information from high-energy X-ray diffraction measurements. While the local average misorientation data represents the surface only, the data from the high-energy X-ray diffraction is a bulk measurement.

4.2.2.1 Dislocation density from k_{pp}

A method to estimate the density of randomly distributed dislocations N_{d} in metals using lattice conductivity was presented by Klemens [58], and was simplified for Nb by Wasserbäch [26] as

$$\frac{W_{\mathrm{gd}}\, T^2}{N_{\mathrm{d}}} = 3.05 \times 10^{-15}\ \mathrm{m^3K^3/watt}, \tag{4.1}$$

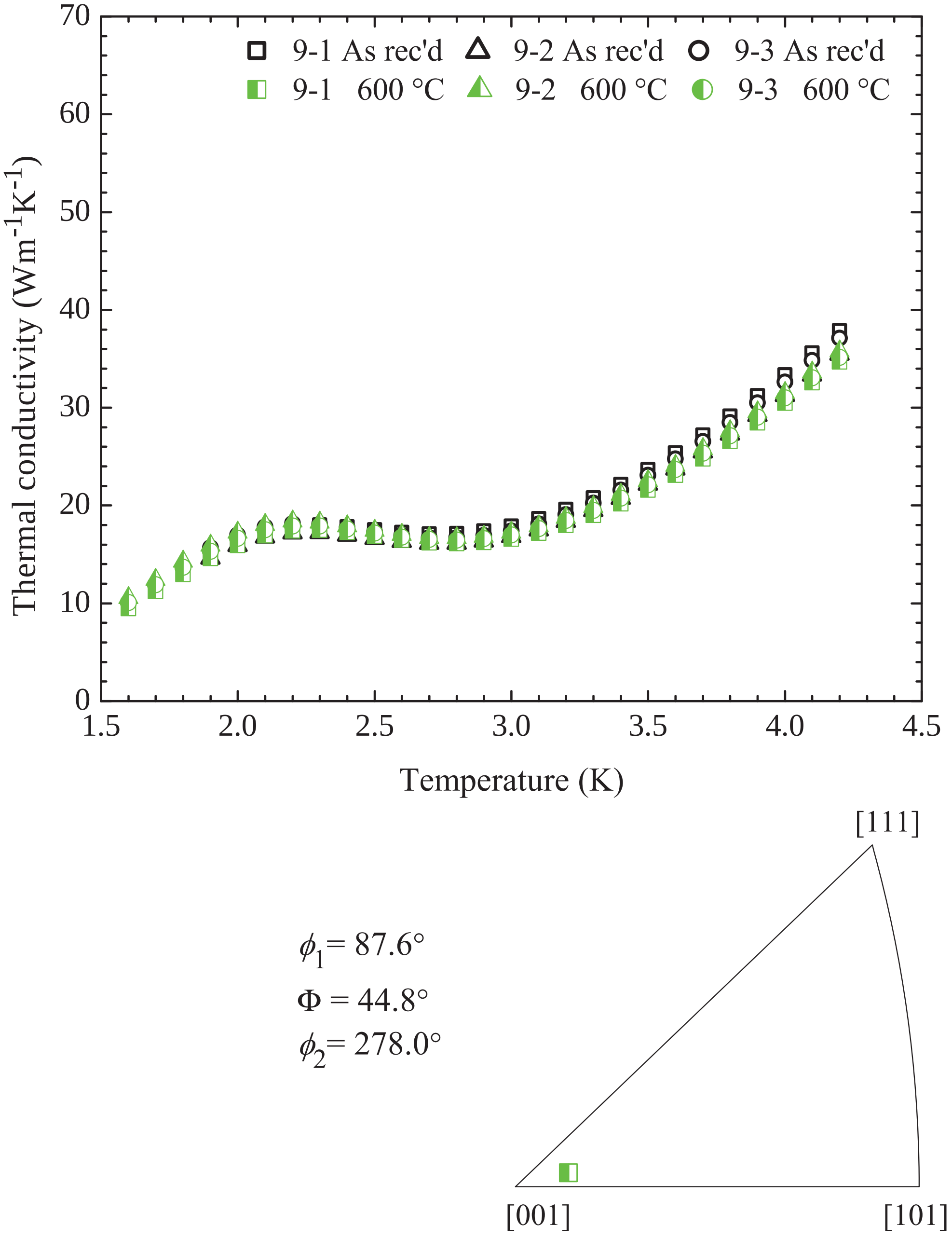

Figure 4.10: Thermal conductivity curves for specimen 9 in its as-received condition (open symbols) and after the 600 ℃ for 2 h heating (half-filled symbols). The three curves for each condition are the k for each T sensor pair on the single crystal specimen. The Euler angels ϕ_1, Φ, and ϕ_2 representing the crystal orientation along the heat flow direction for the specimen after the 600 ℃ heating, as well as the inverse pole figure illustrating the crystal orientation, are shown below the thermal conductivity plot.

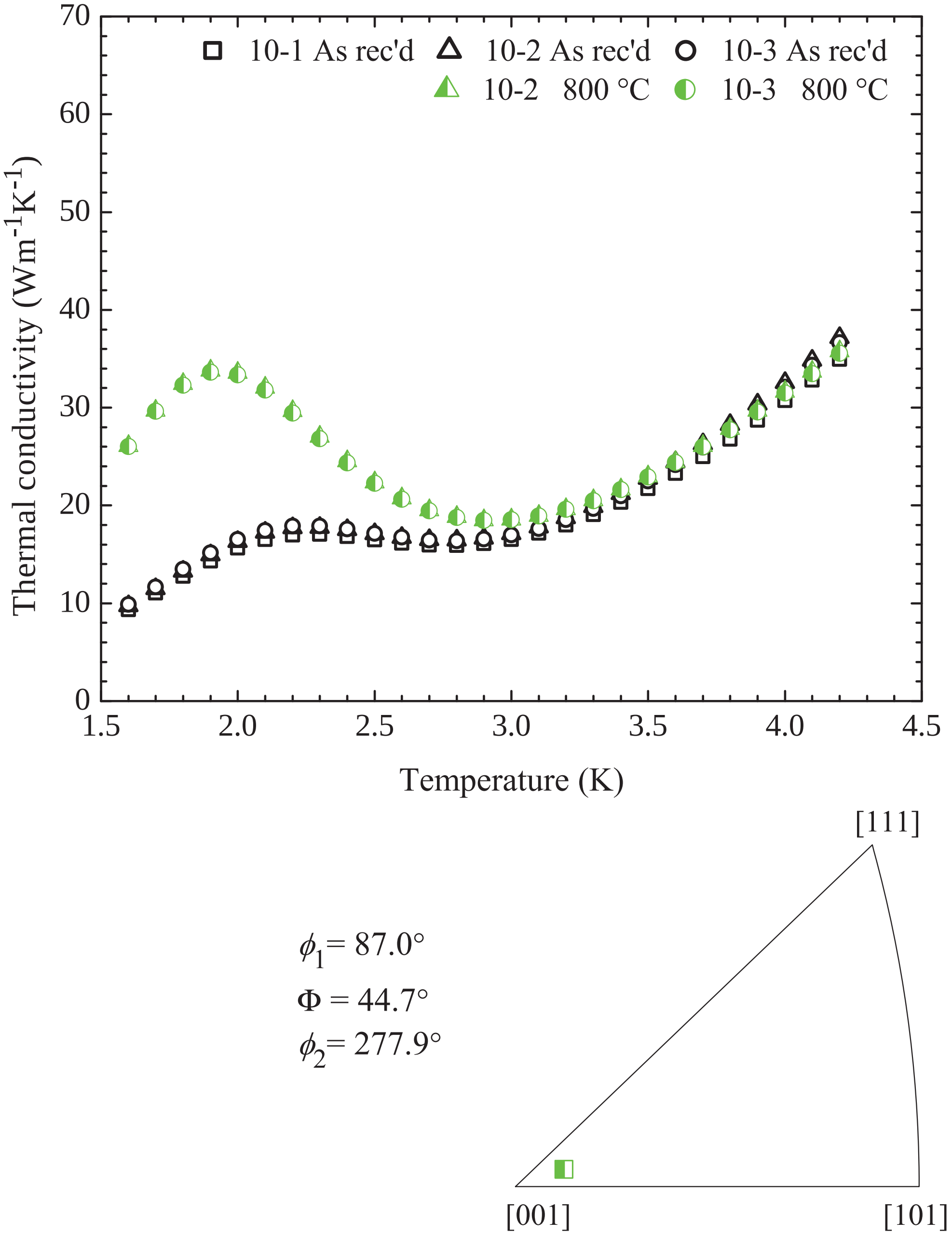

Figure 4.11: Thermal conductivity curves for specimen 10 in its as-received condition (open symbols) and after the 800 ℃ for 2 h heating (half-filled symbols). The three curves for each condition are the k for each T sensor pair on the single crystal specimen. The Euler angels ϕ_1, Φ, and ϕ_2 representing the crystal orientation along the heat flow direction for the specimen after the 800 ℃ heating, as well as the inverse pole figure illustrating the crystal orientation, are shown below the thermal conductivity plot.

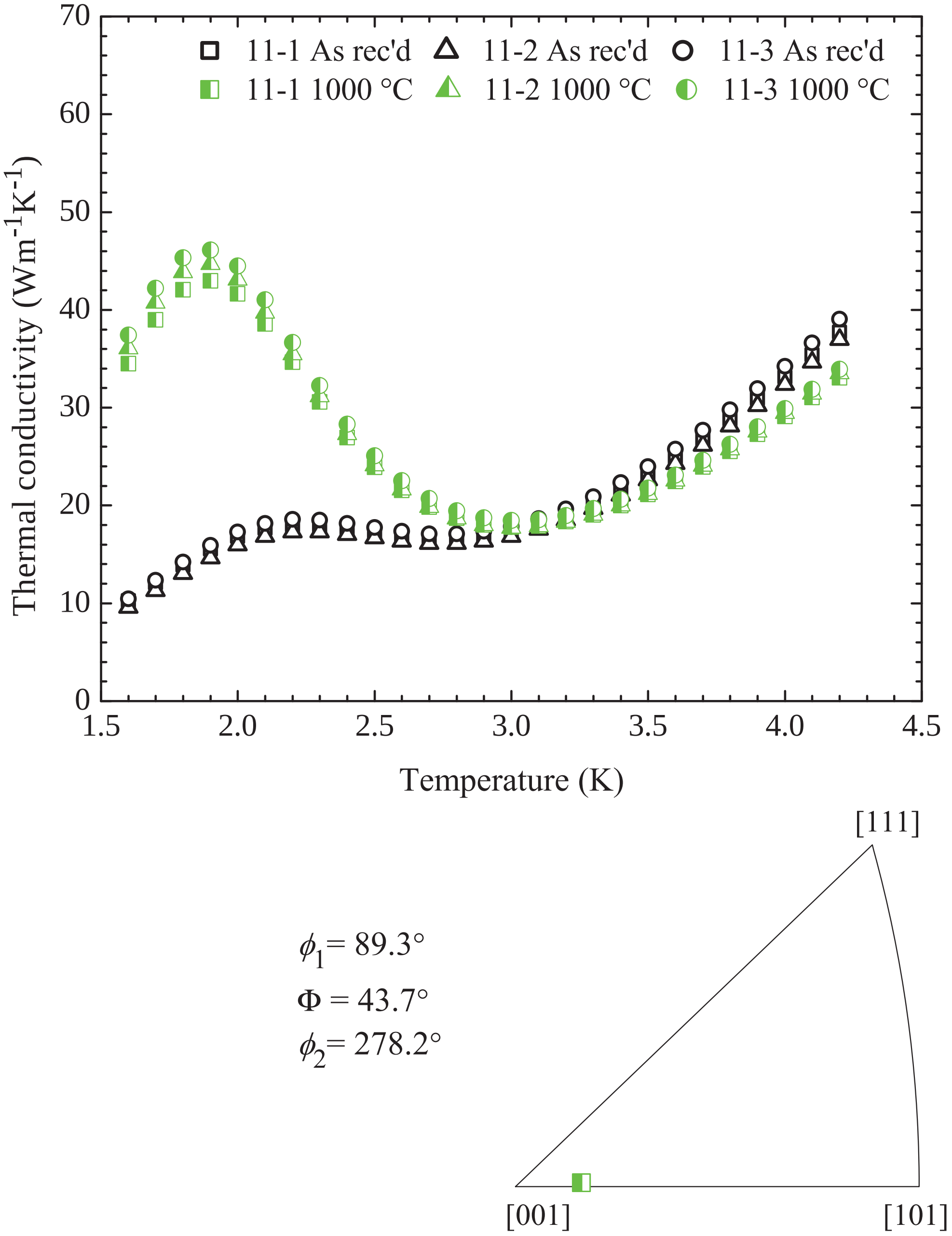

Figure 4.12: Thermal conductivity curves for specimen 11 in its as-received condition (open symbols) and after the 1000 ℃ for 2 h heating (half-filled symbols). The three curves for each condition are the k for each T sensor pair on the single crystal specimen. The Euler angels ϕ_1, Φ, and ϕ_2 representing the crystal orientation along the heat flow direction for the specimen after the 1000 ℃ heating, as well as the inverse pole figure illustrating the crystal orientation, are shown below the thermal conductivity plot.

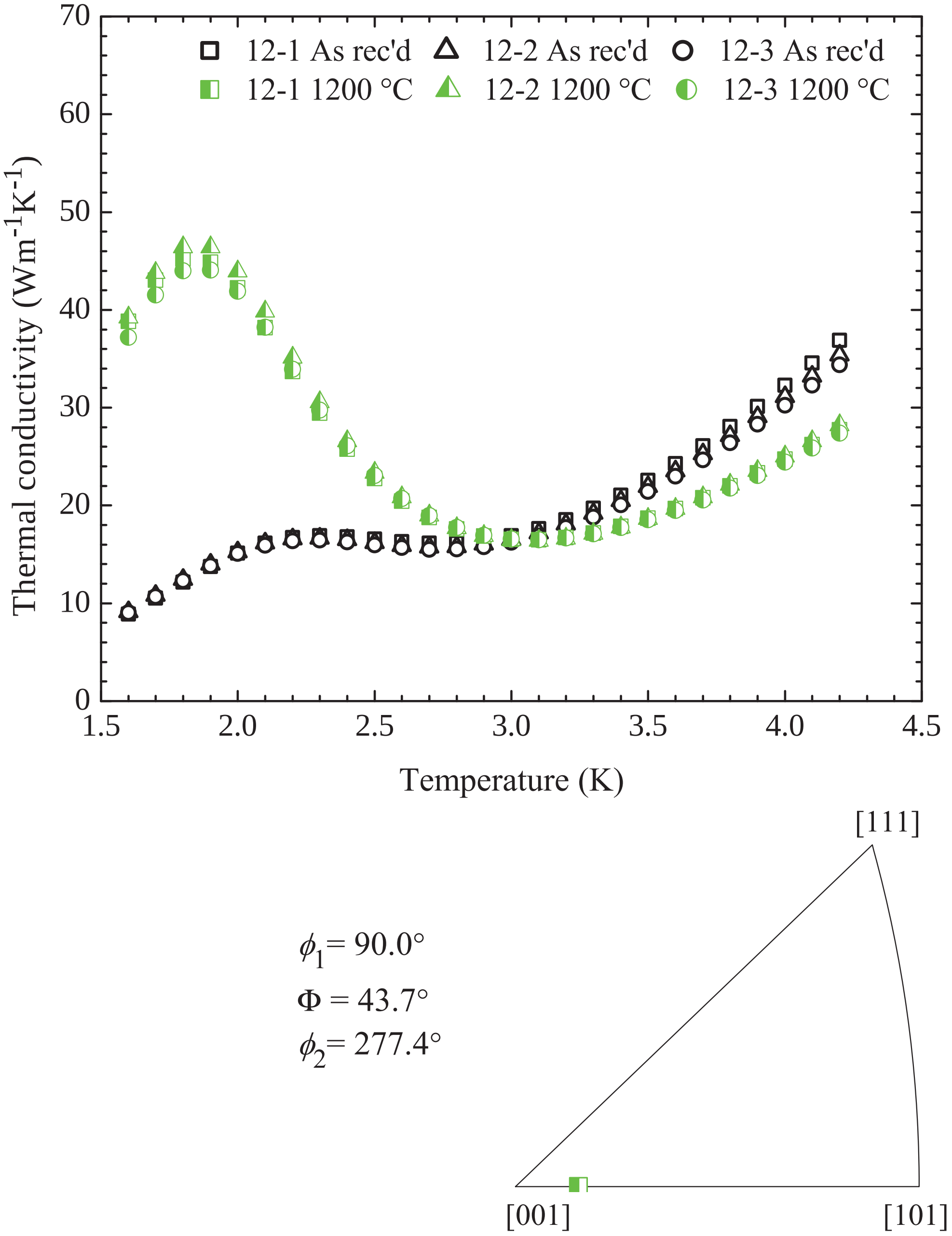

Figure 4.13: Thermal conductivity curves for specimen 12 in its as-received condition (open symbols) and after the 1200 ℃ for 2 h heating (half-filled symbols). The three curves for each condition are the k for each T sensor pair on the single crystal specimen. The Euler angels ϕ_1, Φ, and ϕ_2 representing the crystal orientation along the heat flow direction for the specimen after the 1200 ℃ heating, as well as the inverse pole figure illustrating the crystal orientation, are shown below the thermal conductivity plot.

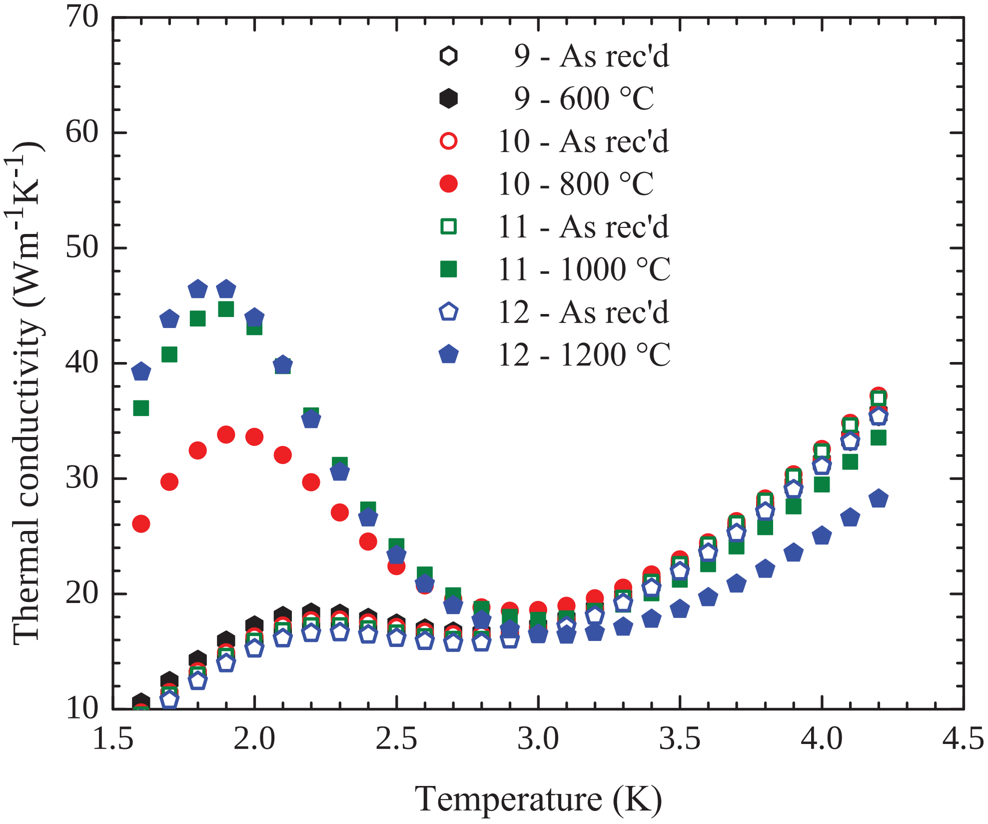

Figure 4.14: Comparison of the thermal conductivities of the four niobium specimens in Set 2 in their as-received condition and after 2 h heat treatments. For clarity, only one curve per specimen is plotted.

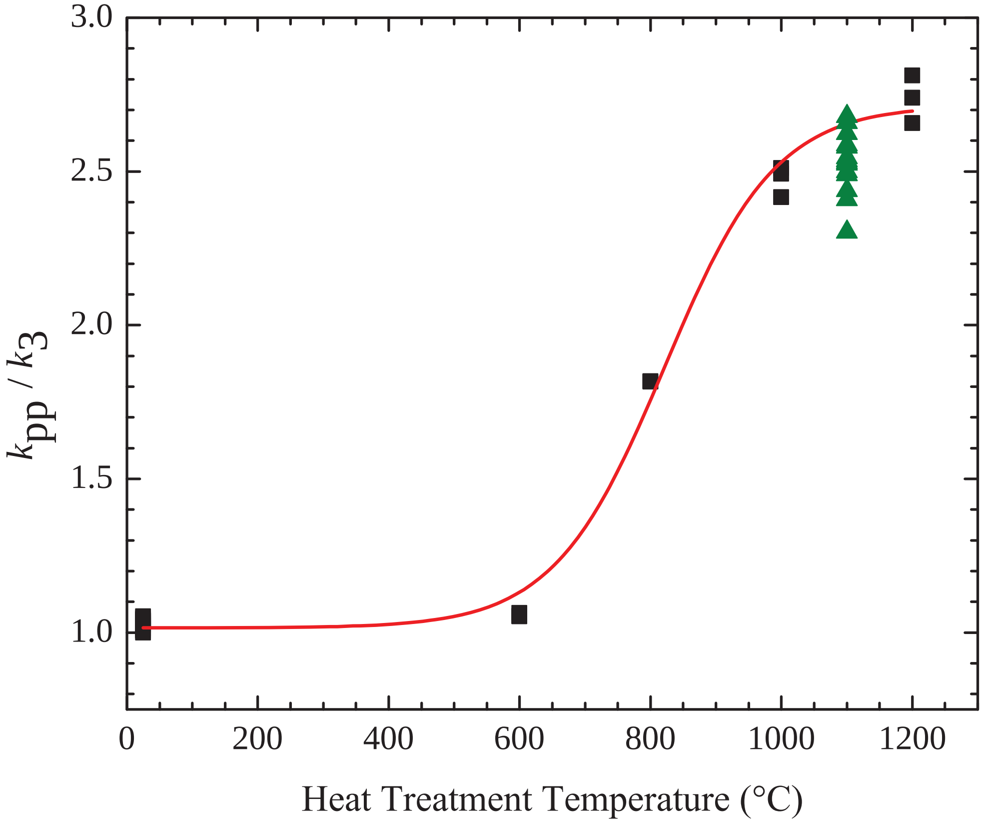

Figure 4.15: Thermal conductivity ratios k_{pp}/k_3 for the specimens in Set 2 (squares) in their as-received condition, and after 2 h heat treatments. The solid line represents a sigmoidal curve fit to the k_{pp}/k_3 data for the specimens in Set 2 (squares). The k_{pp}/k_3 for specimens in Set 1 heat-treated at 1100 ℃ for 4 h (triangles) is also plotted.

where W_{gd} is the thermal resistivity of phonons due to dislocations. This resistance can be separated from the phonon dominated thermal conductivity k_{g} as [26]

$$k_{\mathrm{g}} = \left[k_{\mathrm{gb}}^{-1} + W_{\mathrm{gd}}\right]^{-1}, \tag{4.2}$$

where k_{gb} is the crystal boundary limited phonon conductivity. For analyzing specimens presented here, the thermal conductivity at the phonon peak k_{pp} is used for the phonon conductivity k_{g}. The Casimir [39] relation for k limited by crystal boundaries, defined in equation (2.11), is used for k_{gb}. For convenience, equation (2.11) is rearranged and presented here as

$$k_{\mathrm{gb}}^{\mathrm{c}} = 2.31 \times 10^3\, R\, \frac{2\,(v_l/v_t)^2 + 1}{\left[2\,(v_l/v_t)^3 + 1\right]^{2/3}} \left[\frac{C_v}{T^3}\right]^{2/3} T^3, \tag{4.3}$$

where R is the radius for a circular cylindrical specimen, C_v the specific heat per unit volume, and v_l and v_t are the longitudinal and transverse velocities of sound in the material, respectively. For a specimen with square cross section d^2, R in the above equation would be replaced [39] by $R = 0.564 * d$. For specimens with a rectangular cross sectional area A_{cs}, like the ones presented here, R would be replaced by $R = 0.564\sqrt{A_{\mathrm{cs}}}$.

The dislocation densities for specimens 9 – 12 obtained using equation (4.1) are illustrated as a function of the heat treatment temperature in Figure 4.16. For perspective and comparison, N_{d} is added to the thermal conductivities of specimens 9 – 12 presented in Figure 4.15. This analysis supports the role of reducing dislocations in the enhancement of k_{pp}.

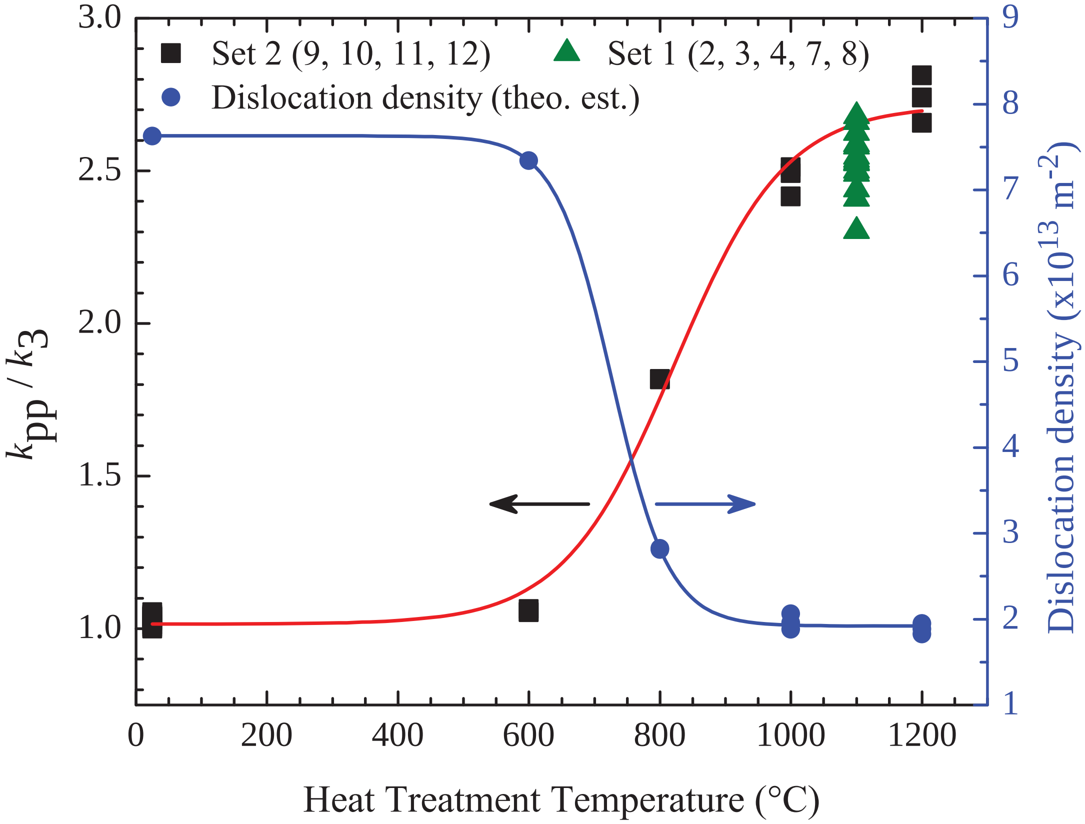

Figure 4.16: The estimated dislocation densities for specimens 9 – 12 using equation (4.1). Note that the dislocation density N_d is plotted over Figure 4.15, for comparison with the thermal conductivities of the specimens.

4.2.2.2 Orientation imaging microscopy

The local average misorientation (LAM) for specimens 9 – 12, generated from orientation gradient maps, in their as-received conditions and after the 2 h heating are illustrated in Figure 4.17. Specimen 9 in its as-received condition has the smallest and widest LAM, indicating greater crystal imperfections in the specimen. The remaining three specimens have similar LAM curves in their as-received condition, suggesting similar dislocation content. After the 2 h heating, specimens 9, 10, and 12, heat treated at 600 ℃, 800 ℃, and 1000 ℃, respectively, similar LAM curves, with peaks at smaller misorientation angle with narrower full width at half maximum than that of the as-received state. Specimen 12, heated at 1200 ℃, displays the most LAM peak shift to the left, indicating greater recovery of dislocations in the material. The LAMs for these four specimens, however, do not directly correlate with the trends of the recovery of the corresponding phonon peaks. This discrepancy may stem from the thermal conductivity being a bulk measurement, while the LAMs are surface measurements, and therefore not indicative of the bulk.

4.2.2.3 X-Ray diffraction

High-energy X-Ray diffraction was performed on all four specimens in Set 2 after the 2 h heat treatment. Each of the specimens was examined at 27 locations, with the specimen being rotated 45° (±22.5°) at each location. The diffracted X-ray peak data was recorded in 60 frames per 45° sweep, *i.e.*, 0.75° per frame, thereby generating 1620 frames per specimen.

The diffracted peaks corresponding to the planes of interest were identified by comparing the theoretical d-spacing for the respective planes with that estimated from the radius of the peaks on the detector with respect to the X-ray beam. The planes to be used to estimate imperfection density of the specimens were chosen based on the stereographic projections of

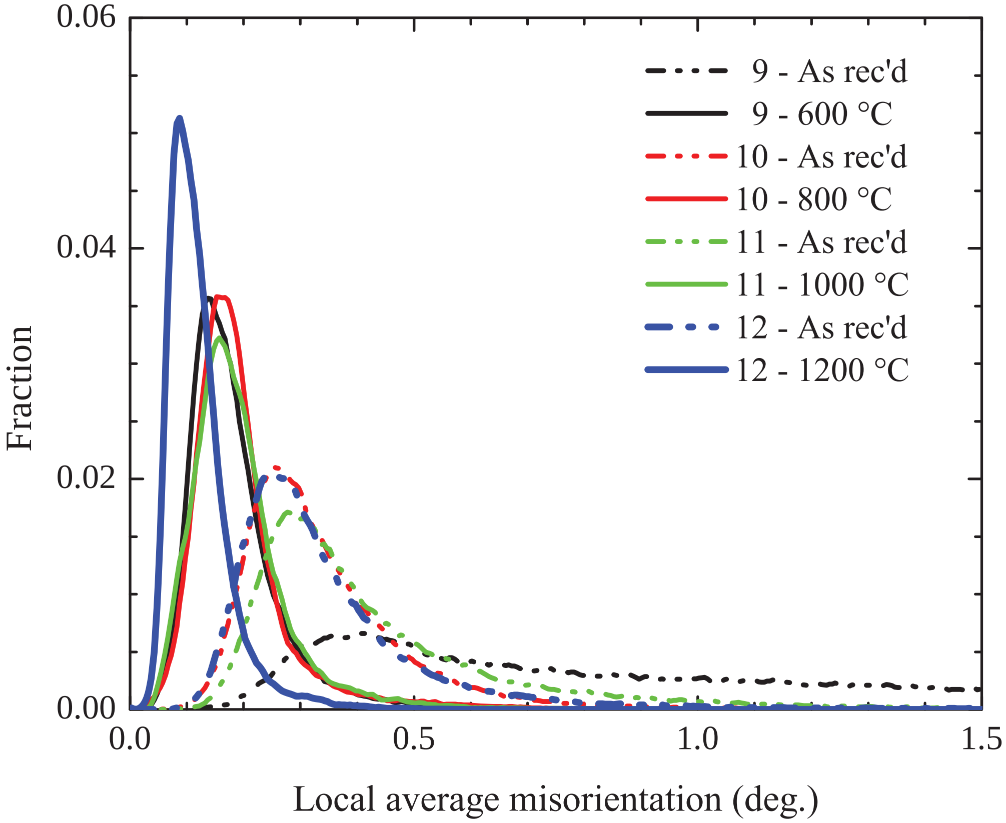

Figure 4.17: The local average misorientation for the single crystal specimens 9 – 12, in their as-received conditions and after the 2 h heating at temperatures between 600 ℃ and 1200 ℃.

these planes.

For specimens 9 – 12, the stereographic projections are similar due to the small variation in Euler angles, as illustrated in Figures 4.18 – 4.21, respectively. The shaded grey region at the center of the stereographic projection plot indicates crystallographic space that was not exposed to the X-rays due to the ±22.5° rotation of the specimen. Hence, only planes that have plane normal directions in the white space outside of the grey area would be diffracted onto the detector. For the four specimens illustrated in Figures 4.18 – 4.21, only two of the four {111} planes with <111> plane normal directions were in the white, detectable region. Hence, a {222} peak analysis could be used to qualitatively estimate dislocation and imperfection contents of the specimens.

Since specimens 9 – 12 are single crystals, the diffracted peaks for all 27 locations, *i.e.*, all 1620 frames, can simultaneously be used to compare the imperfection densities. The spread of the diffracted {222} peaks across the 27 locations for each of the four specimens are illustrated in Figures 4.22 – 4.25. The x- and y-distances are in the figure are with respect to the location of the beam on the detector. The four peak clusters are the locations of the X-rays diffracted by the two {111} planes identified in Figure 4.18. Each individual cluster is a group of {222} peaks from several of the 1620 frames recorded per specimen, and the actual number of frames from which {222} peaks are detected for each cluster is listed towards the center of the figure. The normalized standard deviations of the locations of these peaks are plotted against the temperature of heat treatment in Figure 4.26. The normalized standard deviation is defined as

$$\text{norm. } \sigma = \sqrt{\sigma_x^2 + \sigma_y^2}, \tag{4.4}$$

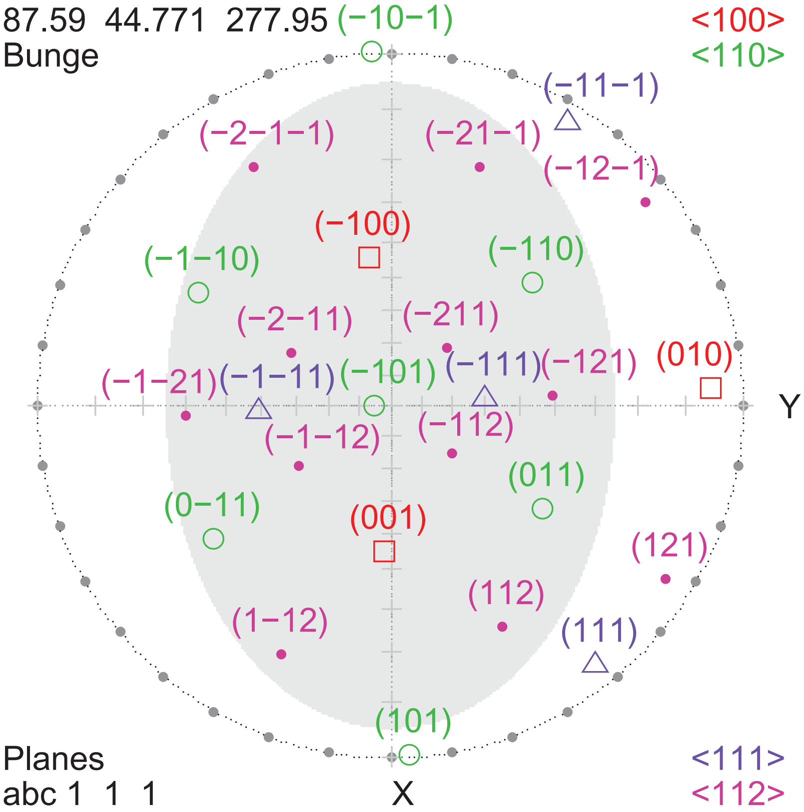

Figure 4.18: Stereographic projection for specimen 9 after the 600 ℃ for 2 h heat treatment, using Euler orientations obtained by EBSD. The stereographic projection was used to identify planes from which X-ray diffraction peaks could be used to estimate the imperfection density of the specimen. The grey shaded region represents crystallographic space which was not visible to the X-rays due to the 45°sweep of the specimens. The stereographic projection was generated using a MATLAB® algorithm developed by Bieler [59].

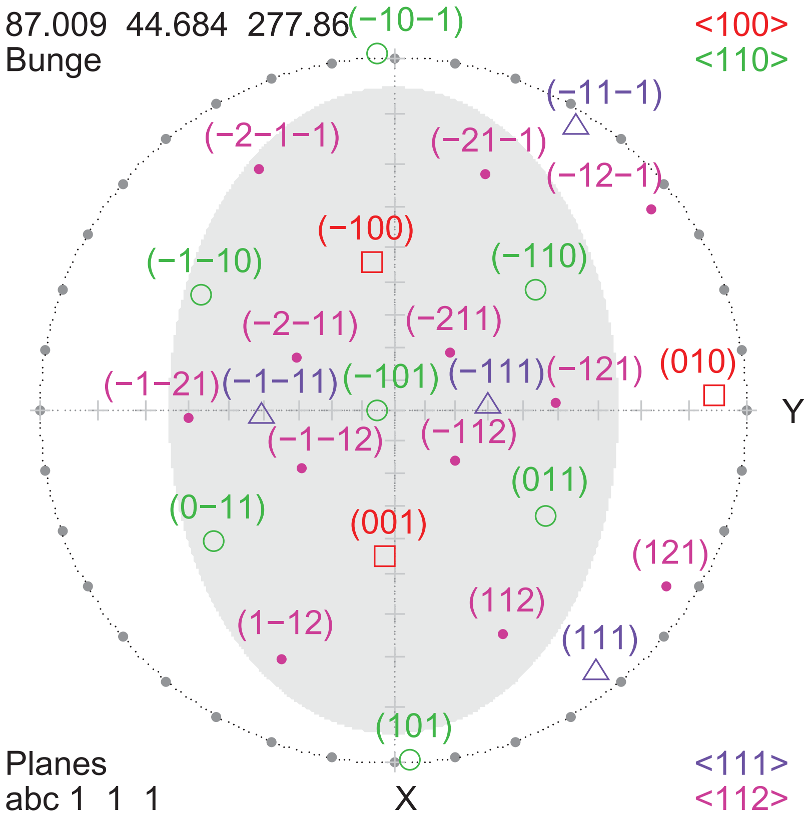

Figure 4.19: Stereographic projection for specimen 10 after the 800 ℃ for 2 h heat treatment, using Euler orientations obtained by EBSD. The stereographic projection was used to identify planes from which X-ray diffraction peaks could be used to estimate the imperfection density of the specimen. The grey shaded region represents crystallographic space which was not visible to the X-rays due to the 45°sweep of the specimens. The stereographic projection was generated using a MATLAB® algorithm developed by Bieler [59].

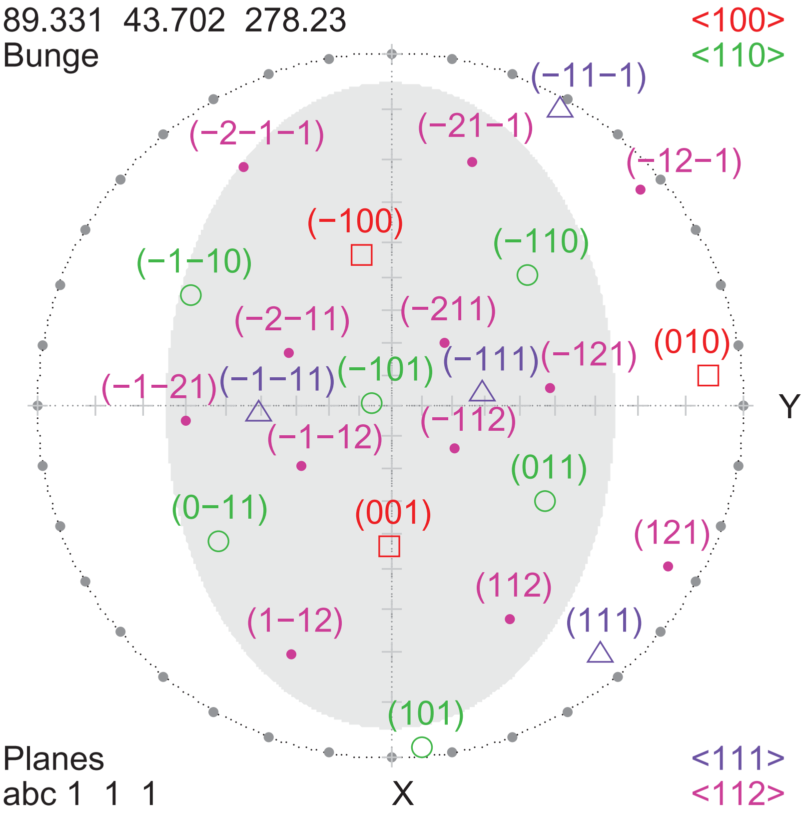

Figure 4.20: Stereographic projection for specimen 11 after the 1000 ℃ for 2 h heat treatment, using Euler orientations obtained by EBSD. The stereographic projection was used to identify planes from which X-ray diffraction peaks could be used to estimate the imperfection density of the specimen. The grey shaded region represents crystallographic space which was not visible to the X-rays due to the 45°sweep of the specimens. The stereographic projection was generated using a MATLAB® algorithm developed by Bieler [59].

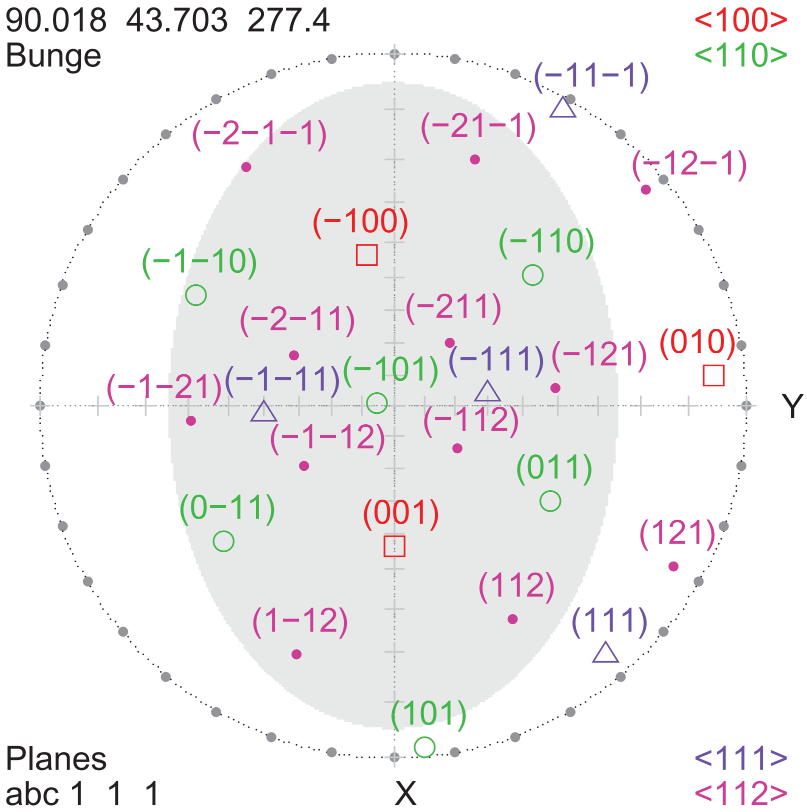

Figure 4.21: Stereographic projection for specimen 12 after the 1200 ℃ for 2 h heat treatment, using Euler orientations obtained by EBSD. The stereographic projection was used to identify planes from which X-ray diffraction peaks could be used to estimate the imperfection density of the specimen. The grey shaded region represents crystallographic space which was not visible to the X-rays due to the 45°sweep of the specimens. The stereographic projection was generated using a MATLAB® algorithm developed by Bieler [59].

where σ_x and σ_y are the standard deviations of a peak in the x- and y-directions, respectively. The primary axes, x- and y-, are defined as illustrated in Figure 3.6. The decreasing dislocation density with increasing increasing heat treatment temperature is clearly illustrated by the decreasing normalized standard deviation.

The average of the full width at half maximum (FWHM) in x- and y-directions are plotted against each other for the four specimens in Figure 4.27. The 1000 ℃ heat treated specimen 11 has the smallest FWHM amongst the four specimens, followed by specimens 12 (green symbols), 10 (red symbols), and 9 (black symbols), heat treated at 1200 ℃, 800 ℃, and 600 ℃, respectively. A smaller FWHM in both the x- and y-directions is indicative of a sharper diffraction peak, implying lesser crystal imperfections in the material.

4.3 Young's modulus and the phonon peak

The Young's modulus E is estimated for specimens 1 – 12 using equation (3.4) and the Euler angles for the specimens. A MATLAB® algorithm developed by Bieler [59] is used to estimate E for specimens 1 – 12 after their hottest temperature heat treatments. The algorithm calculates E using equation (3.4) and a unit vector parallel to the heat flow direction generated from Euler angles. An inverse pole figure displaying the crystal orientations of specimens 1 – 12 with a graded background representing the variation in E for Nb is illustrated in Figure 4.28. The red symbols represent the crystal orientation of grain 1, while the green symbols represent grain 2 in the bicrystal specimens. For the single crystal specimens 9 – 12, a red symbol is used. The shades of grey, from light to dark, indicate the variation in E of Nb from 83.24 GPa to 145.48 GPa, respectively. For the specimens heat treated at $T_{\mathrm{h}} \geq 1000$ ℃, the normalized phonon peak (k_{pp}/k_3) is compared with the

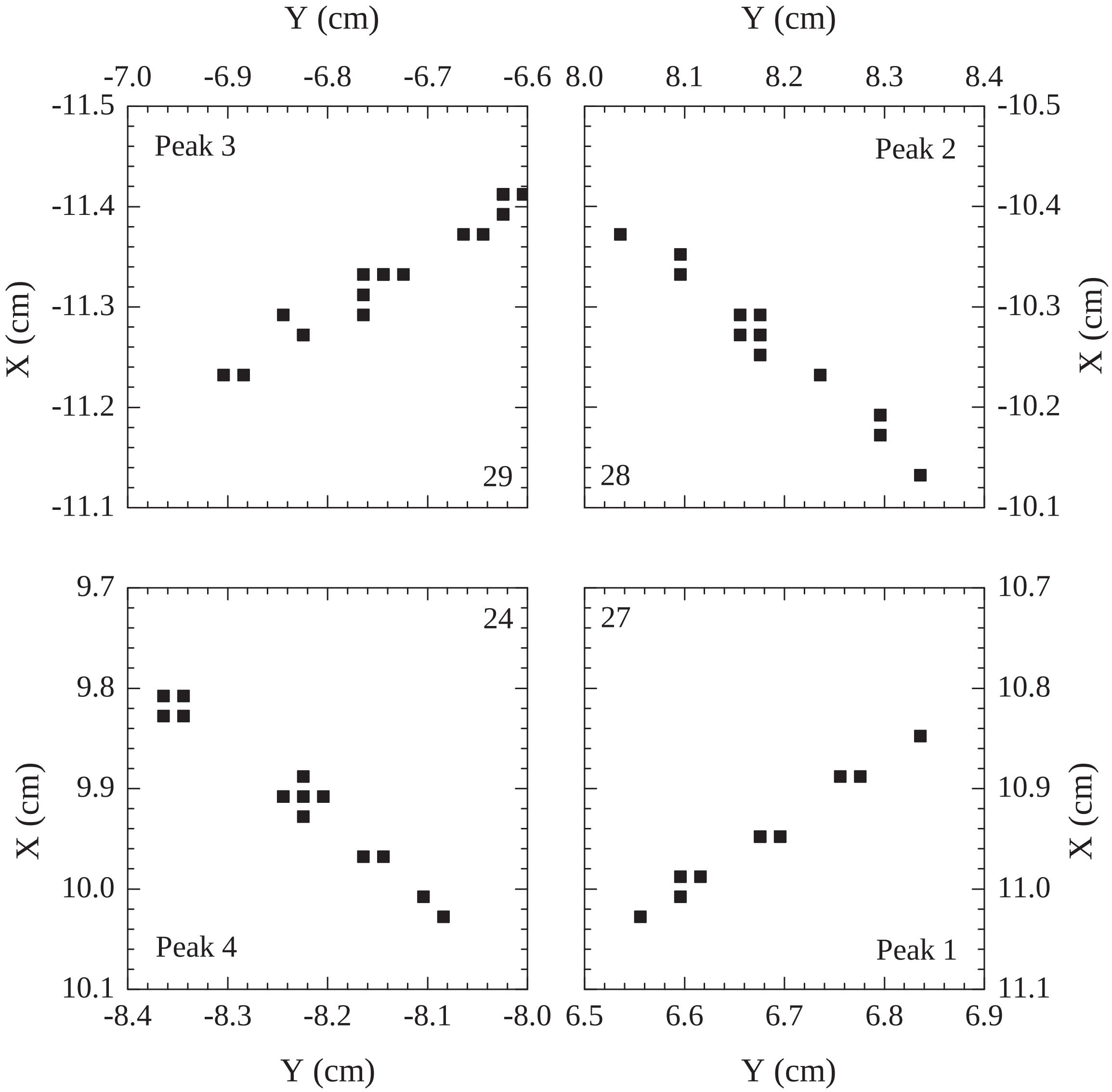

Figure 4.22: Detected peak maximum locations for peaks from {222} planes for specimen 9 after the 600 ℃ for 2 h heat treatment. The x- and y-distances are with respect to the location of the beam on the detector. The four peak clusters are the locations of the X-rays diffracted by the two {111} planes identified in Figure 4.18. Each individual cluster is a group of {222} peaks from several of the 1620 frames recorded per specimen. The number listed in each cluster, towards the center of the figure, is the actual number of frames from which {222} peaks are detected. The spread of the peaks within each cluster represents imperfection density in the crystal.

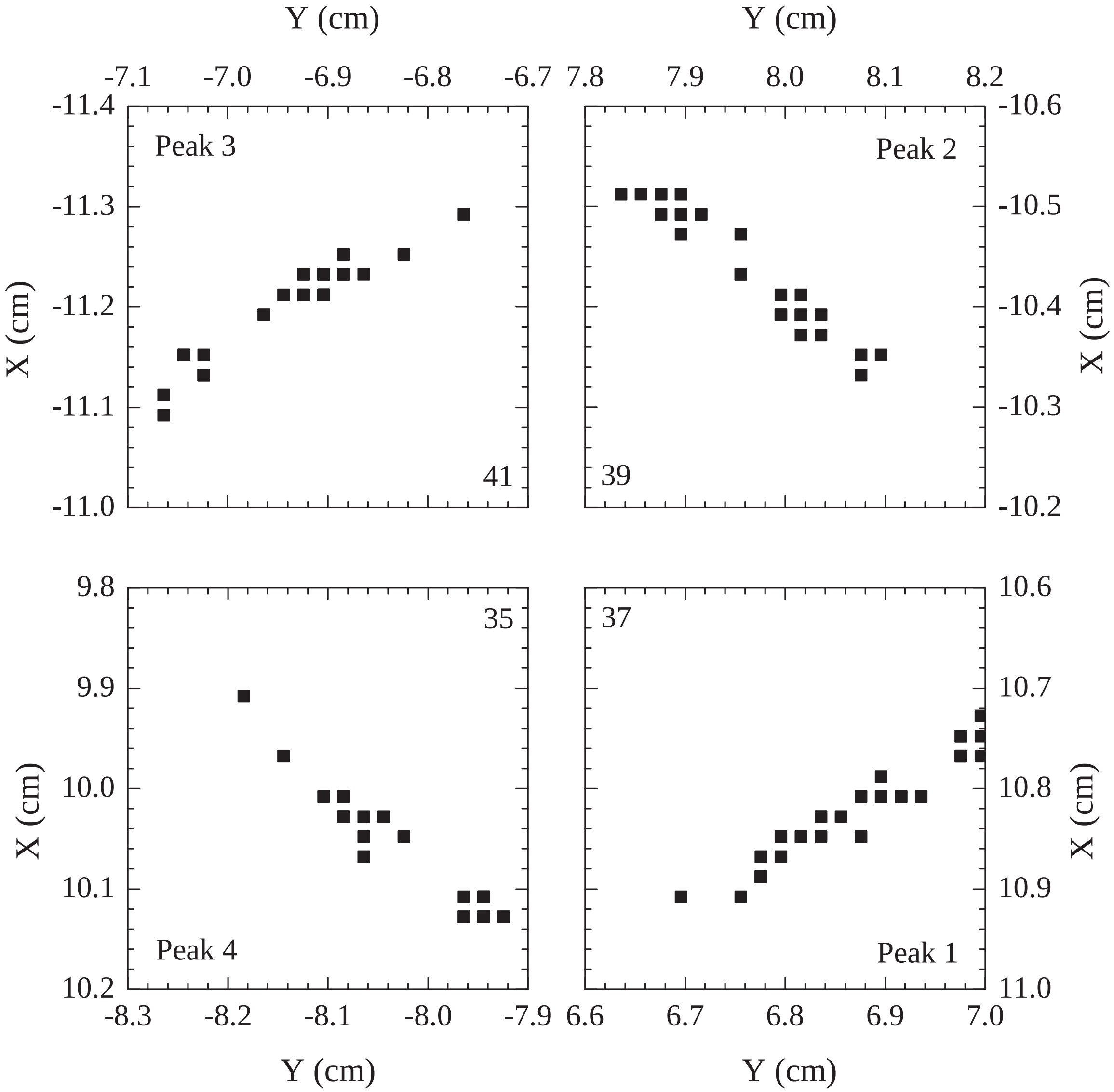

Figure 4.23: Detected peak maximum locations for peaks from {222} planes for specimen 10 after the 800 ℃ for 2 h heat treatment. The x- and y-distances are with respect to the location of the beam on the detector. The four peak clusters are the locations of the X-rays diffracted by the two {111} planes identified in Figure 4.19. Each individual cluster is a group of {222} peaks from several of the 1620 frames recorded per specimen. The number listed in each cluster, towards the center of the figure, is the actual number of frames from which {222} peaks are detected. The spread of the peaks within each cluster represents imperfection density in the crystal.

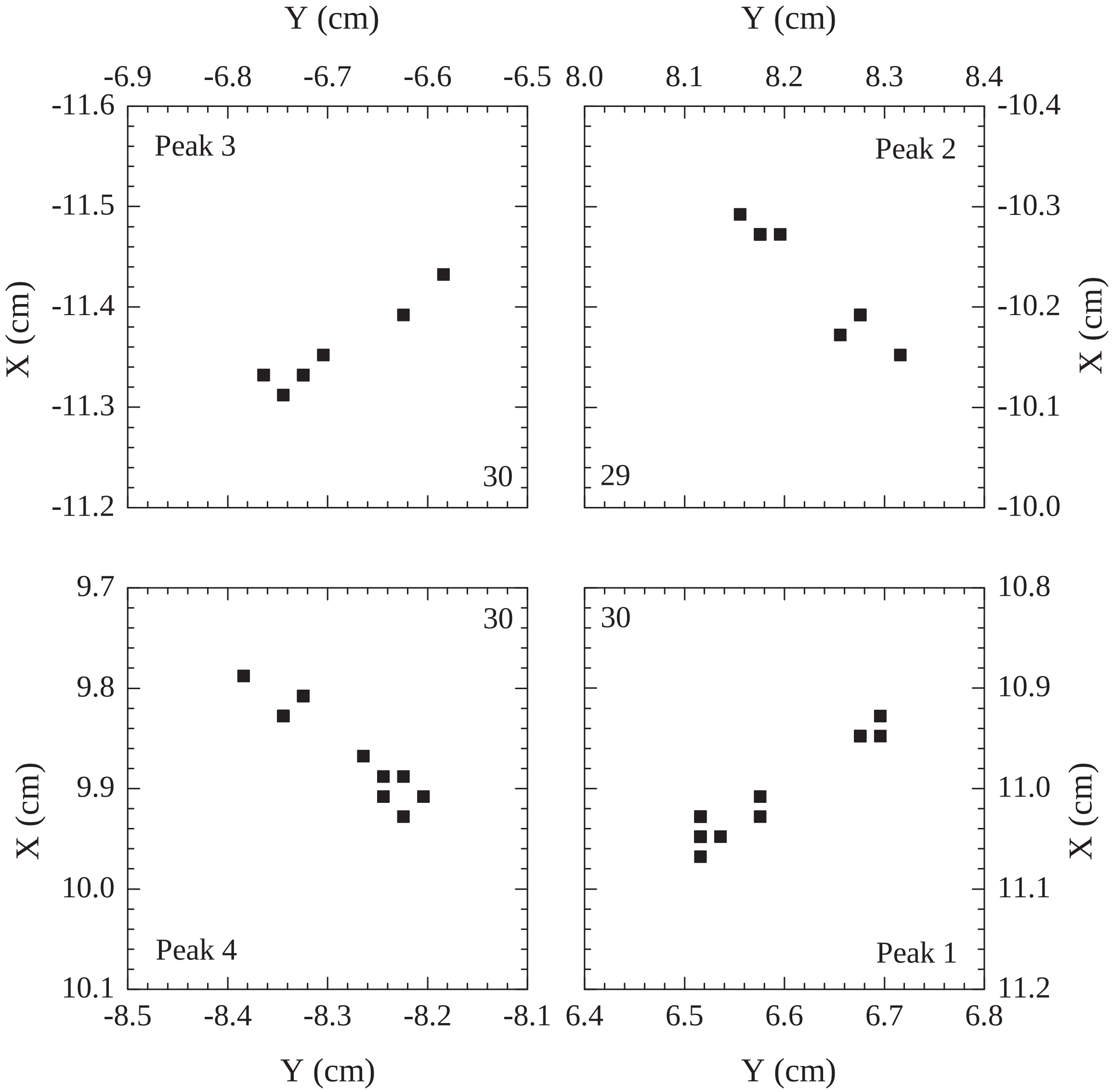

Figure 4.24: Detected peak maximum locations for peaks from {222} planes for specimen 11 after the 1000 ℃ for 2 h heat treatment. The x- and y-distances are with respect to the location of the beam on the detector. The four peak clusters are the locations of the X-rays diffracted by the two {111} planes identified in Figure 4.20. Each individual cluster is a group of {222} peaks from several of the 1620 frames recorded per specimen. The number listed in each cluster, towards the center of the figure, is the actual number of frames from which {222} peaks are detected. The spread of the peaks within each cluster represents imperfection density in the crystal.

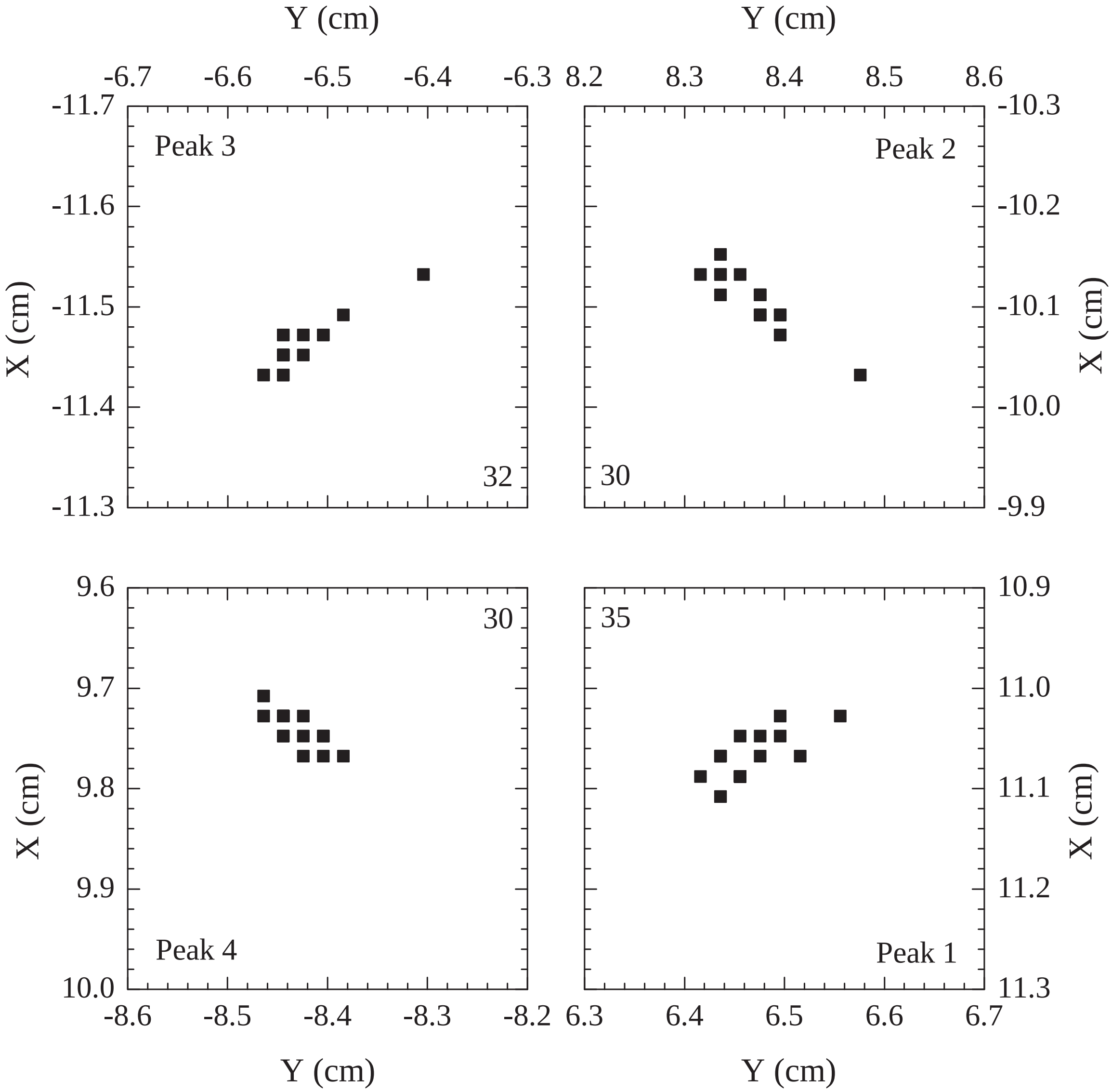

Figure 4.25: Detected peak maximum locations for peaks from {222} planes for specimen 12 after the 1200 ℃ for 2 h heat treatment. The x- and y-distances are with respect to the location of the beam on the detector. The four peak clusters are the locations of the X-rays diffracted by the two {111} planes identified in Figure 4.21. Each individual cluster is a group of {222} peaks from several of the 1620 frames recorded per specimen. The number listed in each cluster, towards the center of the figure, is the actual number of frames from which {222} peaks are detected. The spread of the peaks within each cluster represents imperfection density in the crystal.

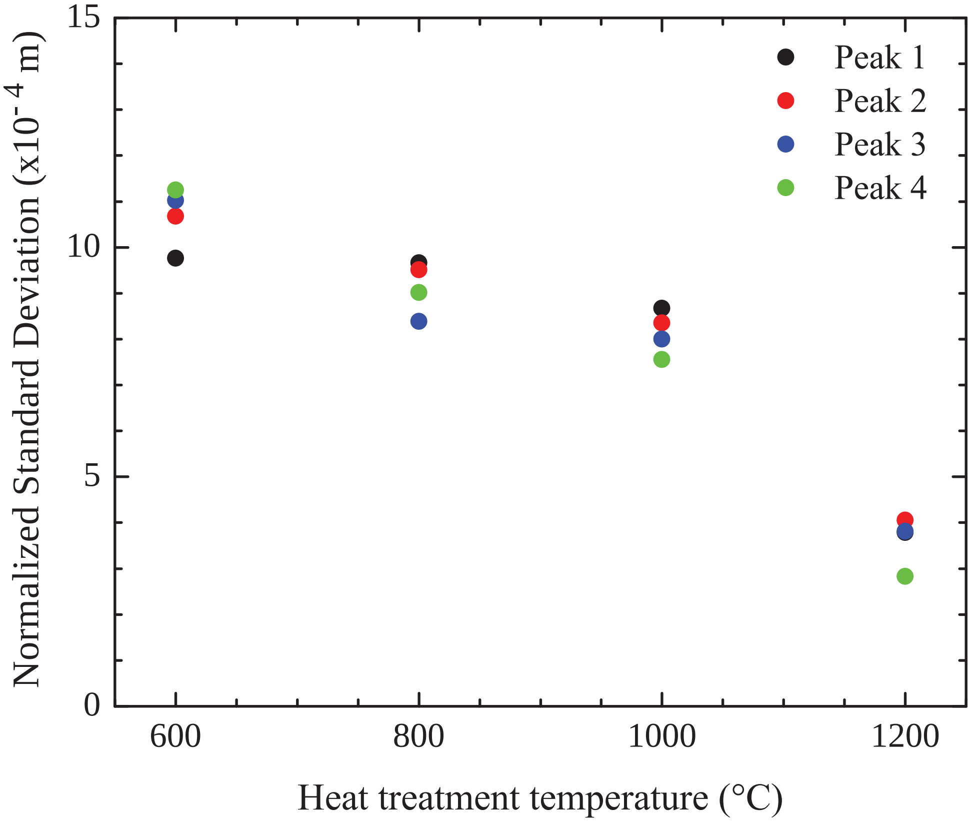

Figure 4.26: The normalized standard deviation of the locations of the diffracted X-ray peak maximums, as defined in equation (4.4). Smaller values of normalized standard deviation imply reduced dislocation contents. Specimen 12, heat treated at 1200 ℃ for 2 h, has the smallest deviation values amongst the four specimens, indicating greatest recovery of dislocations.

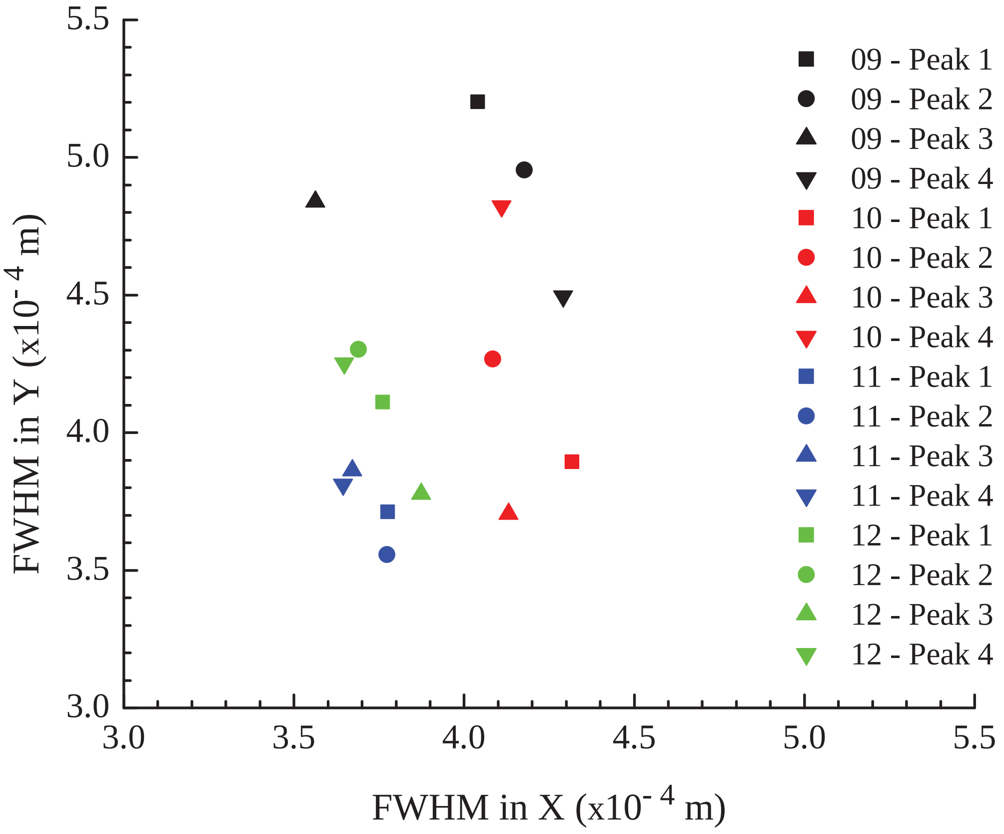

Figure 4.27: The average of full width at half maximum (FWHM) of the four {222} peak clusters for specimens 9 – 12, when measured along the X and Y directions. A smaller FWHM in both the x- and y-directions would imply a sharper peak.

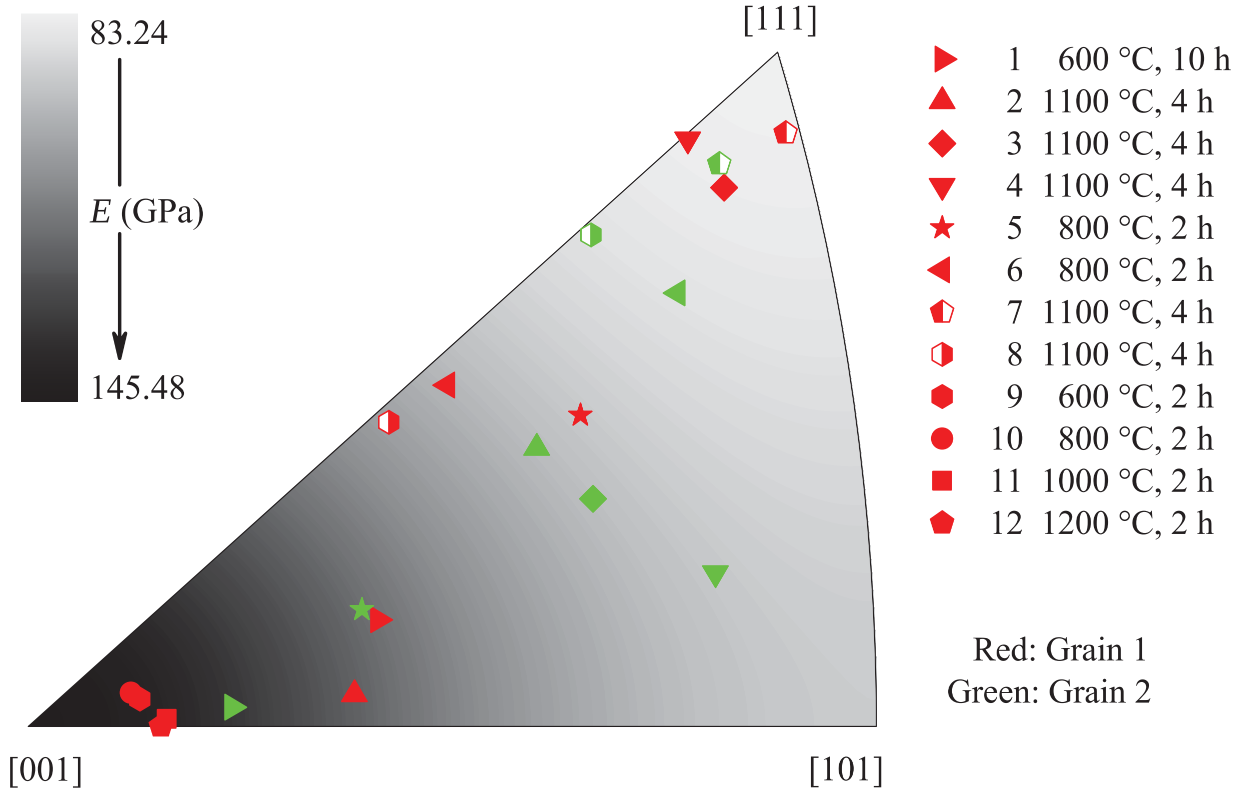

Figure 4.28: An inverse pole figure displaying the crystal orientations of grains 1 (red) and 2 (green) of specimens 1 – 8, and of the single crystal specimens 9 – 12 (red), after their hottest temperature heat treatments. A shaded grey background, from light to dark grey, is used to represent the variation in E of Nb from 83.2 GPa to 145.5 GPa, respectively.

Young's modulus in Figure 4.29. The solid line represents a least squares fit to the data, and reveals a mild correlation between k_{pp}/k_3 and E.

4.4 Parameters from thermal conductivity model

Of the five β_is listed in equation (3.9), four ($i = 1, 3, 4, 5$) are estimated while reducing the T and q'' data from the measurements of k. The estimated β_1s (scattering of normally

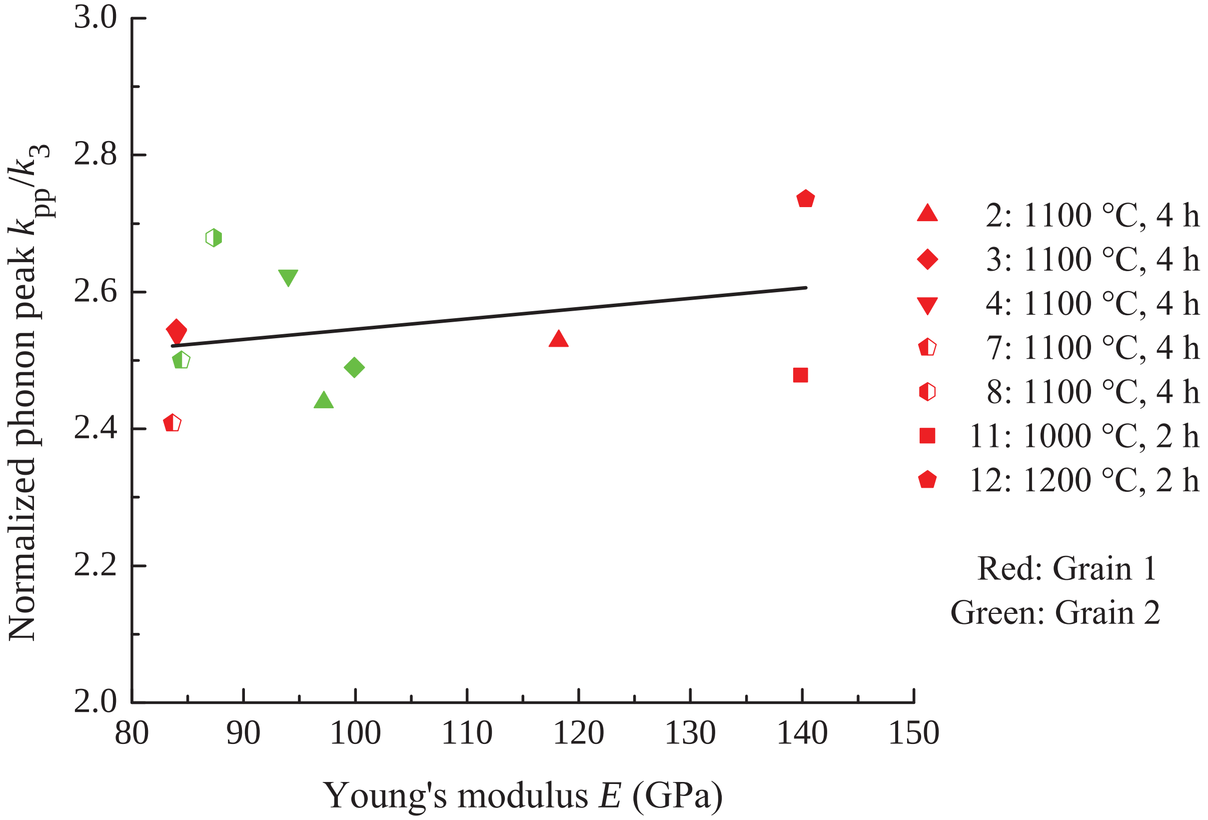

Figure 4.29: A comparison of the normalized phonon peak (k_{pp}/k_3) with E as estimated using equation (3.4). Only specimens that are heat treated at $T_{\mathrm{h}} \geq 1000$ ℃ are used for this purpose. The solid line represents a least squares fit to the data, and reveals a mild correlation between k_{pp}/k_3 and E.

conducting electrons by impurities) for the twelve specimens, in their as-received condition and after heat treatments, are compared with RRR in Figure 4.30. The inverse proportionality between β_1 and RRR is evident, and is as expected from the definition of β_1 (= $\rho_{295}/(L\ \mathrm{RRR})^{-1}$).

The estimated β_3 (scattering of phonons by normal conducting electrons) for the twelve specimens, in their as-received condition and after heat treatments, are compared with the heat treatment temperature and shown in Figure 4.31. The dashed line represents the theoretical value for β_3. The average of β_3 for each T_h begins to center around the theoretical value with increased heat treatment temperature.

The estimated β_4 (scattering of phonons by lattice defects and boundaries) for the twelve heat-treated specimens, in their as-received condition and after heat treatments, are compared with the heat treatment temperature and are illustrated in Figure 4.32. A strong dependence of β_4 on heat treatment temperature is noted, with all of the as-received specimens displaying greater values than any of the heat treated values.

The estimated β_5 (condensation of electrons into Cooper pairs) for the twelve specimens, in their as-received condition and after heat treatments, are compared with the heat treatment temperature and shown in Figure 4.33. Note that the relative range of the ordinate is much smaller than those of other β_is.

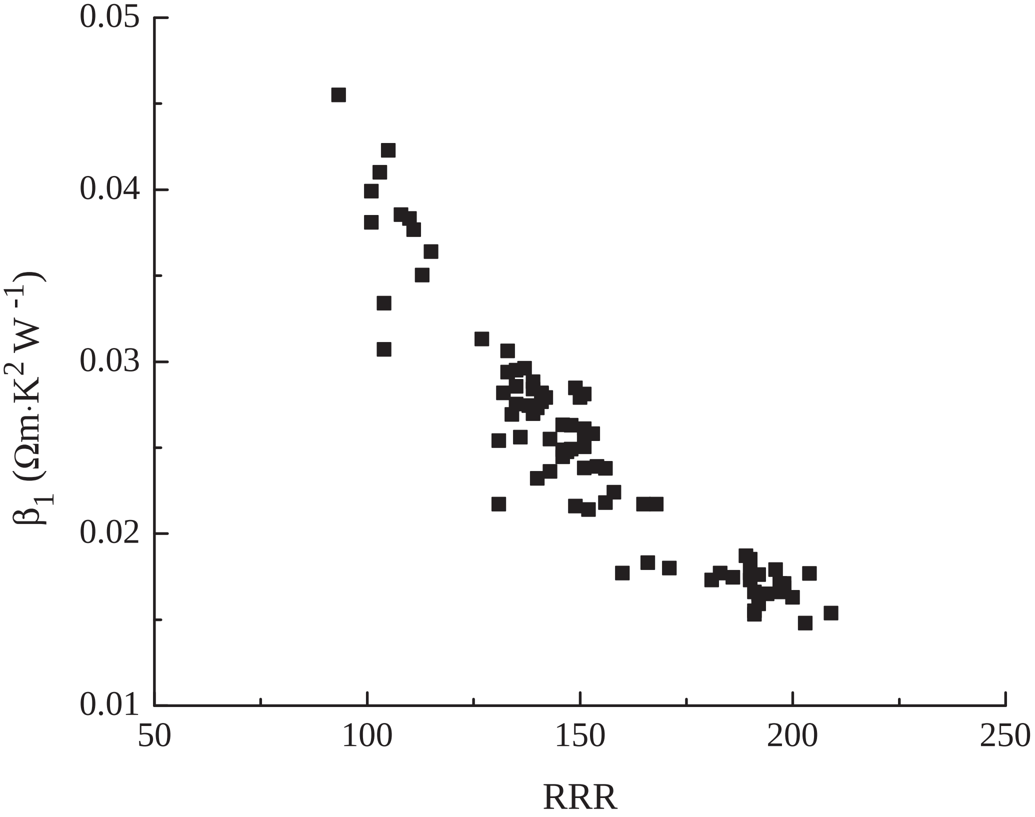

Figure 4.30: Comparison of β_1 (scattering of normally conducting electrons by impurities) with RRR for the twelve specimens, in their as-received condition and after heat treatments. The inverse proportionality would be expected from the definition of β_1 $(= \rho_{295}/(L\,\mathrm{RRR})^{-1})$.

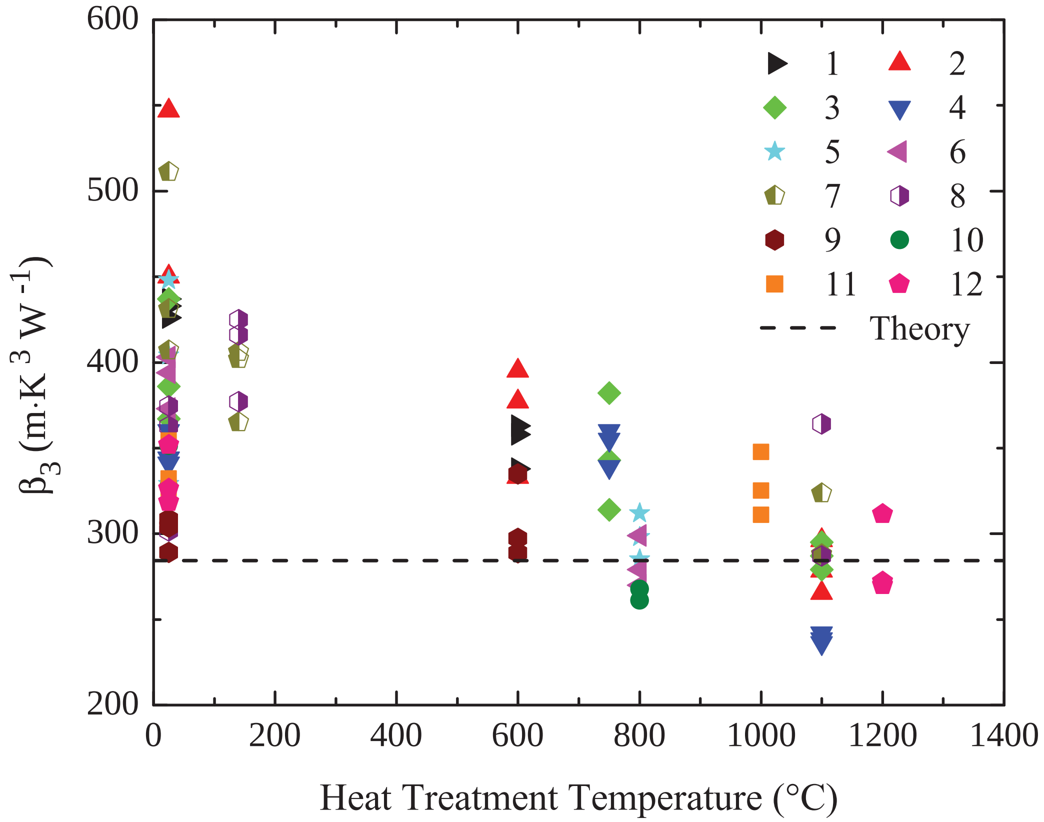

Figure 4.31: Comparison of β_3 (scattering of phonons by normal conducting electrons) with the heat treatment temperature for the twelve specimens. The dashed line represents the theoretical value for β_3. In these specimens, increased heat treatment temperature brings the measured β_3 into agreement with the theoretical value.

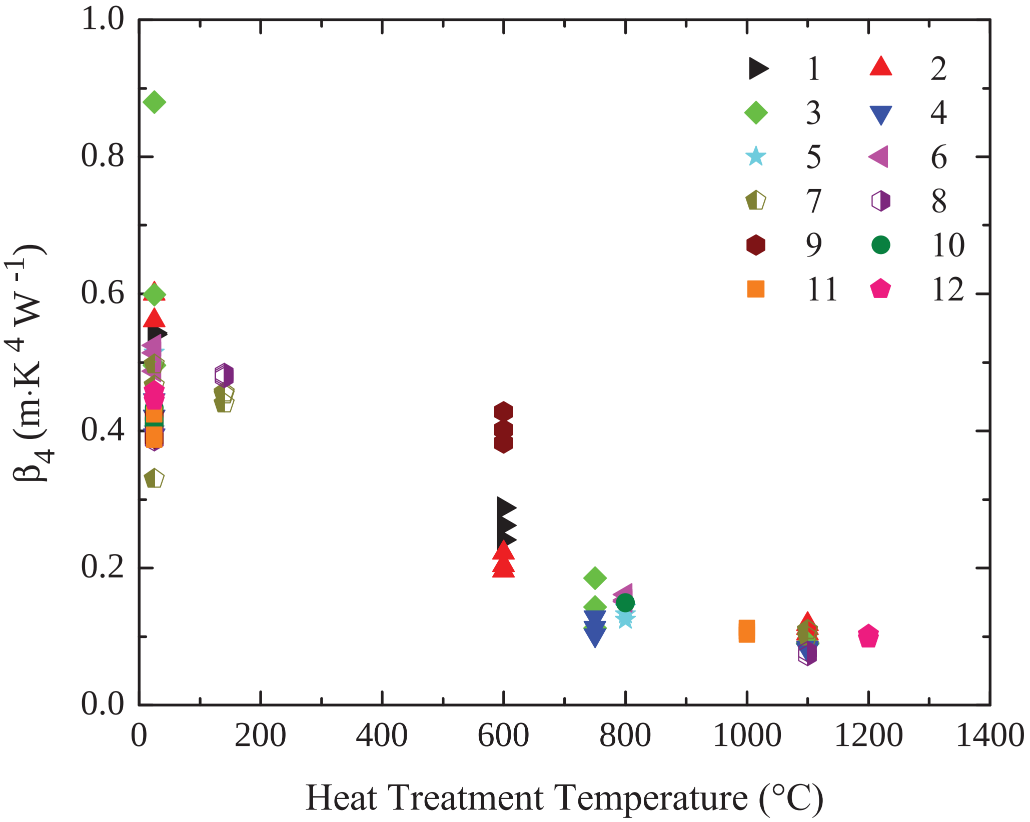

Figure 4.32: Comparison of β_4 (scattering of phonons by lattice defects and boundaries) with the heat treatment temperature for the twelve specimens. As-received specimens display greater β_4 values than those post-heat treatment. Wide variations in the as-received β_4 values may indicate a broad range of process histories. Note again that the 750 ℃ heat treatment was with Ti getter and had a temperature ramp rate of 5 ℃ per minute, whereas at 800 ℃ there was no getter and the temperature ramp rate was 10 ℃ per minute. Note also that the 600 ℃ heat treatment for specimens 1 and 2 was for 6 h, while that for specimen 9 was for 2 h.

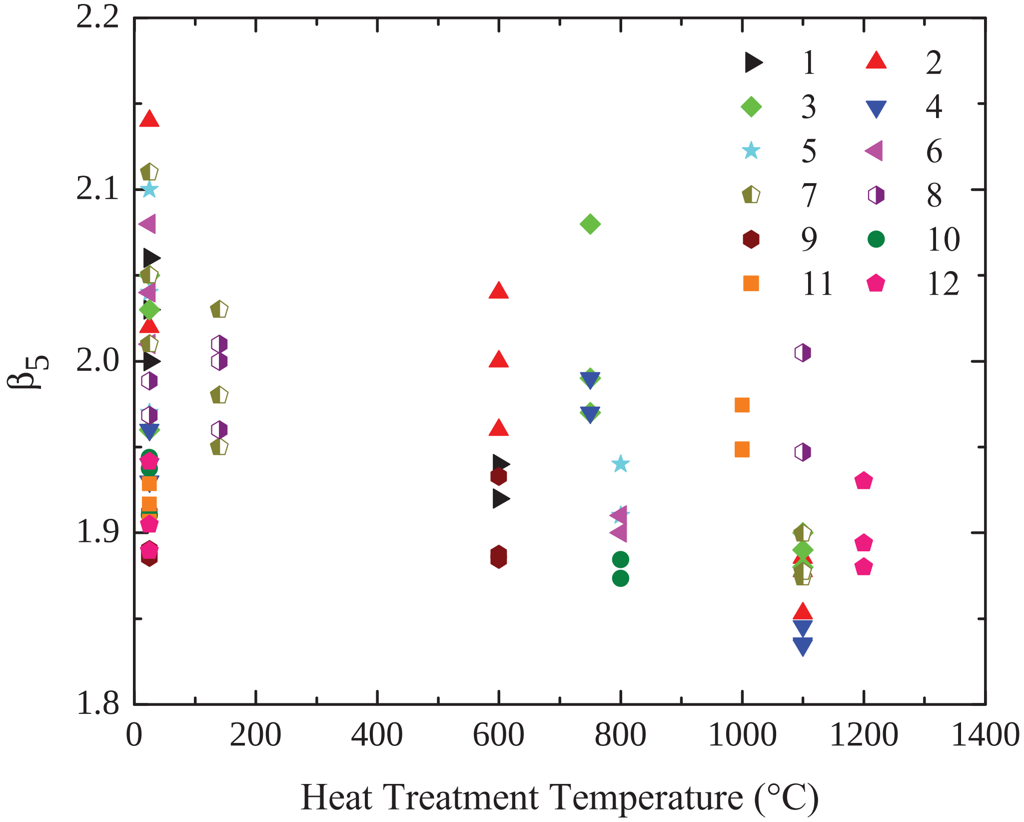

Figure 4.33: Comparison of β_5 (condensation of electrons into Cooper pairs) with the heat treatment temperature. Note that the relative range of the ordinate is smaller than those for other β_is, indicating that the scatter is smaller than it appears.

4.5 Discussion

The as-received specimens in Set 1 display a variety of k for $T > 3$ K, indicating a variation in RRR. The k for $T > 3$ K for the as-received specimens in Set 2 have similar magnitudes, indicating similar RRR, as expected for specimens from the same grain of the same ingot disc. For $T \lesssim 3$ K, however, the as-received specimens in both Sets 1 and 2 display little or no phonon peak irrespective of their crystal orientations, suggesting the presence of dislocations from residual stresses during cooling of the ingot. Except specimen 3, illustrated in Figure 4.3, grains 1 and 2 of the as-received specimens in sets 1 and 2 have similar k curves, suggesting similar RRR and dislocation contents. Although specimens 3 and 4 were cut from the same ingot disc, they have different as-received k. While the two grains in specimen 4 (Figure 4.4) display similar k for $T > 3$ K, indicating similar RRR, the k for $T > 3$ K of grain 1 in specimen 3 is 20% smaller than that of grain 2 in specimen 3 and those in specimen 4. This suggests that there are variations of RRR within a grain in the same ingot disc. After the 750 ℃ for 2 h heat treatment, however, k at 4.2 K for grain 1 of specimen 3 and across the GB increases to that of grain 2, indicating removal of impurities within the grain. Since grain 2 had no change in k at 4.2 K, the change in k of grain 1 can be attributed to the degassing of gaseous impurities, such as hydrogen.

Although several benefits have been observed for the surface layer of Nb after heat treatment at 100 ℃ – 150 ℃ for 48 h [23], no benefit to the thermal conductivity was observed for specimens 7 and 8 after a 140 ℃ for 48 h heat treatment. This confirms that the benefits of the $100 \leq T_{\mathrm{h}} \leq 150$ ℃ heat treatments are limited to the surface of Nb, and has no effect on the crystallography of the bulk.

An 800 ℃ heat treatment for 2 h in the absence of a titanium getter or a 750 ℃ for

2 h heat treatment with a titanium getter resulted in an average 140% increase in k at the phonon peak. The similarity in k_{pp}/k_2 values for 750 ℃ and 800 ℃ heat treatments, tabulated in Table 4.2, may be due to the small difference in the heat treating temperatures, combined with the presence of titanium getter at 750 ℃, and the slower temperature ramp rate of 5 ℃ per minute for the 750 ℃ heat treatment in contrast with the 10 ℃ per minute ramp rate for the 800 ℃ heat treatment. Note that in the ratio k_{pp}/k_2, k_{pp} is k at the phonon peak after heat treatment, while k_2 is k at 2 K in the as-received condition. The 600 ℃ heat treatment for 6 h in the absence of a titanium getter resulted in an average 100% increase in k at the phonon peak. The 17% difference in the magnitudes of the phonon peaks for specimens 1 and 2 after the 600 ℃ heat treatment may be due to the difference in their cross sectional areas. Despite their shortest dimension being similar, their second dimension in the cross section differs by 60%, which may affect the magnitude of scattering of some phonon modes.

The anomalous $k_{\mathrm{pp}}/k_2 = 4.9$ for specimen 3 across the GB is not well understood. Although, greater recovery of dislocations due to the grain boundary acting as a sink for dislocations might explain this result. Similar trends, albeit lower in magnitude than specimen 3, are seen across the grain boundary for all the specimens in Set 1 after the 600 ℃ – 800 ℃ heat treatments, except specimen 6. Specimen 2 displays greater k_{pp} across the GB even after the 1100 ℃ for 4 h heat treatment, while specimens 3, 4, 7, and 8, that were also heat-treated at $T_{\mathrm{h}} = 1100$ ℃, do not show such differences and have overlapping k curves for both the grains and across the grain boundary.

When compared with the RRR of the specimens after the 1100 ℃ heat treatment, the k_{pp} for specimens in Set 1 illustrated in Figure 4.9 show a monotonic dependence on the RRR. This implies that the dominant phonon scattering mechanism is due to impurities, and no longer due to dislocations formed during the differential cooling of the ingot. This result is in good agreement with the findings of Wasserbäch [45] on the dependence of conductivity on the purity of superconducting tantalum ($80 \leq \mathrm{RRR} \leq 3000$) and niobium (RRR=300).

Examining the k_{pp}/k_3 ratio in Table 4.2 for the 1100 ℃ heat-treated specimens, thereby suppressing the effect of RRR (and k_{e}) on k_{pp}, it is evident that despite the differences in the magnitudes of k_{pp} the phonon contribution to k is almost a constant. The same ratios for specimens in Set 2, illustrated in Figure 4.15, also indicate the presence of a constant phonon contribution to k for $T_{\mathrm{h}} > 1000$ ℃. The coupling of k in the phonon dominant regime ($T \leq 3$ K) with that in the electron dominant regime ($T \geq 3$ K) implies that the overall thermal performance of cavities will be greatest for Nb with the greatest RRR.

The ratio k_{pp}/k_3 for the single crystal specimens in Set 2, with the same crystal orientations, displays a sigmoidal dependence on heat treatment temperature, with a plateau above 1000 ℃. This suggests that for 2 hour heat treatments on undeformed specimens there will be little improvement in k_{pp}/k_3 for heat treatment temperatures hotter than 1000 ℃. The calculated dislocation densities for these four specimens using the method described in Section 4.2.2.1 show an inverse sigmoid dependence on T_{h}, with a plateau for $T_{\mathrm{h}} > 1000$ ℃, and displaying inverse proportionality to k_{pp}/k_3.

No clear correlation is visible between the variation in crystal orientation, as illustrated through the inverse pole figures, and the thermal conductivities of the specimens. Examining the k_{pp}/k_3 ratio with respect to E, as illustrated in Figure 4.29, for those specimens that had been heat treated at temperatures greater than 1000 ℃ reveals that there does exist a mild correlation between them. But the large scatter in data and the small slope of the least squares fit line indicates that crystal orientation has little influence on the thermal conductivity at the phonon peak.

In their as-received conditions, specimens 10 – 12 have similar LAM curves, implying similar dislocation contents. Although cut from an adjacent location in the same grain as specimens 10 – 12, specimen 9 has a smaller peak maximum and wider LAM curve than the other three specimens, indicating greater initial dislocation content than the other specimens in the set. After the 2 h heat treatments, specimens 9 – 11 have similar LAM curves, and are narrower than their as-received conditions. Specimen 12, heat treated at 1200 ℃, has an LAM curve that has the most shift in the peak maximum.

Specimen 9 has the most spread in the diffraction peaks, as illustrated in Figure 4.22, while specimen 12 with the 1200 ℃ heat treatment, plotted in Figure 4.25, has the least spread in the peaks. This implies that the hotter heat treatment temperature increases recovery in the crystal, and consequently reduces dislocation density in the specimens. This result is further highlighted when the normalized standard deviations for these peaks are compared, as shown in Figure 4.26. The average of the normalized standard deviation for specimen 12 is 66% smaller than that of specimen 9, while the same for specimens 10 and 11 are 14% and 24%, respectively.

The average of the full width at half maximum (FWHM) of each peak in the four clusters is an indication of crystal imperfection density, including dislocations and vacancies. The 1000 ℃ heat treated specimen 11 displays the least scatter in FWHM, implying least imperfection density. Although the 1200 ℃ heat-treated specimen had the greatest k_{pp}/k_3 ratio and least normalized standard deviation, implying the least number of phonon scattering sites, it displayed a wider FWHM than the 1000 ℃ heat-treated specimen.

To better understand the reason for the presence of a minimum in the FWHM at 1000 ℃, the equilibrium concentration of vacancies dependent on T are estimated. An Arrhenius type equation can be used to estimate the number of vacancies per unit volume (N_{v}) [60], such as

$$\frac{N_\mathrm{v}}{N} = \exp\left(\frac{-E_\mathrm{v}}{k_\mathrm{B}T}\right), \tag{4.5}$$

where E_v is the vacancy formation energy (2.65 eV for Nb [61]), k_B the Boltzmann constant (8.617 eV/K), T the temperature in K, and N the number of potential vacancy sites in the unit volume, calculated as

$$N = \rho\frac{N_\mathrm{A}}{M}, \tag{4.6}$$

where ρ is the density (8.57×10^6 g/m^3 for Nb), N_A the Avogadro's number (6.022×10^{23}), and M the molar mass (92.9 g/mol for Nb). The equilibrium vacancy concentration as a function of T is shown in Figure 4.34. As per the definition, N_v increases exponentially with T, and is evident in the plot. At $T_\mathrm{h} = 1200$ ℃, N_v is about an order of magnitude greater than that at $T_\mathrm{h} = 1000$ ℃.

As the thermal measurements for these specimens are performed at $T < 4.2$ K and since the specimens remain at room temperature most of the time, the estimate of N_v gives the upper limit of vacancy concentration for the specimens. Since vacancies need grain boundaries or dislocation cores to dissolve into, N_v for the single crystal specimens presented here can be expected to be mostly preserved even at cooler temperatures.

The inverse proportionality of the dislocation density with T_h, combined with the exponential dependence of the vacancy concentration on T_h leads to a local minimum in the total imperfection concentration. Therefore, according to the FWHM analysis, it is counter productive to heat treat undeformed Nb at $T_\mathrm{h} > 1000$ ℃. This result, in combination with k_pp/k_3 ratios and normalized standard deviations, also leads to the conclusion that phonon transport is affected by vacancies.

Comparing β_1 (scattering of normally conducting electrons by impurities) with the esti-

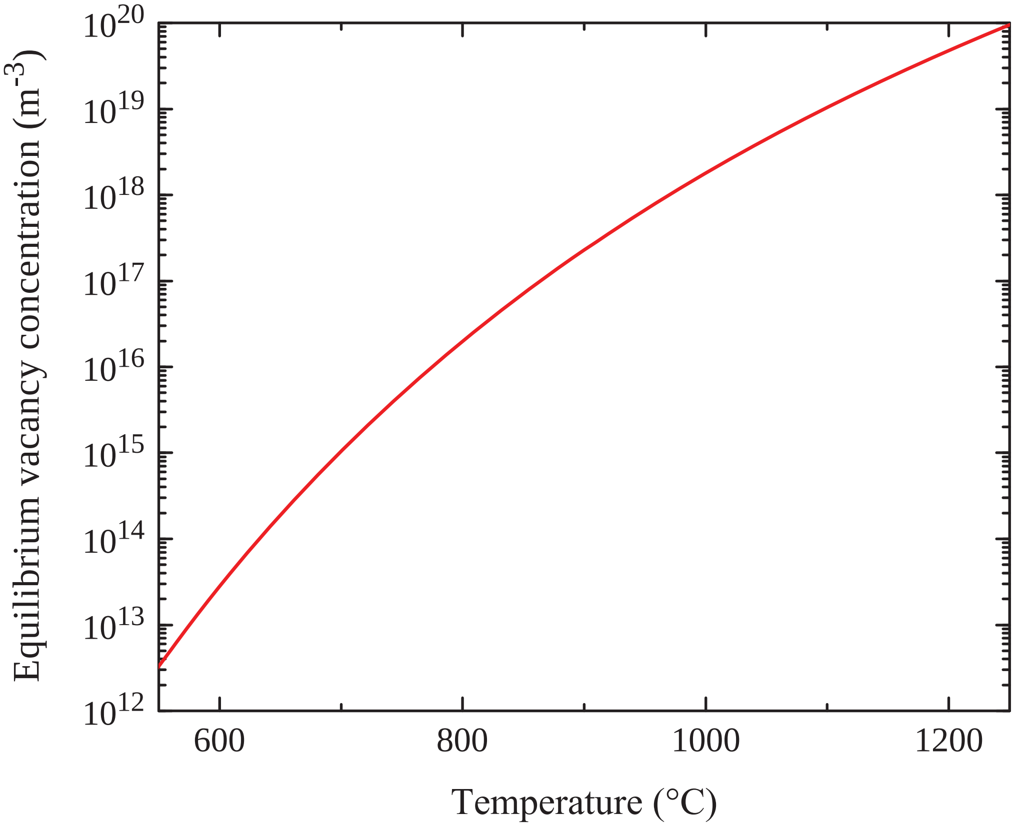

Figure 4.34: The theoretically calculated equilibrium vacancy concentration for Nb with respect to temperature.

mated RRR, for the twelve specimens in their as received condition and after heat treatments, results in an inverse relation between the two as shown in Figure 4.30. This is as expected from the definition of β_1 $(= \rho_{295}/(L\ \mathrm{RRR})^{-1})$. The inverse proportionality provides confidence in the parameter estimation technique used, since β_1 is a free parameter during estimation calculations.

The term for the scattering of phonons by normal conducting electrons β_3, illustrated in Figure 4.31, shows a mild dependence on the heat treatment temperature. The as-received, 600 ℃ for 6 h, 750 ℃, and 1000 ℃ heat-treated specimens have mean β_3 values that are significantly larger than the theoretical value. The 600 ℃ for 2 h, 800 ℃, 1100 ℃, and 1200 ℃ heat-treated specimens have β_3 that are centered about the calculated theoretical value. The cause for this deviation is not yet understood.

The term β_4 illustrated in Figure 4.32, which can be associated with the scattering of phonons by the lattice defects, shows a strong dependence on heat treatment temperature [62], with β_4 decreasing to about 20% of its as-received value for specimens after $T_\mathrm{h} >$ 1000 ℃ heat treatments. This again suggests a reduction in phonon scattering sites after heat treatment. The difference in β_4 between the 800 ℃ and the 1000 ℃ – 1200 ℃ heat treatments is not as dramatic as the difference between the as-received β_4 and the 800 ℃ heat treatments. This suggests that β_4 has an asymptotic dependence on the heat treatment temperature. Hence, heat treating at temperatures hotter than 1000 ℃ might not further decrease β_4. The small values of β_4 after 1000 ℃ – 1200 ℃ heat treatments imply that the lattice scattering sites formed during the production of the ingot might be annihilated and that β_4 might be reaching a limit due to the inability to remove geometrically necessary dislocations and boundary scattering.

The term associated with the condensation of electrons into Cooper pairs, β_5, shows little dependence on the temperature of heat treatment as shown in Figure 4.33. This might be expected due to the definition of β_5, which includes the superconductor energy gap $\Delta(T)$, the Boltzmann constant k_B, and the superconducting critical temperature T_c. The value for β_5 from BCS theory is 1.76, though measurements of $\Delta(T)$ have shown departures from this predicted value [63–66].

Based on the k and β_i data from Sets 1 and 2, no readily apparent effect was found of tantalum content on the thermal conductivity of niobium for concentrations between 523 and 1322 ppm.

4.6 Conclusion

The recovery of the phonon contribution to the phonon peak, by virtue of dislocation density, will have a sigmoidal dependence on the heat treatment temperature. The best values for the thermal conductivity at the phonon peak for 2 h heat treatments will be obtained around 1000 ℃. Although hotter heat treatment temperatures result in some improvement, the vacancy concentration also increases. The magnitude of the phonon peak is affected by vacancies generated during heat treatments. Smaller RRR will result in a smaller phonon peak. Crystal orientation plays little role in the variation of the thermal conductivity.

Chapter 5

Results: Deformation and the Phonon peak

The role of deformation and dislocation content on the magnitude of the phonon peak is examined using four bi-crystal Nb specimens. The specimens were uniaxially strained to different levels, with individual grains having different local engineering strains ranging from 2% to 38%. The corresponding change in the phonon peak was correlated with the strain and grain orientation for the individual grains.

The k at the phonon peak of deformed large grain Nb is known to recover to its undeformed value [25] subsequent to heat treatments at temperatures close to the melting temperature of Nb (2468 ℃). For the production of SRF cavities, however, heat treatment temperatures (T_h) need to be as small as possible, so as to not compromise their mechanical properties. The recovery of k at the phonon peak in the strained Nb specimens is examined here by heat treating the specimens for 2 h at a relatively colder temperature of 1000 ℃.

5.1 Uniaxial straining of specimens

Four bi-crystal Nb specimens, shaped according to the ASTM E-8 tensile standards, were subjected to different magnitudes of uniaxial tensile strain to observe the effect of dislocations on the magnitude of the phonon peak. Specimens 2, 3, 7, and 13 were subject to nominal engineering strains of 20, 10, 2, and 2 percent, respectively. Prior to deformation, specimens 2, 3, and 7 were heat treated at 1100 ℃ for 4 h, while specimen 13 was in its as-received condition. Using Euler angles obtained from orientation imaging microscopy, the Schmid factors and the direction of the Burger's vector were estimated using a MATLAB® code developed by Baars [67]. These parameters are listed in Table 5.1 for each specimen. A larger Schmid factor indicates that a grain will more readily deform. Based on these estimated Schmid factors and Burger's vector directions, the level of strain for each specimen was chosen. In addition, the characteristics of the recovery of the phonon peak with a 1000 ℃ for 2 h heat treatment subsequent to the deformation was also examined. The 1000 ℃ for 2 h heating was chosen as the recovery heat treatment based on the results presented in Chapter 4, where a plateau was observed in the recovery of k_{pp} for temperatures hotter than 1000 ℃.

Table 5.1: State of specimens prior to deformation. The Euler angles obtained using orientation imaging microscopy are also listed. Also tabulated are the Schmid factors for {110} and {112} slip systems, and the Burger's vector directions for these specimens. The level of strain chosen for these specimens based on the Schmid factors and Burger's vector directions are also tabulated.

Spec.	Grain	Euler angles in degrees			Largest Schmid factors[*]				Angle bet. Burger's vector and tensile direction in degrees				Chosen nominal strain (%)
		ϕ_1	Φ	ϕ_2									
2	1	9.7	18.4	351.8	**-0.493**	**0.484**	*-0.474*	*-0.469*	135.1	138.4	138.4	135.1	20
	2	64.7	40.8	261.2	**-0.469**	*-0.449*	**-0.365**	*-0.364*	53.8	53.8	155.9	53.8	
3	1	183.2	41.8	135.0	*0.387*	**0.350**	**-0.320**	*0.316*	64.6	64.6	64.6	70.2	10
	2	1.3	13.1	30.0	**-0.481**	*-0.469*	**-0.387**	*-0.363*	50.1	50.1	154.6	50.1	
7	1	157.3	40.3	168.5	*0.365*	**-0.318**	**0.314**	*-0.293*	66.6	66.6	66.6	108.0	2
	2	226.2	47.0	172.8	*-0.373*	**-0.337**	*0.325*	**-0.309**	114.2	114.2	69.6	114.2	
13	1	62.6	51.8	266.3	**-0.439**	**-0.425**	*-0.400*	*0.385*	120.9	60.7	120.9	60.7	2
	2	64.4	51.6	314.5	**-0.446**	*-0.429*	**-0.379**	*0.352*	57.4	57.4	114.9	114.9	

---

[*] **bold**: {110} slip system; *italics*: {112} slip system.

To better estimate the local strain on the two grains of each bi-crystal specimen, a 2 mm × 2 mm square grid was painted onto the surface of the specimens. The grid on specimen 2 in its as-received condition and after 20% nominal uniaxial tensile strain is shown in Figure 5.1. The location of the intersection of the grid lines before and after deformation was used to estimate the local strain. Also pictured is the side-view of the specimen before and after deformation.

Due to the differences in the Schmid factors of the two grains, the level of deformation is not the same for the two grains. This is shown in Figure 5.1(b). The grain with the greater Schmid factor has the softer orientation, and hence will yield more readily. Contrary to this rule of thumb, grain 2-1 (left grain in Figure 5.1(b)) despite having a greater Schmid factor than grain 2-2, has yielded less. The resulting local engineering strains for grains 2-1 and 2-2 were estimated to be 5% and 38%, respectively. This discrepancy in the expected softer orientation based on the Schmid factor was noted only for specimen 2. This may be explained by considering the number of slip systems being activated during deformation; this can be inferred from the number of unique Burger's vector directions tabulated for each grain in Table 5.1. Despite grain 2-1 having greater Schmid factors, it has two unique Burger's vector directions, while grain 2-2 has only one unique direction. This implies that even though grain 2-1 will yield before grain 2-2, it will also work harden faster, and thus it will deform less.

5.2 Thermal conductivities of strained specimens

The thermal conductivities for specimen 2 after the initial 1100 ℃ for 4 h heat treatment (open symbols), after 20% nominal uniaxial tensile strain (half-filled symbols), and after the

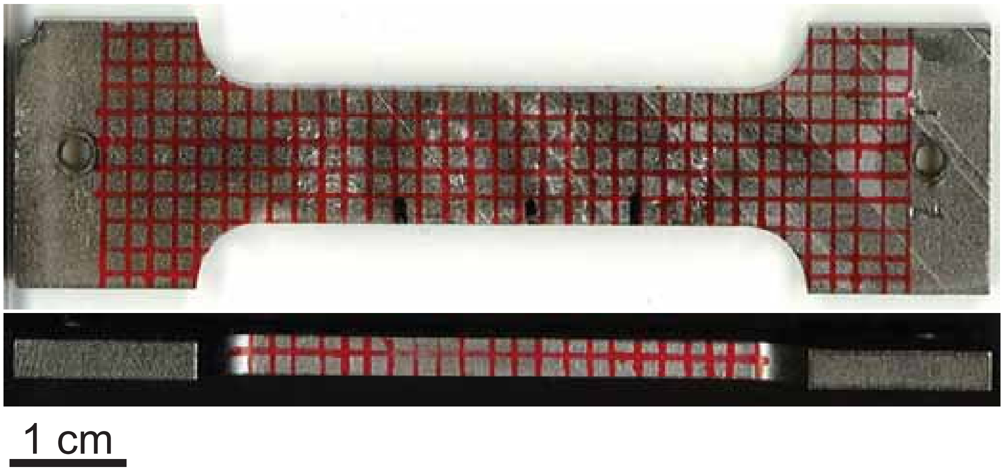

(a) Before deformation.

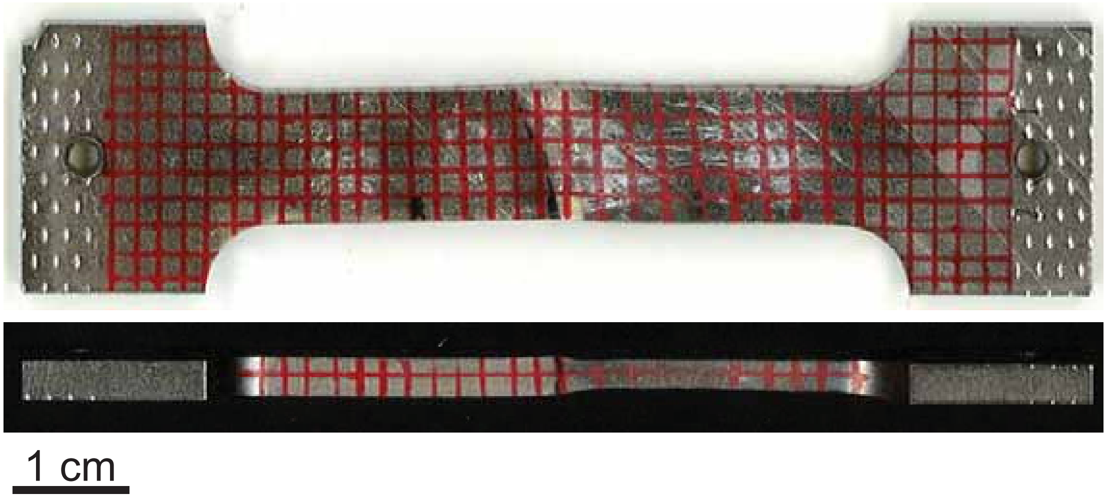

(b) After 20% nominal uniaxial tensile strain.

Figure 5.1: Painted 2 mm x 2 mm grid on the surface of specimen 2, (a) before deformation, and (b) after 20% nominal uniaxial tensile strain. This grid is used to estimate local strains on the two grains (left: grain 1, right: grain 2) of the bi-crystal specimen. Also pictured are the side-view of the specimen with the grid. The variable effect of deformation on the thickness of the two grains is visible in the side-view of (b). Similar grids were painted on the remaining three specimens.

1000 ℃ for 2 h recovery heat treatment (solid symbols) are illustrated in Figure 5.2. The Euler angles and an inverse pole figure illustrating the crystal orientations of the two grains are shown below the thermal conductivity plot in the figure. The thermal conductivities for specimen 3 after the initial 1100 ℃ for 4 h heat treatment (open symbols), after 10% nominal uniaxial tensile strain (half-filled symbols), and after the 1000 ℃ for 2 h heat treatment (solid symbols) are illustrated in Figure 5.3. The thermal conductivities for specimen 7 after the initial 1100 ℃ for 4 h heat treatment (open symbols), after 2% nominal uniaxial tensile strain (half-filled symbols), and after the 1000 ℃ for 2 h heat treatment (solid symbols) are illustrated in Figure 5.4.

A summary of the k results for the four specimens used in the deformation experiments is presented in Table 5.2. The results are tabulated as ratios of k at the phonon peak for the specimens before deformation ($k_{\mathrm{pp},1}$), after deformation ($k_{\mathrm{pp},2}$), and after the 1000 ℃ for 2 h heat treatment ($k_{\mathrm{pp},3}$). The ratio of $k_{\mathrm{pp},2}/k_{\mathrm{pp},1}$ presents the decrease in k_{pp} after deformation, while $k_{\mathrm{pp},3}/k_{\mathrm{pp},2}$ presents the increase in k_{pp} after the recovery heat treatment with respect to k_{pp} after deformation, and $k_{\mathrm{pp},3}/k_{\mathrm{pp},1}$ presents the relative change in k_{pp} after the 1000 ℃ heating with respect to k_{pp} before deformation. For cases where there was no phonon peak, such as specimen 13 in its as-received condition and after deformation, the k at 2 K is used. Also tabulated are the k_{pp}/k_3 ratios for the four specimens after the 1000 ℃ heat treatment. Additionally, the chosen nominal strains of the specimens and the measured engineering strains on the two grains of the specimens are also tabulated.

Previous work by Wasserbäch [26, 41, 42] and Singer *et al.* [27] consider the effects of deformation on k_{pp} of single crystal Nb, while Aizaz *et al.* [28] considered deformation on polycrystal Nb. Although there are several other publications in the literature discussing deformation and k in Nb, these five publications are chosen here due to the presence of

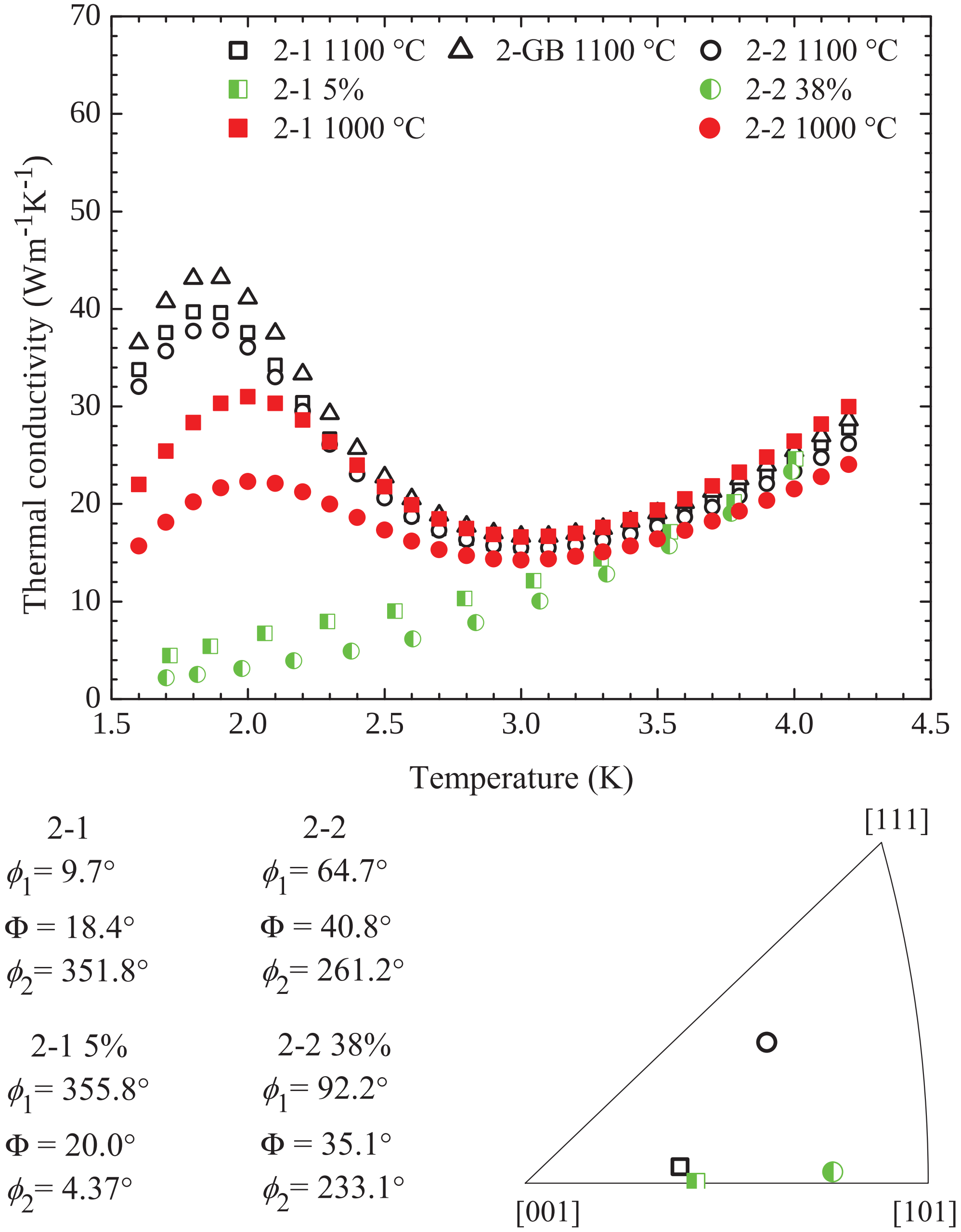

Figure 5.2: Thermal conductivities for specimen 2 after the 1100 ℃ for 4 h heat treatment (open symbols), after 20% nominal uniaxial tensile strain (half-filled symbols), and after the 1000 ℃ for 2 h recovery heat treatment (solid symbols). The thermal conductivity across the grain boundary (triangles) could not be estimated reliably after deformation, due to large variation in the cross sectional areas of the two grains in the specimen as visible in Figure 5.1(b). The Euler angels ϕ_1, Φ, and ϕ_2 as well as the inverse pole figure representing the crystal orientation along the heat flow direction for the two grains after the 1100 ℃ heating (open symbols) and after deformation (half-filled symbols) are shown below the thermal conductivity plot.

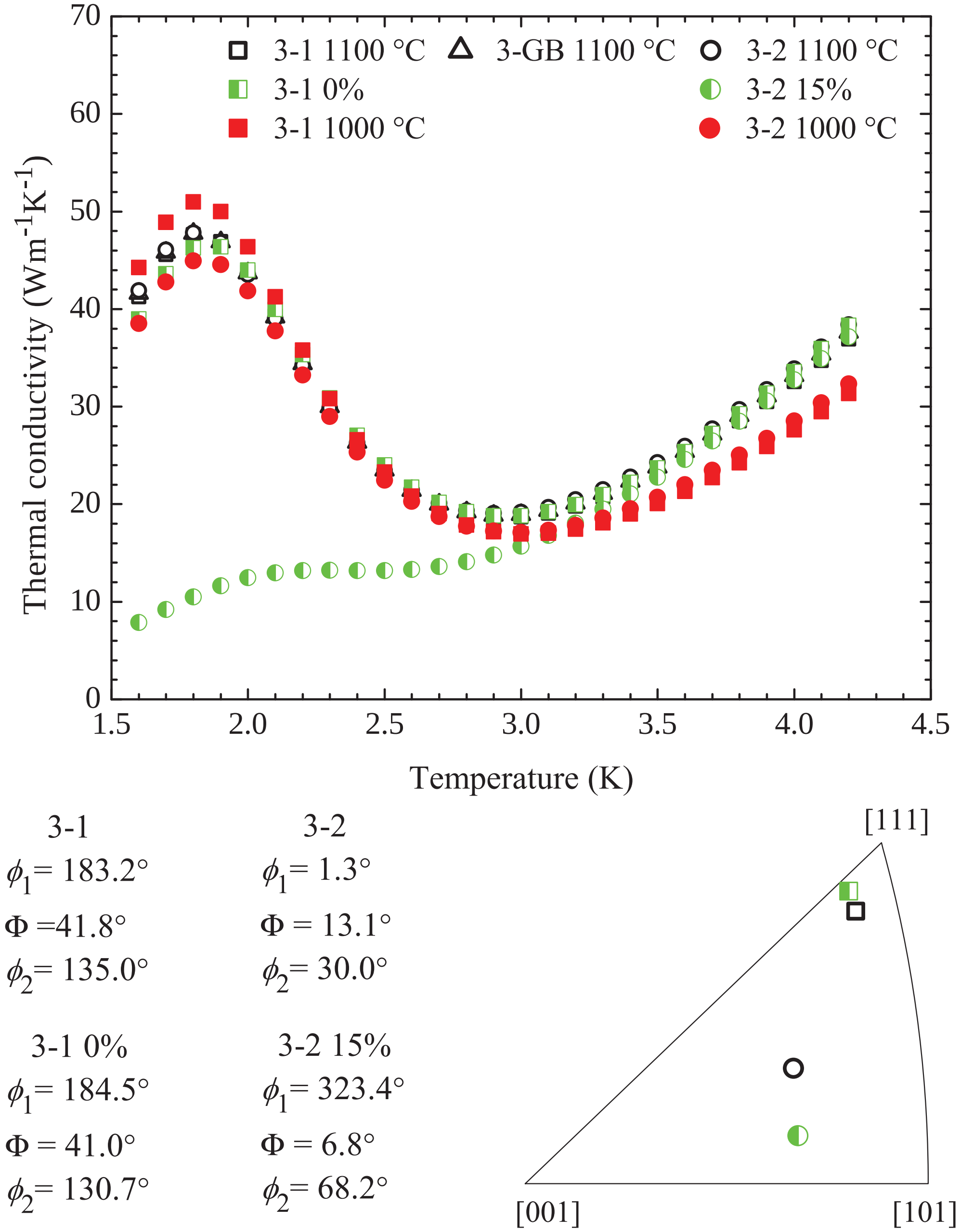

Figure 5.3: Thermal conductivities for specimen 3 after the 1100 ℃ for 4 h heat treatment (open symbols), after 20% nominal uniaxial tensile strain (half-filled symbols), and after the 1000 ℃ for 2 h recovery heat treatment (solid symbols). Similar to specimen 2, the thermal conductivity across the grain boundary (triangles) for specimen 3 could not be estimated reliably after deformation, due to large variation in the cross sectional areas of the two grains in the specimen. The Euler angels ϕ_1, Φ, and ϕ_2 as well as the inverse pole figure representing the crystal orientation along the heat flow direction for the two grains after the 1100 ℃ heating (open symbols) and after deformation (half-filled symbols) are shown below the thermal conductivity plot.

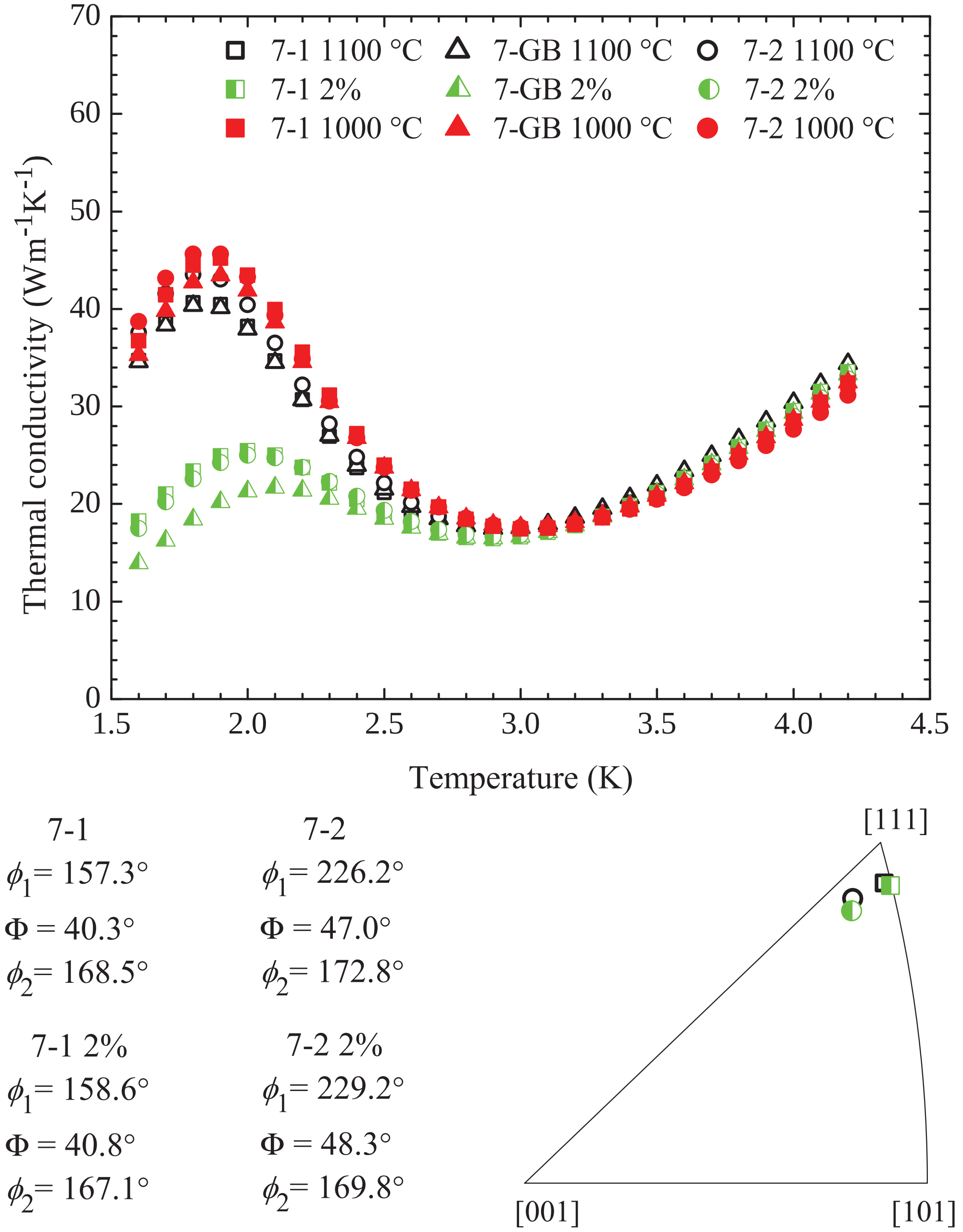

Figure 5.4: Thermal conductivities for specimen 7 after the 1100 ℃ for 4 h heat treatment (open symbols), after 2% nominal uniaxial tensile strain (half-filled symbols), and after the 1000 ℃ for 2 h recovery heat treatment (solid symbols). The Euler angels ϕ_1, Φ, and ϕ_2 as well as the inverse pole figure representing the crystal orientation along the heat flow direction for the two grains after the 1100 ℃ heating (open symbols) and after deformation (half-filled symbols) are shown below the thermal conductivity plot.

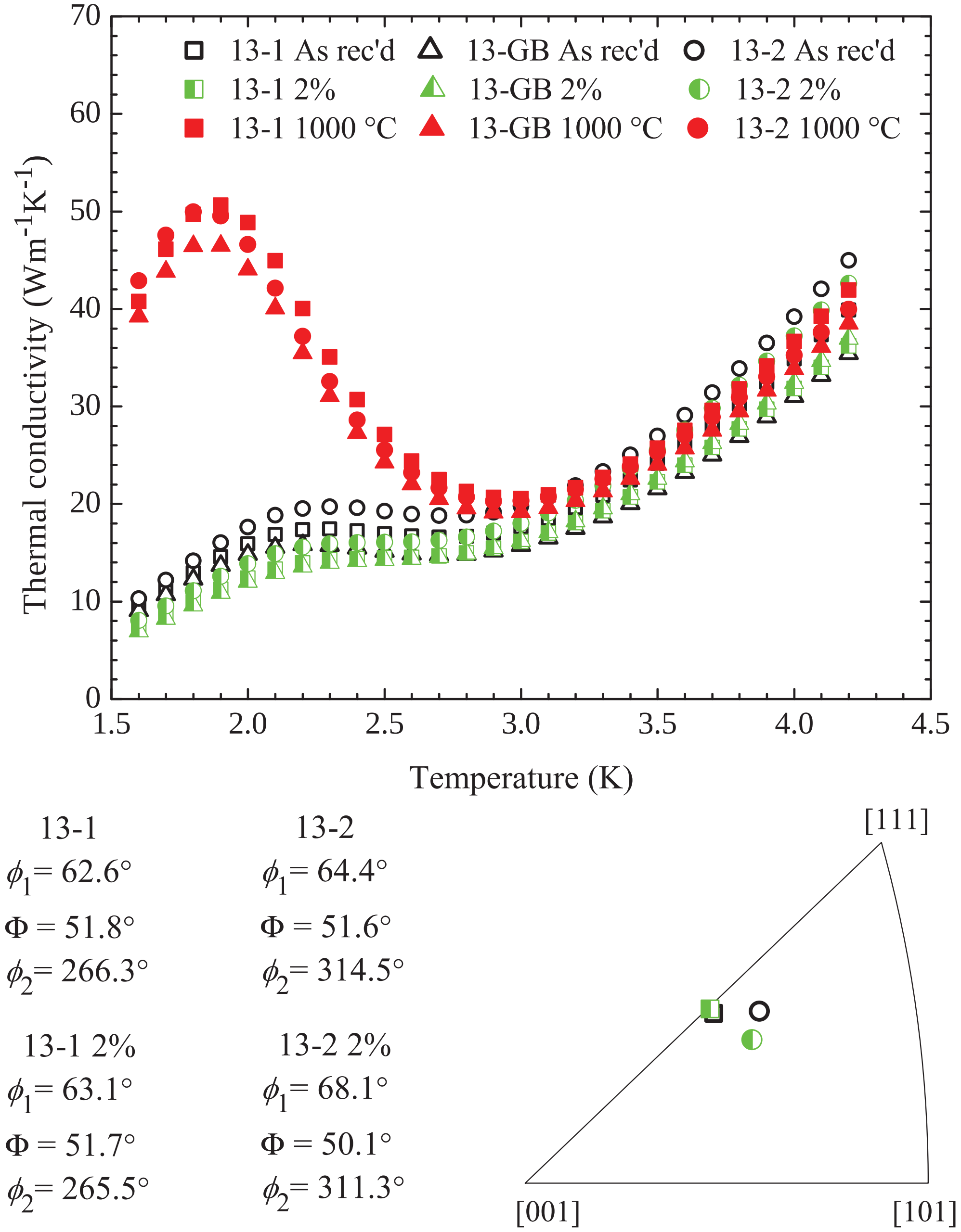

Figure 5.5: Thermal conductivities for specimen 13 in its as-received condition (open symbols), after 2% nominal uniaxial tensile strain (half-filled symbols), and after the 1000 ℃ for 2 h recovery heat treatment (solid symbols). The Euler angels ϕ_1, Φ, and ϕ_2 as well as the inverse pole figure representing the crystal orientation along the heat flow direction for the two grains in their as-received condition (open symbols) and after deformation (half-filled symbols) are shown below the thermal conductivity plot.

Table 5.2: Effect of uniaxial strain on the thermal conductivities of the two grains in specimens 2, 3, 7 and 13. Tabulated are the ratios of $k_{\mathrm{pp},2}/k_{\mathrm{pp},1}$, $k_{\mathrm{pp},3}/k_{\mathrm{pp},2}$, and $k_{\mathrm{pp},3}/k_{\mathrm{pp},1}$. The first ratio is a measure of the decrease in k_{pp} after deformation with respect to k_{pp} before deformation, the second ratio the increase in k_{pp} after the 1000 ℃ for 2 h heat treatment with respect to the k_{pp} after deformation, and the third ratio the change in k_{pp} after the 1000 ℃ for 2 h heat treatment with respect to the k_{pp} before deformation. In the ratios, $k_{\mathrm{pp},1}$ is the k at the phonon peak before deformation, $k_{\mathrm{pp},2}$ the k_{pp} after deformation, and $k_{\mathrm{pp},3}$ the k_{pp} after the 1000 ℃ heat treatment. In cases where there is no phonon peak, k at 2 K is used. Additionally, the k_{pp}/k_3 values for the specimens after the 1000 ℃ heat treatment are listed. Also tabulated are the chosen nominal strains along with the measured engineering strains on the two grains of the specimens.

Specimen	Grain	Chosen nominal strain (%)	Measured engg. strain (%)	$\frac{k_{\mathrm{pp},2}}{k_{\mathrm{pp},1}}$	$\frac{k_{\mathrm{pp},3}}{k_{\mathrm{pp},2}}$	$\frac{k_{\mathrm{pp},3}}{k_{\mathrm{pp},1}}$	After 1000 ℃ k_{pp}/k_3
2	1	20	5	0.17	4.63	0.78	1.87
	2		38	0.08	7.19	0.59	1.57
3	1	10	0	0.98	1.10	1.07	3.02
	2		15	0.26	3.60	0.94	2.61
7	1	2	2	0.63	1.77	1.11	2.60
	GB		2	0.54	2.00	1.07	2.47
	2		2	0.58	1.82	1.05	2.59
13	1	2	2	0.78	4.08	3.18	2.46
	GB		2	0.88	3.88	3.39	2.42
	2		2	0.79	3.60	2.84	2.46

before-deformation k in them for the corresponding strained Nb specimens. Wasserbäch also considered the effect of the temperature at which deformation occurred (T_{def}), by straining several specimens at temperatures ranging between $77 \leq T_{\mathrm{def}} \leq 470$ K. Additionally, the specimens were strained in several steps before reaching the final strain condition, with intermediate k measurements at each strain level. The specimens strained by Singer [27] and Aizaz [28], and the specimens presented in this work, were all strained at $T_{\mathrm{def}} = 295$ K. A comparison of the change in k_{pp} after deformation with respect to k_{pp} before deformation ($k_{\mathrm{pp},2}/k_{\mathrm{pp},1}$) as a function of engineering strain for the data from literature and those presented in this work are illustrated in Figure 5.6. Inserted in the figure is the inverse pole figure with orientations for specimens presented in this work, along with those for Wasserbäch's specimens. A $k_{\mathrm{pp},2}/k_{\mathrm{pp},1}$ value of unity implies no change in k_{pp} after deformation, while a value smaller than unity implies reduction in k_{pp} after deformation.

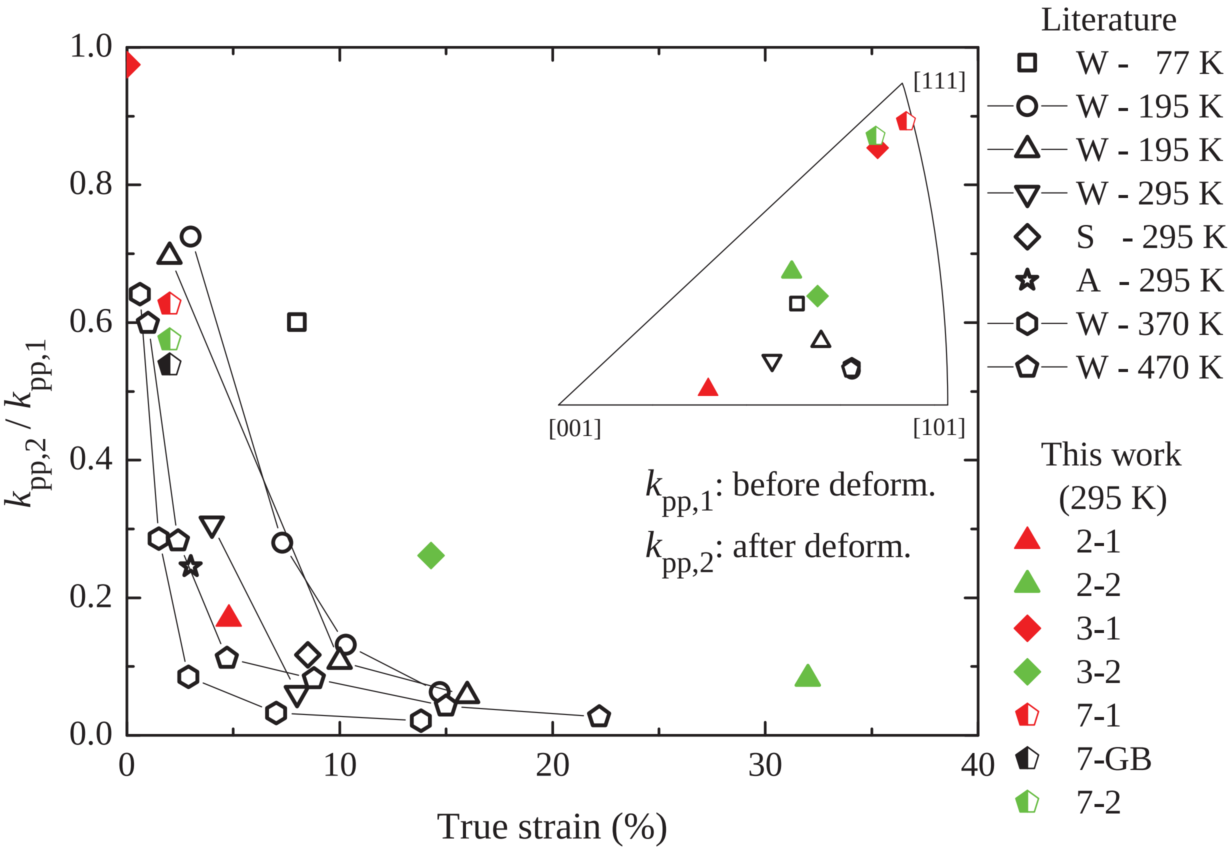

Figure 5.6: The change in k_{pp} after deformation with respect to k_{pp} before deformation ($k_{\text{pp},2}/k_{\text{pp},1}$) as a function of the engineering strain for the bicrystal specimens 2, 3, and 7 (different squares) are compared with the data from single crystal Nb specimens presented by Wasserbäch [26, 41, 42] and Singer *et al.* [27], and polycrystal Nb presented by Aizaz *et al.* [28]. $k_{\text{pp},2}/k_{\text{pp},1} = 1$ implies no change in k_{pp} after deformation. A value smaller than unity implies reduction in k_{pp} after deformation. The data from Wasserbäch, Singer, and Aizaz are differentiated in the legend with a "W", "S", and "A", respectively. Lines are added to aid in presentation and do not represent a model. Inserted is the inverse pole figure with orientations for specimens presented in this work, along with those for Wasserbäch's specimens.

5.3 Discussion

5.3.1 Deformation on k_{pp}

In Figure 5.6, at first glance, the amount of reduction in k_{pp} after deformation for Wasserbäch's specimens seem to display a dependence on T_{def}. Closer examination by considering the crystal orientation reveals that the three data points with anomalously high $k_{\text{pp},2}/k_{\text{pp},1}$ values, Wasserbäch's 77 K specimen along with grains 2-2 and 3-2, have crystal orientations that lie at the center of the inverse pole figure, indicating single slip in these specimens. The remaining specimens have duplex slip, and generate more dislocations during deformation due to the interaction of the slip systems.

The specimens with duplex or multiple slip display greater reduction in k_{pp} after deformation. Strains as small as $\epsilon \approx 2\%$ and 5% results in decreases in k_{pp} of more than 37% and 83%, respectively. The conductivity ratio quantifying the decrease in k_{pp} after deformation $k_{\text{pp},2}/k_{\text{pp},1}$, for specimens with multiple slip, asymptotically converges to values smaller than 0.05 (greater than 95% reduction in k_{pp}) for strains greater than $\epsilon \approx 15\%$. These results indicate that dislocations generated during deformation are major phonon scattering sites.

Depending on the crystal orientation of adjacent grains in large grain Nb, by virtue of the Schmid factors and number of slip systems, deformation can result in preferential thinning of grains such as that illustrated in Figure 5.1(b). Such differences in the thickness is undesirable for SRF cavities, where surface smoothness is vital. Therefore, to estimate the effects of deformation of large grain Nb, it is vital to know not only the level of strain endured by large grain material but also the Schmid factors of the adjacent grains and the number of primary slip systems that will be activated during deformation.

5.3.2 Recovery of k_{pp}

The four single crystal specimens (Set 2) presented in Chapter 4, heat-treated for 2 h each at a temperature between 600 ℃ – 1200 ℃, displayed a plateau in the recovery of k_{pp} for temperatures hotter than 1000 ℃. Based on this result, a 1000 ℃ for 2 h heating was performed on the deformed specimens, to observe the recovery of the phonon peak.

After the 1000 ℃ for 2 h recovery heat treatment, k_{pp} for both grains and across the grain boundary in the 2% strained specimen 7 recovered to at least 5% greater than the phonon peak before deformation. The k_{pp} for the grains in the 2% strained specimen 13 after the 1000 ℃ heat treatment increased 300%, and had an average k_{pp}/k_3 ratio of 2.45. This value of k_{pp}/k_3 is consistent with those for the specimens in Sets 1 and 2 from Chapter 4, heat treated at $T_{\mathrm{h}} \geq 1000$ ℃, indicating the attainment of the maximum in k at the phonon peak for this specimens' purity.

The 1000 ℃ for 2 h heat treatment caused a 10% increase in k_{pp} for the 0% strained grain 3-1 of specimen 3. The k_{pp} for grain 3-2 with 15% engineering strain, after the 1000 ℃ heat treatment, recovered to 94% of the before deformation k_{pp}. Though no change was observed in k for $T \gtrsim 3.5$ K for the two grains after deformation, a 15% decrease in k for $T \gtrsim 3.5$ K was observed for both grains after the 1000 ℃ for 2 h recovery heat treatment. This decrease in k for $T \gtrsim 3.5$ K combined with the 10% increase in k_{pp} for grain 3-1, led to the increase of k_{pp}/k_3 from 2.55 before deformation (after 1100 ℃ heat treatment), to 3.02 after the 1000 ℃ heat treatment. This value of k_{pp}/k_3 is the greatest for all the specimens and conditions, including the 1100 ℃ for 4 h heating.

The 5% and 38% strained grains 2-1 and 2-2, respectively, did not display complete recovery in k_{pp} after the 1000 ℃ for 2 h recovery heat treatment. Grain 2-1, which had a

5% engineering strain and an 83% decrease in k_{pp} after deformation, recovered partially to 78% of the undeformed k_{pp}. On the other hand, after deformation, grain 2-2 had a 38% engineering strain with a 92% decrease in k_{pp}. After the 1000 ℃ for 2 h heat treatment, the phonon peak recovered to 59% of k_{pp} in the undeformed condition. No significant change was observed in k for $T \gtrsim 3.5$ K for grain 2-1 after deformation and after the 1000 ℃ heating. Grain 2-2 also had no change in k for $T \gtrsim 3.5$ K after deformation. After the 1000 ℃ heating, however, an 8% decrease in k at 4.2 K was observed for Grain 2-2, which may be attributed to introduction of small quantities of impurities from the furnace.

The k_{pp}/k_3 ratios after the 1000 ℃ heat treatment for the grains with engineering strains $\geq 5\%$, *i.e.*, grains 2-1 (square), 2-2 (triangle), and grain 3-2 (circle), are compared in Figure 5.7 with the sigmoidal curve fit to the k_{pp}/k_3 data for the 2 h heat-treated specimens of Set 2 in Figure 4.15 of Chapter 4. While the 15% strained grain 3-2, after the 1000 ℃ recovery heat treatment, displays a k_{pp}/k_3 value comparable with the undeformed values for this heat treatment temperature, the 5% strained grain 2-1 has a k_{pp}/k_3 value that is 28% smaller than that of grain 3-2. Grain 2-2, deformed to 38% engineering strain, has a k_{pp}/k_3 value that is 40% smaller than that of grain 3-2. Grains 2-1 and 2-2 clearly display incomplete recovery.

Plotting the ratios of $k_{\mathrm{pp},2}/k_{\mathrm{pp},1}$ and $k_{\mathrm{pp},3}/k_{\mathrm{pp},2}$ with each other, illustrated as the squares in Figure 5.8, uncovers an exponential relation between the two. In the ratios, $k_{\mathrm{pp},1}$ is the k_{pp} before deformation, $k_{\mathrm{pp},2}$ the k_{pp} after deformation, and $k_{\mathrm{pp},3}$ the k_{pp} after the 1000 ℃ for 2 h heat treatment. A smaller $k_{\mathrm{pp},2}/k_{\mathrm{pp},1}$ ratio indicates greater reduction in k_{pp} after deformation, while a smaller $k_{\mathrm{pp},3}/k_{\mathrm{pp},2}$ ratio indicates no recovery of k_{pp} due to the 1000 ℃ heat treatment. For both ratios, a value closer to unity implies no change in k_{pp}. The exponential relation between the decrease in k_{pp} after deformation and increase in k_{pp} after

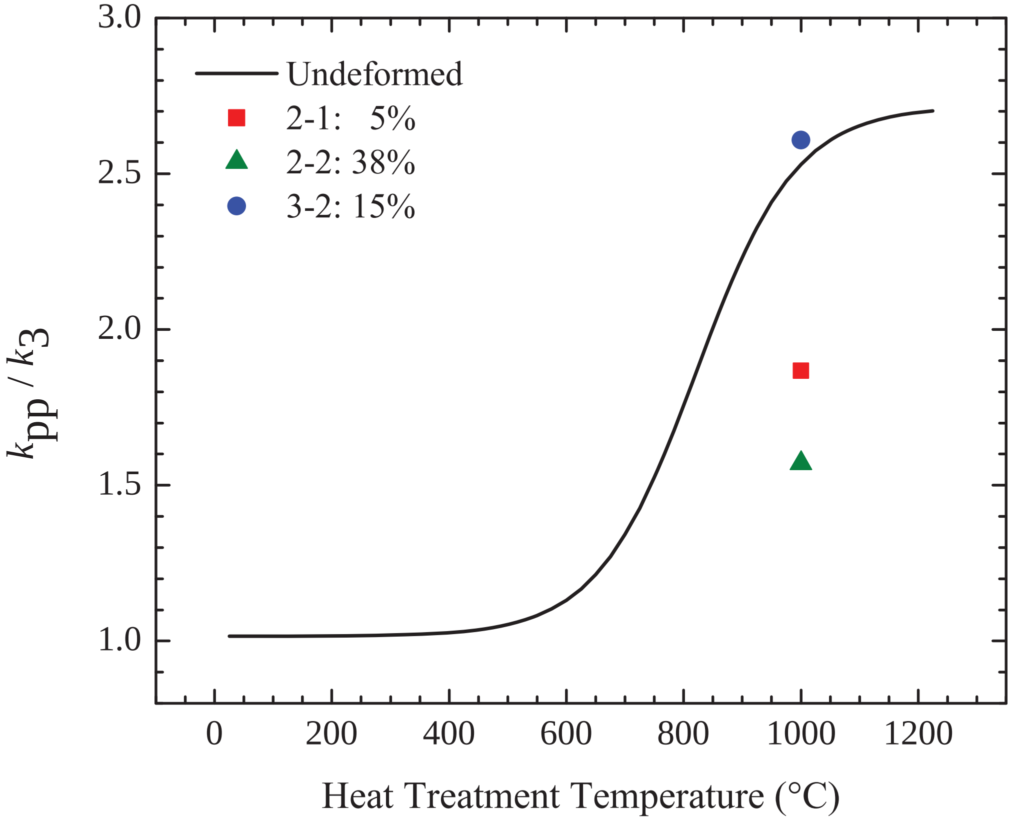

Figure 5.7: Comparison of k_{pp}/k_3, for the three grains with engineering strains $\geq 5\%$, with the sigmoidal curve from Figure 4.15, fit to the k_{pp}/k_3 data for the 2 h heat-treated specimens of Set 2 in Chapter 4.

the 1000 ℃ heat treatment is highlighted by plotting $\left[1 - (k_{\mathrm{pp},3}/k_{\mathrm{pp},2})\right] \cdot 100$ as a function of $\left[(k_{\mathrm{pp},3}/k_{\mathrm{pp},2}) - 1\right] \cdot 100$, as shown in Figure 5.9. Since the magnitude of the phonon peak is inversely proportional to the dislocation density, the exponential correlation illustrated in Figure 5.9 implies greater initial dislocation contents lead to greater recovery of dislocations during heat treatments, irrespective of crystal orientations. Data from specimen 13 were omitted from this correlation since it did not have a phonon peak in the before-deformation condition. Also compared in Figure 5.8 are the relation between $k_{\mathrm{pp},2}/k_{\mathrm{pp},1}$ and $k_{\mathrm{pp},3}/k_{\mathrm{pp},1}$ (triangles), where $k_{\mathrm{pp},3}/k_{\mathrm{pp},1}$ is a measure of how much k_{pp} has recovered with respect to k_{pp} before deformation. Examining these correlations, it can be inferred that although there is greater recovery after the introduction of more dislocations, the recovery is incomplete for the larger dislocation concentrations. For SRF cavities, hence, from the perspective of obtaining greater k_{pp} and due to the economics of heat treatments, it is beneficial to minimize the number of dislocations generated during fabrication and processing.

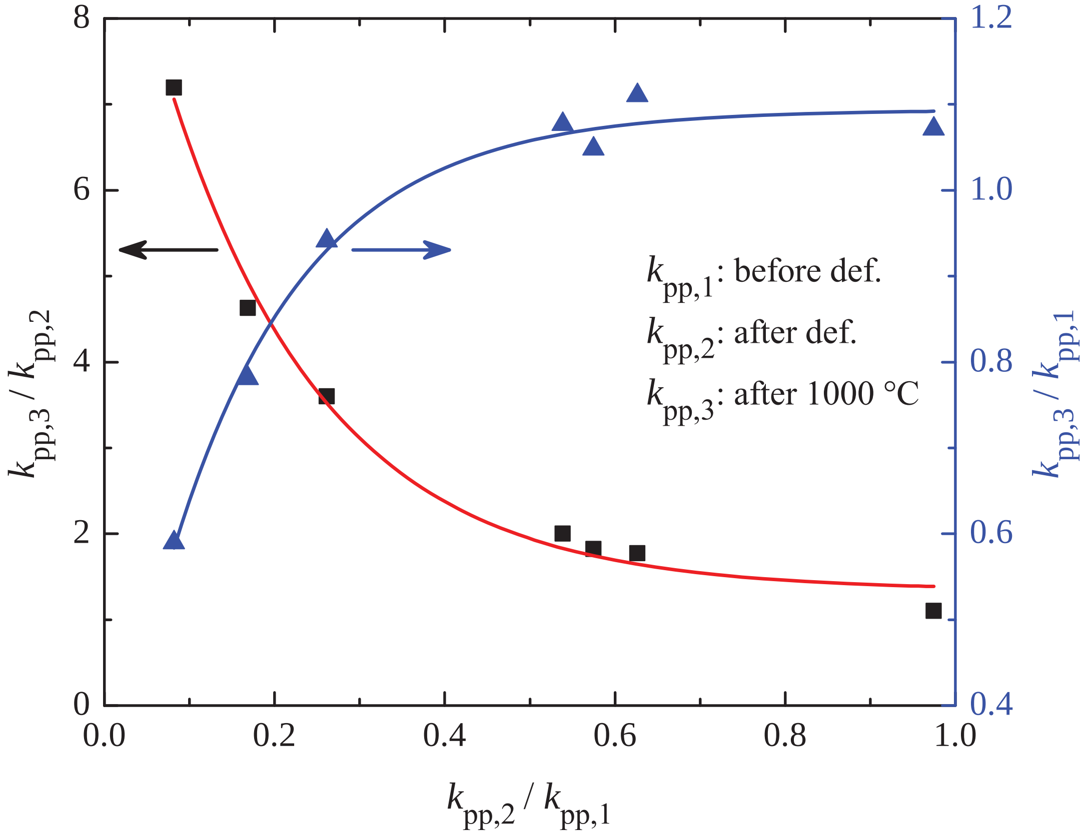

Figure 5.8: The change in k_{pp} after deformation with respect to that before deformation (abscissa) is compared with the change in k_{pp} after the 1000 ℃ recovery heat treatment with respect to that after deformation (left ordinate) and the change in k_{pp} after the 1000 ℃ recovery heat treatment with respect to that before deformation (right ordinate) for specimens 2, 3, and 7. For all three ratios, a value of unity implies no change in k_{pp}, while a value smaller than unity implies reduction in k_{pp}. An exponential relation is visible between $k_{\mathrm{pp},2}/k_{\mathrm{pp},1}$ and $k_{\mathrm{pp},3}/k_{\mathrm{pp},2}$, with greater reduction in k_{pp} after deformation leading to greater recovery of k_{pp} after heat treatment. This implies that greater dislocation density leads to greater recovery of dislocations during heat treatments, irrespective of crystal orientations. The solid lines represent exponential curve fits to the data for specimens 2, 3, and 7. Since specimen 13 did not have a phonon peak before deformation, the corresponding data points are omitted from this plot.

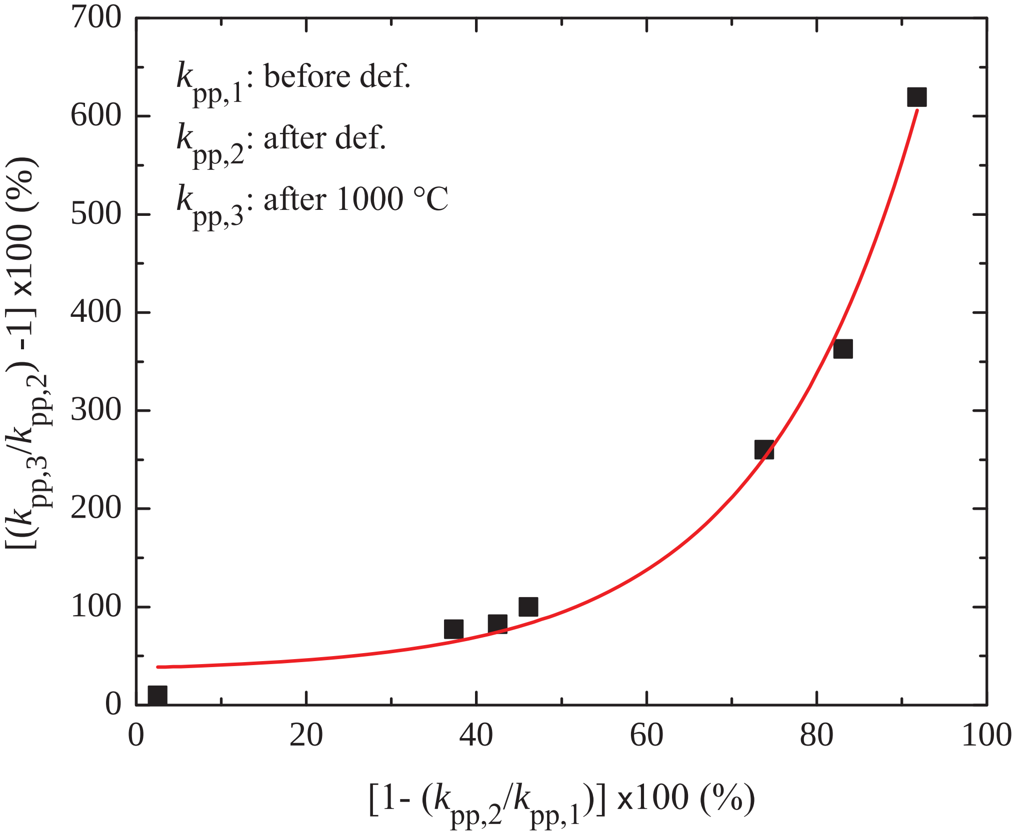

Figure 5.9: Comparison between the decrease in k_{pp} after deformation (abscissa) and increase in k_{pp} after the 1000 ℃ recovery heat treatment (ordinate) for specimens 2, 3, and 7. An exponential relation is visible between the two, with greater reduction in k_{pp} after deformation leading to greater recovery of k_{pp} after heat treatment. This implies that greater dislocation density leads to greater recovery of dislocations during heat treatments, irrespective of crystal orientations. The solid line represents an exponential curve fit to the data for specimens 2, 3, and 7. Since specimen 13 did not have a phonon peak before deformation, the corresponding data points are omitted from this plot.

5.4 Conclusion

Uniaxial engineering strain as small as $\epsilon \approx 2\%$ is sufficient to reduce the phonon peak by more than 37%. The magnitude of decrease in k at the phonon peak is not only related to the level of deformation, but is also strongly influenced by the grain orientation along the direction of deformation, by virtue of the number of slip systems being activated during deformation. A 5% strain with duplex slip during deformation causes the phonon peak to reduce by 83%, while a 15% strain with single slip reduces the phonon peak by just 72%.

The recovery of k at the phonon peak, by virtue of dislocation recovery, is proportional to the magnitude of the dislocations introduced during deformation. A 1000 ℃ for 2 h heat treatment is sufficient to recover the phonon peak in grains with up to $\leq 74\%$ reduction in the phonon peak due to strain-induced dislocations.

Chapter 6

Results:

Hydrogen and the Phonon Peak

During fabrication of SRF cavities, BCP or EP is regularly used to etch the interior (RF) surface of the cavity to remove surface irregularities. This step is known to introduce hydrogen from the acid into the bulk due to the removal of the impermeable niobium pentoxide layer from the surface, leading to “Q-disease”. The effect of hydrogen on the thermal conductivity of superconducting niobium is being studied here.

6.1 Infusing hydrogen into niobium

Three bicrystal niobium specimens were infused with hydrogen in a 75% H_2, 25% N_2 environment at 0.5 atm ($P_{H_2} = 0.375$ atm). The hydrogen infusion was carried out in a custom built brazing furnace at Michigan State University. The coolest temperature that can be stably maintained in the furnace is 300 ℃, while the maximum pressure is limited to 0.5 atm. For hydrogen to flow into Nb, the impermeable niobium-pentoxide (Nb_2O_5) layer has to be dissolved. It has been observed [68] that the Nb_2O_5 layer dissolves within minutes at $T \geq 250$ ℃, hence the 300 ℃ is an optimum temperature to introduce hydrogen into the material.

The characteristic distance of diffusion x_d was estimated as

$$x_\mathrm{d} = \sqrt{Dt}, \tag{6.1}$$

where D is the diffusion coefficient, and t the time. For the hydrogen-niobium system at 300 ℃, $D \approx 5.5 \times 10^{-5}$ $\mathrm{cm^2s^{-1}}$ [69]. For a duration of 1 hour, $x_\mathrm{d} = 4.45$ mm, estimated to be sufficient to diffuse hydrogen through the 3 mm thickness of the specimens.

Of the three specimens examined, one was used to measure the concentration of hydrogen, while the remaining two (specimens 5 and 8) were used to measure the thermal conductivity. Prior to H_2 infusion, specimen 5 had been heat treated at 800 ℃ for 2 h in a high-temperature, high-vacuum furnace at Michigan State University [30]. Specimen 8 had been heat treated twice before the H_2 treatment, first at 140 ℃ for 48 h, and second at 1100 ℃ for 4 h. The RRR and processing histories of these two specimens prior to H_2 infusion are listed in Table 6.1, along with the H_2 infusion parameters and the H_2 degassing heat treatment data.

6.1.1 Hydrogen concentration

The concentration of hydrogen in specimens 5 and 8 were estimated using the temperature and duration during infusion, pressure of hydrogen during the infusion, and a survey of experimentally obtained solubility curves for hydrogen in niobium [70, Chapter 2]. For a temperature of 300 ℃ (573 K) and pressure of 0.375 atm, yields the concentration of

Table 6.1: Hydrogen specimen histories.

		Heat Treatment (HT)				Hydrogen Treatment				
		First HT		Second HT		H_2 infusion			Recovery HT	
Spec.	Est. RRR	T_h (℃)	t (h)	T_h (℃)	t (h)	T_{H2} (℃)	t_{H2} (h)	P_{H2} (atm)	$T_{h,H2}$ (℃)	t_{H2} (h)
5	104	800	2			300	1	0.375	800	2
8	200	140	48	1100	4	300	1	0.375	800	2

hydrogen in niobium (ratio of the number of atoms of hydrogen to that of niobium) to be ~0.7, or 41.2 at. % of hydrogen.

Depending on the concentration of hydrogen in niobium and the temperature of the specimen, several niobium-hydrogen phases have been identified, and are represented as the niobium-hydrogen phase diagram [71, 72]. After the hydrogen infusion at 300 ℃ the Nb-H system would have been in the α' phase for specimens 5 and 8. Consequently, during cooling the Nb-H system would have transformed from α' to $\alpha' + \beta$ at ~115 ℃, and to $\alpha + \beta$ at ~85 ℃.

6.2 Thermal conductivity

The thermal conductivity for specimen 5 after the first 800 ℃ heat treatment (open symbols), after hydrogen infusion (solid symbols), and after the 800 ℃ hydrogen degassing heating (half filled symbols) are illustrated in Figure 6.1. Curves for the estimated k, as a function of temperature, for the two grains and across the grain boundary are illustrated. The results indicate that hydrogen can be a significant scattering source for phonons. Figure 6.2 illustrates the thermal conductivity for the two grains and across the grain boundary of

Table 6.2: Ratio of k at the phonon peak to that at 3 K for specimens 5 and 8 before hydrogen infusion, after hydrogen infusion, and after hydrogen degassing heat treatment at 800 ℃ for 2 h.

	k_{pp}/k_3		
Spec.	Before H_2	With H_2	After 800 ℃
5-1	2.47	1.81	2.27
5-2	2.28	1.86	2.57
5-3	2.45	1.88	2.52
8-1	–	2.23	2.19
8-2	2.66	2.27	2.40
8-3	2.68	2.22	2.29

specimen 8 after the 1100 ℃ heat treatment (open symbols), after hydrogen infusion (solid symbols), and after the 800 ℃ for 2 h heating to degas hydrogen (half filled symbols). The ratios of k at the phonon peak k_{pp} and that at 3 K k_3 for the two hydrogen specimens in their pre-hydrogen infusion state, with hydrogen in them, and after the 800 ℃ for 2 h degassing heat treatment are listed in Table 6.2.

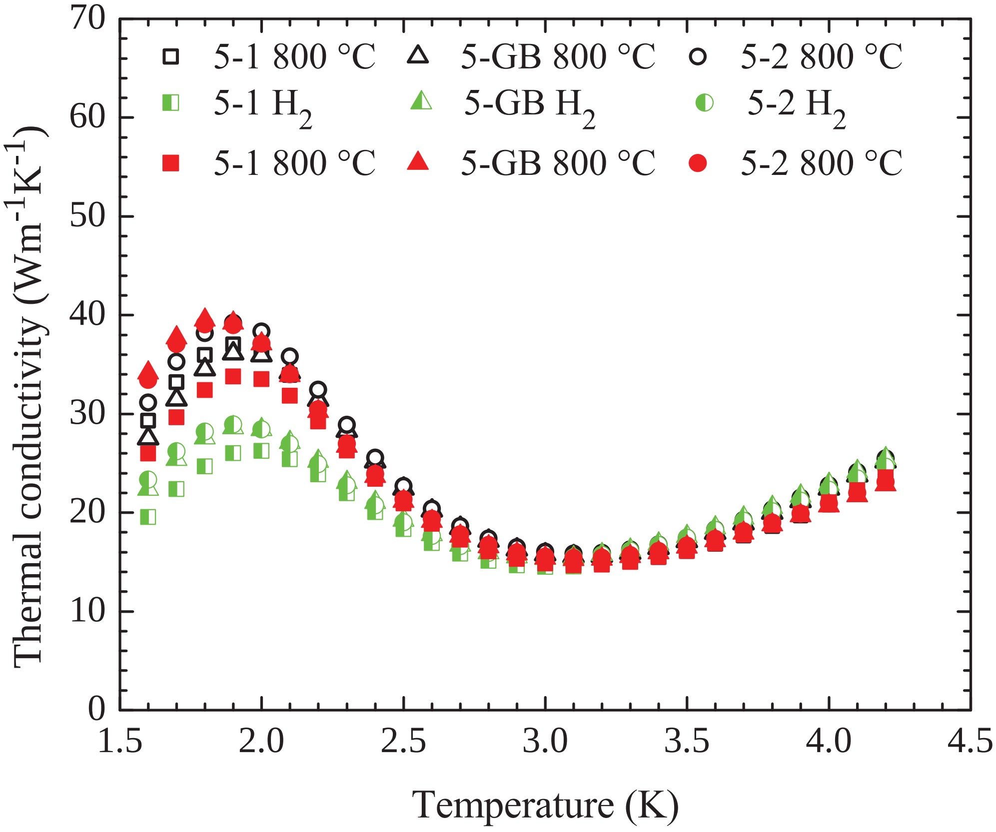

Figure 6.1: Thermal conductivity curves for specimen 5 after the first 800 ℃ heat treatment (open symbols), after hydrogen infusion (solid symbols), and after the hydrogen degassing heat treatment at 800 ℃ for 2 h (half filled symbols). Conductivity curves estimated from each of the three temperature sensor pairs are illustrated. After hydrogen infusion, a 25% reduction in the magnitude of the phonon peak was observed for sensor pairs 2 and 3, while a 30% reduction was noted for sensor pair 1. No change was detected in k for $T > 3$ K. After the 800 ℃ for 2 h heating to degas hydrogen from the specimen, k at the phonon peak was recovered to the before state for sensors 2 and 3. For sensor pair 1, the degassing heating recovered the k at the phonon peak to approximately 9% less than its before hydrogen infusion condition.

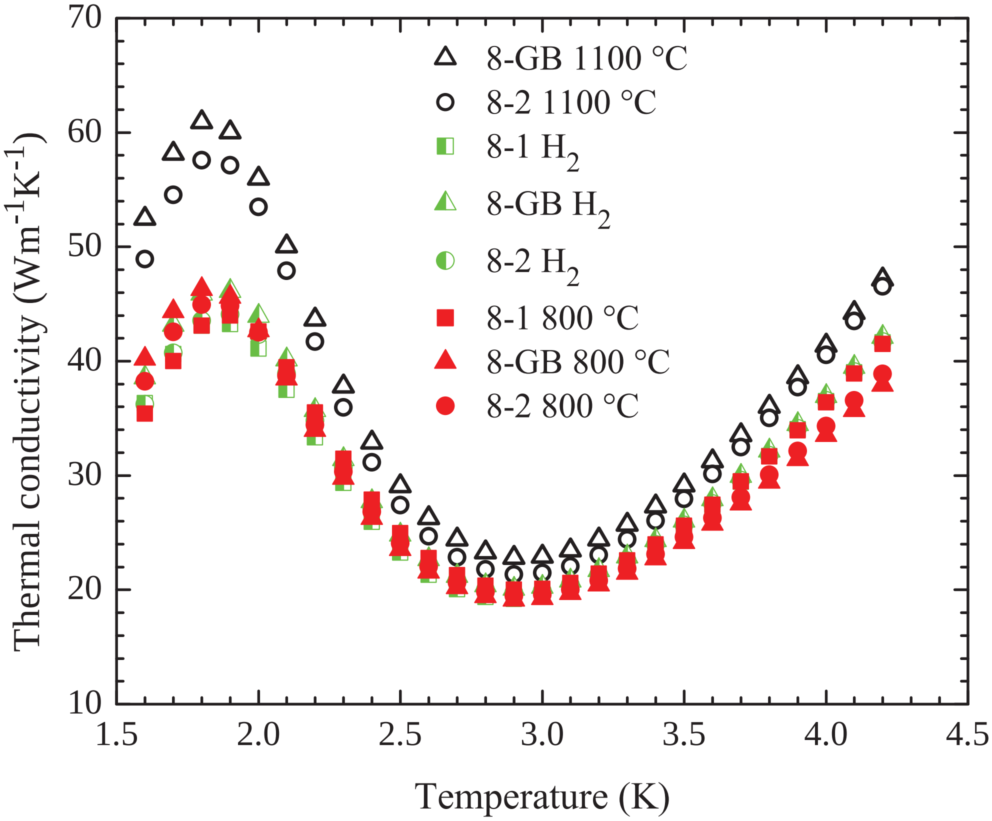

Figure 6.2: Thermal conductivity curves for specimen 8 after the 1100 ℃ heat treatment (open symbols), after hydrogen infusion (solid symbols), and after the hydrogen degassing heat treatment at 800 ℃ for 2 h (half filled symbols). Conductivity curves estimated from each of the three temperature sensor pairs are illustrated. After hydrogen infusion, a 25% reduction in the magnitude of k at the phonon peak was observed along with a 10% reduction in k at 4.2 K. The 800 ℃ for 2 h heating to degas hydrogen from the specimen showed no effect on the conductivity at the phonon peak, though a mild decrease in k for $T > 3$ K was noted.

6.3 Discussion

The thermal conductivity at the phonon peak for specimen 5, grain 1, showed a 30% decrease after the introduction of hydrogen. Similarly, the k_{pp} of Grain 5-2, 5-GB, and the k at the phonon peak of both grains and across the grain boundary of specimen 8 displayed a 25% reduction due to the presence of hydrogen. These suggest that the excess hydrogen acts as a scattering source for phonons, by probably precipitating into hydrides. No change was observed in k for $T > 3$ K for specimen 5, implying that the excess hydrogen is not a major scattering source for electrons. Contrary to this, k for $T > 3$ K for specimen 8 after hydrogen infusion displayed a 10% reduction. Note that the RRR, prior to hydrogen infusion, for specimens 5 and 8 were 104 and 200, respectively. This indicates that for the estimated concentration of hydrogen, there is sufficient hydrogen present to reduce the RRR of the higher RRR material and thus caused the reduction in k for $T > 3$ K, but insufficient to become a major scattering source of electrons in the lower RRR material.

After the 800 ℃ for 2 h heating to degas specimen 5 of hydrogen, the conductivity at the phonon peak for grain 5-2 and 5-GB recovered to the before hydrogen state. However, k at the phonon peak for grain 5-1, despite having a recovery after the 800 ℃ heating, recovered to 91% of the k_{pp} before hydrogen infusion. The 800 ℃ for 2 h heating to degas hydrogen from specimen 8 had no effect on the conductivity at the phonon peak, though a mild decrease in k for $T > 3$ K was noted.

In the α and α' phases, the hydrogen atoms are disordered, and can be considered to behave like a gas [70, Chapter 2]. In the β phase, however, hydrogen is ordered with well defined spacing [70, Chapter 2], behaving like a solid. Hence, the mobility of the hydrogen atoms in the β phase is reduced, and the mobility has been observed to be about two orders of magnitude less than that in the α' phase [73–75].

The concentration of hydrogen in these two specimens was estimated to be 41.2 at. % of hydrogen, which is the $\alpha + \beta$ phase at room temperature. The additional solid-like β phase in the bulk of the specimens could be the source of the additional resistance to the flow of phonons, which led to the reduction of the phonon peak by 25% in both specimens, as seen in Figures 6.1 and 6.2. However, the reason for the reduction in k for $T > 3$ K in specimen 8, or the lack there of in specimen 5, is not clear.

The difference in the ratio of vacancies to dislocations in the two specimens could explain the extra resistance in specimen 8. Prior to the infusion of hydrogen, specimen 5 had been heat treated at 800 ℃ for 2 h, while specimen 8 had been heat treated at 1100 ℃ for 4 h. Through thermal conductivity measurements at the phonon peak [76], hotter temperature heat treatments have been shown to decrease the number of dislocations in the niobium specimen. The vacancy concentration, on the other hand, increases exponentially with temperature, as was illustrated in Figure 4.34. Hence, the ratio of the number of vacancies to dislocations of specimen 8 would be greater than that of specimen 5. Since there was a reduction in k in the electron dominated regime as well for specimen 8, it implies that specimen 8 had greater concentration of hydrogen than the estimated concentration. This suggests that the concentration of hydrogen is a function of the vacancy concentration. This may have led hydrogen concentration of specimen 8 to be in the β phase at room temperature, and ε or $\varepsilon+\lambda$ phase at cryogenic temperatures. This does not, however, readily explain the absence of recovery of k after the 800 ℃ for 2 h heat treatment of specimen 8. It may be of importance to note that specimen 5, which displayed complete recovery after the 800 ℃ for 2 h heating, had been heat treated at 800 ℃ for 2 h prior to the hydrogen infusion. Specimen 8, however, had been heat treated at 1100 ℃ for 4 h prior to hydrogen infusion, followed by the 800 ℃

for 2 h heating. This may indicate the presence of an as yet unclear phenomenon that could be correlated with the specimens' condition before infusion of hydrogen.

6.4 Conclusion

The amount of hydrogen infused into niobium during controlled SRF cavity processing has negligible effect on the thermal conductivity for $1.6 \leq T \leq 4.2$ K. When saturated with hydrogen, however, the phonon peak is reduced by 25% due to hydride-phonon scattering. The concentration of hydrogen is affected by the vacancy concentration.

Chapter 7

Conclusions

The thermal conductivity of superconducting niobium is a function of grain orientation, purity, deformation, and heat treatments. Large grain niobium is a better performing alternative to conventional polycrystalline niobium sheets for SRF cavity manufacture. Accelerators requiring continuous high power operation seek to reduce RF losses by taking advantage of small surface resistances (< 5 nΩ) in Nb at temperatures of about 2 K to increase efficiency. Accelerator cavities operating at $T \approx 1.8$ K may additionally benefit from increased thermal stability by virtue of a phonon peak in Nb at 1.8 K. Phonon conductivity in the superconducting regime in polycrystal Nb is significantly limited by grain size. The reduced number of grain boundaries in large grain Nb enhances the phonon peak.

Niobium ingot production introduces thermal strains in the material, which generate dislocations and destroy potential phonon peaks. Uniaxial engineering strain as small as $\epsilon \approx 2\%$ is sufficient to reduce the phonon peak by more than 37%. The magnitude of decrease in k at the phonon peak is also strongly influenced by the grain orientation along the direction of deformation. If there are several slip systems being activated during deformation along a given crystal direction, then a relatively small magnitude of deformation may produce the same degradation on the phonon peak as a much larger strain operating on a single slip system. A 1000 ℃ for 2 h heat treatment was sufficient to recover the phonon peak after a strain as large as 15%. Depending on the number of slip systems being activated during deformation, however, the phonon peak may not be completely recovered even for strains as small as 5%.

The maximum in the phonon peak in large grain Nb also has a monotonic dependence on the RRR. The role of RRR on conduction has generally been considered for $T > 3$ K. The presence of the phonon peak is greatly influenced by deformation and heat treatments, by virtue of dislocation concentration. Separating the phonon contribution to the phonon peak by examining the ratio k_{pp}/k_3 reveals that the greatest phonon contribution is obtained for heat treatment temperatures of about 1000 ℃. Hotter heat treatment temperatures show some improvement in the phonon peak, however, the concentration of vacancies also increases. Although greater vacancies did not affect the thermal conductivity, they may aid in the formation of hydrides and can adversely affect accelerator performance. The role of saturated hydrogen on the thermal conductivity at the phonon peak appears to result from the formation of these hydrides. Hydrogen introduced into Nb through typical cavity processing steps has no effect on the phonon conductivity. While RRR influences the phonon peak, the substitutional impurity tantalum, for 520–1375 ppm in Nb, has no effect on phonon conductivity.

This study has shown that for cavities fabricated using large grain Nb, heat treatment is the single most important factor for producing a phonon peak in the thermal conductivity. Additionally, the results provide guidance for choosing heat treatment parameters by presenting their benefits with respect to the phonon peak, while also uncovering the drawbacks of the heating on other factors, such as the increase in vacancy concentration.

BIBLIOGRAPHY

BIBLIOGRAPHY

[1] H. Padamsee, J. Knobloch, and T. Hays, *RF Superconductivity for Accelerators.* Wiley-Interscience Publication, 1998.

[2] J. P. Turneaure, *Microwave Measurements of the Surface Impedance of Superconducting Tin and Lead.* PhD Dissertation, Stanford University, 1967.

[3] J. Halbritter, "Comparison between Measured and Calculated *RF* Losses in the Superconducting State," *Z. Phys. A Hadron Nucl.*, vol. 238, no. 5, pp. 466–476, 1970.

[4] R. B. Flippen, "The Radial Velocity of Magnetic Field Penetration in Type II Superconductors," *Phys. Lett.*, vol. 17, no. 3, pp. 193 – 194, 1965.

[5] J. H. Graber, *High Power RF Processing Studies of 3 GHz Niobium Superconducting Accelerator Cavities.* PhD Dissertation, Cornell University, May 1993.

[6] A. Gurevich, "Multiscale Mechanisms of SRF Breakdown," *Physica C*, vol. 441, pp. 38–43, 2006.

[7] J. P. Charrier, B. Coadou, and B. Visentin, "Improvements of Superconducting Cavity Performances at High Accelerating Gradients," *Proc. 6th European Particle Accelerator Conference*, pp. 1885–1887, 1998.

[8] B. Visentin, "Q-Slope at High Gradients: Review of Experiments and Theories," *Proc. 11th Workshop on RF Superconductivity*, pp. 74–77, 2003.

[9] P. Kneisel, G. R. Myneni, G. Ciovati, J. Sekutowicz, and T. Carneiro, "Performance of Large Grain and Single Crystal Niobium Cavities," *Proc. 12th International Workshop on RF Superconductivity*, pp. 134–142, 2005.

[10] W. Singer, H. Kaiser, X. Singer, G. Weichert, I. Jelezov, T. Khabibuline, A. Skasyrskaia, P. Kneisel, T. Fujino, and K. Saito, "Hydroforming of Superconducting TESLA Cavities," *Proc. 10th Workshop on RF Superconductivity*, pp. 170–176, 2001.

[11] W. Singer, "Seamless/Bonded Niobium Cavities," *Proc. 12th International Workshop on RF Superconductivity*, pp. 143–147, 2005.

[12] V. Palmieri, "Seamless Cavties: The Most Creative Topic in RF Superconductivity," *Proc. 8th Workshop on RF Superconductivity*, pp. 553–589, 1997.

[13] V. Palmieri, "Advancements on Spinning of Seamless Multicell Reentrant Cavities," *Proc. 11th Workshop on RF Superconductivity*, pp. 357–361, 2003.

[14] H. Padamsee, *RF Superconductivity: Science, Technology, and Applications.* Wiley-VCH Verlag GmbH & Co. KGaA, 2009.

[15] P. Kneisel, "Cavity preparation/assembly techniques and impact on Q, realistic Q-factors in a module, review of modules," *Nucl. Instrum. Meth. A*, vol. 557, pp. 250–258, 2006.

[16] B. Bonin and R. W. Röth, "Q-Degradation of Niobium Cavities due to Hydrogen Contamination," *Proc. 5th Workshop on RF Superconductivity*, pp. 210–244, 1991.

[17] C. Z. Antoine, B. Aune, B. Bonin, J. M. Cavedon, M. Juillard, A. Godin, C. Henriot, P. Leconte, H. Safa, and A. Veyssiere, "The Role of Atomic Hydrogen in Q-Degradation of Niobium Superconducting RF Cavities: Analytical Point of View," *Proc. 5th Workshop on RF Superconductivity*, pp. 616–634, 1991.

[18] B. Aune, R. Bandelmann, D. Bloess, B. Bonin, A. Bosotti, M. Champion, C. Crawford, G. Deppe, B. Dwersteg, D. A. Edwards, H. T. Edwards, M. Ferrario, M. Fouaidy, P.-D. Gall, A. Gamp, A. Gössel, J. Graber, D. Hubert, M. Hüning, M. Juillard, T. Junquera, H. Kaiser, G. Kreps, M. Kuchnir, R. Lange, M. Leenen, M. Liepe, L. Lilje, A. Matheisen, W.-D. Möller, A. Mosnier, H. Padamsee, C. Pagani, M. Pekeler, H.-B. Peters, O. Peters, D. Proch, K. Rehlich, D. Reschke, H. Safa, T. Schilcher, P. Schmüser, J. Sekutowicz, S. Simrock, W. Singer, M. Tigner, D. Trines, K. Twarowski, G. Weichert, J. Weisend, J. Wojtkiewicz, S. Wolff, and K. Zapfe, "Superconducting TESLA cavities," *Phys. Rev. ST Accel. Beams*, vol. 3, no. 9, 2000.

[19] H. Padamsee, "A New Purification Technique for Improving the Thermal Conductivity of Superconducting Nb Microwave Cavities," *IEEE Trans. Magn.*, vol. MAG-21, pp. 1007–1010, 1985.

[20] P. Kneisel, "Use of the titanium solid state gettering process for the improvement of the performance of superconducting rf cavities," *J. Less-Common Met.*, vol. 139, pp. 179–188, 1988.

[21] H. Lengeler, W. Weingarten, G. Müller, and H. Piel, "Superconducting Niobium Cavities of Improved Thermal Conductivity," *IEEE Trans. Magn.*, vol. MAG-21, pp. 1014–1017, 1985.

[22] B. Visentin, J. P. Charrier, B. Coadou, and D. Roudier, "Cavity Baking: A Cure for the High Accelerator Field Q_0 Drop," *Proc. 9th Workshop on RF Superconductivity*, pp. 198–202, 1999.

[23] G. Ciovati, "Effect of Low-Temperature Baking on the Radio-Frequency Properties of Niobium Superconducting Cavities for Particle Accelerators," *J. Appl. Phys.*, vol. 96, pp. 1591–1600, 2004.

[24] P. M. Rowell, "The Thermal Conductivity of Some Superconductors," *Proc. R. Soc. Lond. A*, vol. 254, pp. 542–550, 1960.

[25] A. C. Anderson and S. C. Smith, "Effect of Dislocations on the Lattice Thermal Conductivity of Superconducting Niobium," *J. Phys. Chem. Solids*, vol. 34, pp. 111–122, 1973.

[26] W. Wasserbäch, "Low-Temperature Thermal Conductivity of Plastically Deformed Niobium Single Crystals," *Philos. Mag. A*, vol. 38, pp. 401–431, 1978.

[27] W. Singer, A. Brinkmann, A. Ermakov, J. Iversen, G. Kreps, A. Matheisen, D. Proch, D. Reschke, X. Singer, M. Spiwek, H. Wen, and H. G. Brokmeier, "Large Grain Superconducting RF Cavities at DESY," *Proc. Linear Accelerator Conference*, 2006.

[28] A. Aizaz, T. L. Grimm, and N. T. Wright, "Thermal design studies in superconducting rf cavities: Phonon peak and Kapitza conductance," *Phys. Rev. ST Accel. Beams*, vol. 13, p. 093503, 2010.

[29] M. G. Rao and P. Kneisel, "Mechanical Properties of High RRR Niobium at Cryogenic Temperatures," *Adv. Cryog. Eng.*, vol. 40, pp. 1383–1390, 1994.

[30] S. K. Chandrasekaran, "Design and Fabrication of a High-Temperature High-Vacuum Furnace to Heat Treat Niobium for Superconducting Radio Frequency Cavities," MS Thesis, Michigan State University, May 2010.

[31] A. H. Wilson, *The Theory of Metals*. Cambridge University Press, 1936.

[32] R. E. B. Makinson, "The Thermal Conductivity of Metals," *Proc. Cam. Phys. Soc.*, vol. 34, pp. 474–497, 1938.

[33] J. K. Hulm, "The Thermal Conductivity of Tin, Mercury, Indium and Tantalum at Liquid Helium Temperatures," *Proc. R. Soc. A*, vol. 204, pp. 98–123, 1950.

[34] F. Koechlin and B. Bonin, "Parametrization of the Niobium Thermal Conductivity in the Superconducting State," *Supercond. Sci. Technol.*, vol. 9, pp. 453–460, 1996.

[35] J. Bardeen, L. N. Cooper, and J. R. Schrieffer, "Theory of Superconductivity," *Phys. Rev.*, vol. 108, pp. 1175–1204, 1957.

[36] J. Bardeen, G. Rickayzen, and L. Tewordt, "Theory of the Thermal Conductivity of Superconductors," *Phys. Rev.*, vol. 113, pp. 982–994, 1959.

[37] P. Rhodes, "Fermi-Dirac Functions of Integral Order," *Proc. R. Soc. Lon. A*, vol. 204, pp. 396–405, 1950.

[38] K. Mendelssohn and H. M. Rosenberg, "The Thermal Conductivity of Metals at Low Temperatures," *Solid State Phys.*, vol. 12, pp. 223–274, 1961.

[39] H. B. G. Casimir, "Note on the Conduction of Heat in Crystals," *Physica*, vol. 5, pp. 495–500, 1938.

[40] A. C. Anderson and S. G. O'Hara, "The Lattice Thermal Conductivity of Normal and Superconducting Niobium," *J. Low Temp. Phys.*, vol. 15, pp. 323–333, 1974.

[41] W. Wasserbäch, "Phonon-Dislocation Scattering and Low Temperature Lattice Thermal Conductivity of Niobium and Tantalum Single Crystals Deformed at Low Temperatures," *Phys. Status Solidi B*, vol. 128, pp. 453–466, 1985.

[42] W. Wasserbäch, “Lattice Thermal Conductivity and Phonon-Dislocation Interaction in Niobium and Tantalum Single Crystals Plastically Deformed at Intermediate Temperatures,” *Philos. Mag. A*, vol. 52, pp. 225–241, 1985.

[43] W. Wasserbäch, “Low-Temperature Thermal Conductivity of Plastically Deformed Niobium and Tantalum Single Crystals of [001] Orientation,” *Phys. Status Solidi A*, vol. 128, pp. 55–68, 1991.

[44] A. Connolly and K. Mendelssohn, “Thermal Conductivity of Tantalum and Niobium below 1°K,” *Proc. R. Soc. Lond. A*, vol. 266, pp. 429–439, 1962.

[45] W. Wasserbäch, “Low Temperature Thermal Conductivity of Pure and Impure Niobium and Tantalum Single Crystals,” *Phys. Status Solidi B*, vol. 84, pp. 205–214, 1977.

[46] E. P. Roth and A. C. Anderson, “Interaction Between Thermal Phonons and Dislocations,” *Phys. Rev. B*, vol. 20, pp. 768–775, 1979.

[47] E. J. Cotts, D. M. Miliotis, and A. C. Anderson, “Thermal Transport in Deformed Lithium Flouride,” *Phys. Rev. B*, vol. 24, pp. 7336–7341, 1981.

[48] A. Aizaz, *Thermal Design Studies in Niobium and Helium for Superconducting Radio Frequency Cavities*. PhD Dissertation, Michigan State University, 2006.

[49] M. R. Daymond and P. J. Withers, “A Synchrotron Radiation Study of Transient Internal Strain Changes During the Early Stages of Thermal Cycling in an Al / SiCw MMC,” *Scripta Mater.*, vol. 35, no. 10, pp. 1229–1234, 1996.

[50] H.-J. Bunge, *Texture Analysis in Materials Science*. Butterworths, 1982.

[51] J. Nye, *Physical Properties of Cristals: Their Representation by Tensors and Matrices*. Oxford University Press, 1985.

[52] K. Carroll, “Elastic Constants of Niobium from 4.2° to 300°K,” *J. Appl. Phys.*, vol. 36, pp. 3689–3690, 1965.

[53] G. Simmons and H. Wang, *Single Crystal Elastic Constants and Calculated Aggregate Properties. A Handbook*. The MIT Press, second ed., 1971.

[54] S. K. Chandrasekaran, J. V. Beck, T. R. Bieler, C. C. Compton, and N. T. Wright, “Parameter Estimation of the Thermal Conductivity of Superconducting Niobium,” *Therm. Cond.*, vol. 30, pp. 742–749, 2010.

[55] J. V. Beck and K. J. Arnold, *Parameter Estimation in Engineering and Science*. Wiley, 1977.

[56] S. J. Kline and F. A. McClintock, “Describing uncertainties in single-sample experiments,” *Mech. Eng.*, vol. 75, pp. 3–8, 1953.

[57] G. R. Myneni private communication, 2010.

[58] P. G. Klemens, “The Scattering of Low-Frequency Lattice Waves by Static Imperfections,” *Proc. Phys. Soc. A*, vol. 68, pp. 1113–1128, 1955.

[59] T. R. Bieler private communication, 2012.

[60] P. Moeck, “Physical Metallurgy for Engineers.” Portland State University Lecture, 2012.

[61] H.-E. Schaefer, “Investigation of Thermal Equilibrium Vacancies in Metals by Positron Annihilation,” *Phys. Status Solidi A*, vol. 102, pp. 47–65, 1987.

[62] S. K. Chandrasekaran, T. R. Bieler, C. Compton, W. Hartung, and N. T. Wright, “Comparison of the Role of Moderate Heat Treatment Temperatures on the Thermal Conductivity of Ingot Niobium,” *AIP Conf. Proc.*, vol. 1352, pp. 131–141, 2011.

[63] P. L. Richards and M. Tinkham, “Far-Infrared Energy Gap Measurements in Bulk Superconducting In, Sn, Hg, Ta, V, Pb, and Nb,” *Phys. Rev.*, vol. 119, pp. 575–590, 1960.

[64] M. D. Sherrill and H. H. Edwards, “Superconduting Tunneling on Bulk Niobium,” *Phys. Rev. Lett.*, vol. 6, pp. 460–461, 1961.

[65] P. Townsend and J. Sutton, “Investigation by Electron Tunneling of the Superconductivity Energy Gaps in Nb Ta Sn and Pb,” *Phys. Rev.*, vol. 128, pp. 591–595, 1962.

[66] D. Bonnet, S. Erlenkamper, H. Germer, and H. Rabenhorst, “A New Mmeasurement of the Energy Gap in Superconducting Niobium,” *Phys. Lett.*, vol. 25A, pp. 452–453, 1967.

[67] D. Baars private communication, 2011.

[68] K. Kowalski, A. Bernasik, W. Singer, and X. Singer, “In Situ XPS Investigtaion of the Baking Effect on the Surface Oxide Structure Formed on Niobium Sheets Used for Superconducting RF Cavity Production,” *Proc. 11th Workshop on RF Superconductivity*, pp. 610–613, 2003.

[69] J. Vökl and H. Wipf, “Diffusion of Hydrogen in Metals,” *Hyperfine Interact.*, vol. 8, pp. 631–637, 1981.

[70] G. Alefeld and J. Vökl, eds., *Hydrogen in Metals II: Application-Oriented Properties*. Springer-Verlag, 1978.

[71] F. Manchester and J. Pitre, “Part I: The Incoherent Phase Diagram,” *Phase Diagrams of Binary Hydrogen Alloys*, pp. 115–137, 2000.

[72] “Evaluation of the Propensity of Niobium to Absorb Hydrogen During Fabrication of Superconducting Radio Frequency Cavities for Particle Accelerators,” *J. Res. Natl. Inst. Stand. Technol.*, vol. 115, pp. 353–371, 2010.

[73] J. F. Smith, “The H-Nb (Hydrogen-Niobium) and D-Nb (Deuterium-Niobium) Systems,” *Bulletin of Alloy Phase Diagrams*, vol. 4, pp. 39–46, 1983.

[74] M. A. Pick and R. Bausch, “The Determination of the Force-Dipole Tensor of Hydrogen in Niobium,” *J. Phys. F*, vol. 6, pp. 1751–1763, 1976.

[75] J.-M. Welter and F. J. Johnen, “Superconducting Transistion Temperature and Low Temperature Resistivity in the Niobium-Hydrogen System,” *Z. Phys. B Con. Mat.*, vol. 27, pp. 227–232, 1977.

[76] S. K. Chandrasekaran, T. R. Bieler, C. Compton, and N. T. Wright, “Effect of Heat Treatment Temperature on the Thermal Conductivity of Large Grain Superconducting Niobium,” *Proc. 15th International Conference on RF Superconductivity*, pp. 593–596, 2011.